SISSA ISAS

SCUOLA INTERNAZIONALE SUPERIORE DI STUDI AVANZATI
INTERNATIONAL SCHOOL FOR ADVANCED STUDIES

Ab-initio study of oxygen adsorption on selected transition metal surfaces

Thesis submitted for the degree of

Doctor Philosophiæ

Candidate

Gabriele Cipriani

Supervisors

Dr. A. Dal Corso

Dr. S. de Gironcoli

Prof. S. Baroni

October 2000

Contents

Introduction

The term catalysis, introduced by Berzelius in 1836, indicates the ability that some materials have to facilitate specific chemical reactions. In particular, many technologically relevant chemical processes are favored, or made possible, by the surface atoms of heterogeneous catalysts. These materials, by reducing the activation energies for the reaction, increase the rate of formation of specific molecules and modify the relative distributions of the products. Transition metals are, in particular, uniquely active as catalysts, because the presence of narrow *d* states enhances their electronic density of states at the Fermi level and chemical reactivity. As very important examples we can mention the ethylene epoxidation on Ag surfaces and the NO reduction to N_2 by its reaction with CO on rhodium surfaces ($CO + NO \rightarrow CO_2 + \frac{1}{2}N_2$), occurring in automobile catalytic converters. The investigation of such processes is important both because of huge economical interests and also from a purely academic point of view, since the mechanisms at the basis of surface catalysis are still not completely understood [1].

From an experimental point of view, it is nowadays possible to study the microscopic basis of surface catalysis, with the aim of understanding the relevant atomic reaction paths and designing new and cheaper catalysts. This is mainly due to the development of surface-sensitive experimental techniques (Dynamical Low Energy Electron Diffraction (LEED-IV) or Scanning Tunneling Microscopy (STM), just to mention two), together with the progress of ultra-high vacuum technology. It has to be noted, however, that the surface science approach to catalysis consists in the study of surface reactions in very well controlled experimental conditions, which are obviously different from those occuring, for instance, in an industrial chemical reactor. Nevertheless, such experiments are able to isolate the principal chemical and physical phenomena we are interested in.

From the theoretical point of view, we are now in a position to successfully simulate these systems, performing computer experiments that are of great value in understanding the experimental findings. In fact in the last thirty years the physics community has developed efficient theoretical methods to describe quantum mechanically, at the atomic level, the chemical bonds on the surface of a catalyst. Such simulations, in particular,

give important information about microscopic processes which are not otherwise accessible by the experiments. The main tool in this context is the *Density Functional Theory* (DFT), developed by Hohenberg, Kohn and Sham in the sixties [2, 3]. This method allows an efficient and sufficiently accurate solution of the many electron problem. Even though the approximations for the exchange-correlation energy at the basis of any DFT implementation are somehow uncontrolled—the first and most used is the *Local Density Approximation* (LDA) [4]—the comparison with the experimental data has eventually confirmed that DFT is indeed able to describe atomic the structures in a large variety of systems with a great accuracy [5]. Moreover, with the availability of massively parallel super-computers and still better theoretical approximations for the exchange-correlation functional (like the moderns GGAs [6]), DFT has also become the method of choice in surface chemistry. In the ab-initio approach there is no need for any phenomenological parameter to be specified for the model: the only required input is the chemical composition of the system to be studied. This means, in particular, that the predictive power of DFT turns out to be quite independent of the specific system under investigation.

It is known that the catalytic properties of a given surface are due to both its geometrical and electronic properties, as well as to kinetic effects [1]. Although the system size and the time scales involved in a typical reaction make a complete dynamical ab-initio simulation unfeasible, the static properties can be usefully studied. Then, if one is able to estimate the most important energetic barriers for the process (i.e. the transition states), it is also possible to extrapolate some information about the kinetics of the system using Arrhenius theory for the determination of the rate constants [1]. In this sense, an accurate study of the surface morphology and electronic structure is a necessary step for any further study of heterogeneous reactivity.

In this thesis we have studied several examples of surface adsorption phenomena. We have considered, in particular, one of the principal and most elementary steps of many surface catalytic reactions with oxygen as a reactant, that is the dissociation of an O_2 molecule impinging on the metal surface, and the various structures that the resulting atomic oxygen may present in the specific case of Ag(100), Rh(110), and Pd(100) surfaces. We will describe the stable adsorption structures, discussing energetical and electronic aspects. Among these, we have also considered surface magnetism, which is known to be enhanced at surfaces and which could play an important role in the catalytic processes. In particular we have addressed the problem of surface magnetism of 4d transition metals, considering the case of Rh low-index surfaces.

Plan of the thesis

In the first chapter we briefly present the main theoretical techniques used in this thesis. We describe in particular *Density Functional Theory* framework and the Plane-Wave Pseudopotential Method.

In the second chapter we discuss oxygen adsorption on the Ag(100) surface. Even though the Ag−O system has been extensively studied from the experimental point of view [7, 8, 9, 10, 11], a satisfactory understanding of the surface morphology and the relevant reaction paths occurring in this system is still lacking, especially for Ag(100). Atomic oxygen adsorption on Ag(100) surfaces has recently been characterized by X-ray photoelectron diffraction [12]. It has been found that oxygen adsorption induces a $2\sqrt{2} \times \sqrt{2}$ missing-row reconstruction of the Ag(100) substrate below room temperature. At higher temperatures the system undergoes a phase transition to a 1×1 structure with O sitting in the fourfold hollow sites. We present an ab-initio investigation of the two covered surfaces as well of the clean one, describing the electronic structure of the system. Our calculated equilibrium geometries are in good agreement with the experimental data for the clean and covered 1×1 surfaces. We also predict that the observed $2\sqrt{2} \times \sqrt{2}$ missing-row reconstruction is indeed energetically as favored as the unreconstructed surface, even though our structural model differs in some respects from the one proposed in Ref. [12]. We have also found that oxygen sub-surface adsorption can occur at high coverage, and we have analyzed its effects on the missing-row structure. Furthermore, we have studied the chemistry of the metal-adsorbate bond, describing how O adsorption influences many of the electronic surface states present in this system.

In the third chapter we present a systematic study of the energetics for the magnetization of low-index Rh surfaces. Rhodium is a marginally non-magnetic metal which in the bulk is very close to satisfying the Stoner criterion for ferro-magnetism [13]. The narrowing of *d* bands occurring at surfaces may favor the establishment of a spontaneous spin polarization, so that the magnetic properties of Rh(100) have long been debated theoretically [14]. Starting from a recent spin-resolved XPS experiment [15] which shows evidence of a spontaneous magnetization occurring at this surface, we re-address theoretically the problem using a recently developed constrained DFT scheme. We present a systematic discussion of the magnetic properties of the Rh(111), Rh(100) and Rh(110) surfaces, discussing the effects that surface morphology has on the magnetic properties.

In the fourth chapter we report on oxygen chemisorption on the Rh(110) surface. Recent STM data [16] have shown a rather uncommon adsorption structure at $0.3/0.4$ mono-layers (ML) coverage. In Fig. 1 we show an STM image from Ref. [16] and the

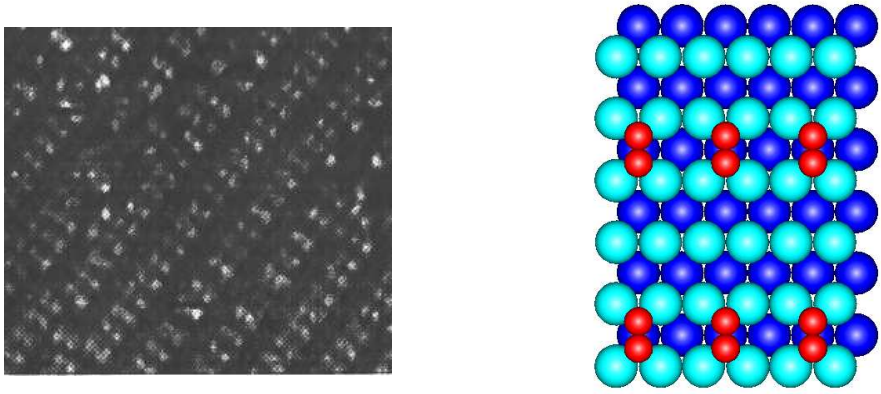

Figure 1: (Color) STM image of the low-temperature, low-coverage phase of O/Rh(110). White protrusions are to be considered as oxygen adatoms. On the right we show the structural model proposed to explain such findings.

proposed model for such a structure. According to the experiment, oxygens form rows of pairs, aligned in the (100) direction and in which the O−O bond distance is smaller than the in-plane bulk lattice periodicity. We have therefore studied the adsorption of atomic oxygen on Rh(110) at coverages ranging from 0.17 to 1 ML, identifying the most stable sites and describing how the adsorption site changes with the coverage. Even though we have not been able to predict the observed oxygen pairs, we have obtained a rather complete description of the unreconstructed low-coverage phase for O/Rh(110), in very good agreement with the experimental data [17].

Oxygen is known to induce a (2×2)p4g *clock* reconstruction on Rh(100), as do C and N on Ni(100) [18] (see Fig. 2). In the fifth chapter we study this kind of distortion, which occurs when the adatoms—situated in the hollow sites with a c(2×2) periodicity—induce a lateral relaxation of the first-layer metal atoms in such a way as to deform part of the hollows into rhombi, while the remaining square hollows are enlarged. We will initially discuss the O/Pd(100) system, which does not present such structural instability. By comparing it with the similar O/Rh(100) and O/Ni(100), we will be able to determine the different kinds of surface chemical bonds that lead to one or the other type of reconstruction. In the last part of the chapter we discuss the Al/Pd(100) system [19], which presents a reconstruction having the same LEED pattern, but this time due to a different microscopic structure. In this case, in fact, Al atoms are incorporated in the Pd second layer [19], inducing a distortion of the first surface layer. We will be able, in particular, to discriminate between two different structural models proposed in Ref. [19] and [87]. Finally, we will discuss the removal of the Al/Pd(100) (2×2)p4g recon-

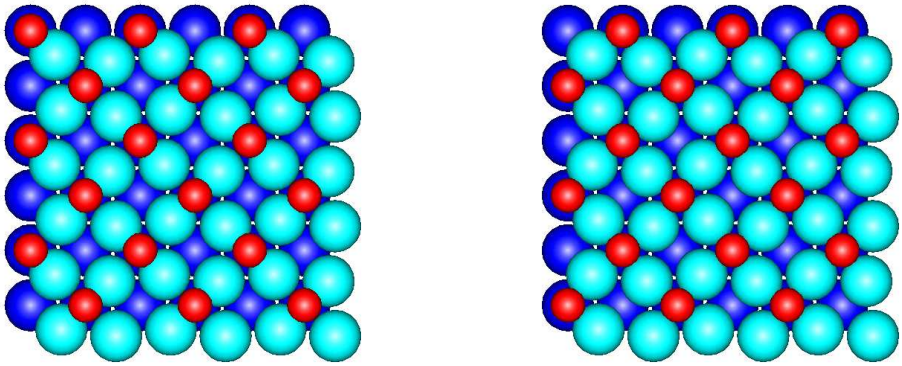

Figure 2: (Color) Adsorbate-induced reconstructions of an fcc (100) surface. Adatoms are smaller and shown as red.

struction induced by O coadsorption, studying both the oxygen equilibrium site and the structure of the final unreconstructed surface.

Chapter 1

Theoretical Tools

In this chapter we illustrate the theoretical tools used to study the energetical and structural properties, at zero temperature, of the systems considered in this thesis.

Using the Born-Oppenheimer approximation it is possible to decouple the ionic and electronic degrees of freedom, thanks to their large mass difference; in doing so one solves the Schrödinger equation for the electronic ground state by considering the nuclei as fixed, thus obtaining the total energy of the system $E[\{\mathbf{R}\}]$ as a function of ionic positions, which appear as parameters. Once this is done it is possible to study the energetics and the dynamics of ions in this effective potential. It is still not possible, however, to tackle the full many-body electronic problem directly (at least for the systems we wish to investigate), and actually it would be impossible even to store in the computer's memory the N-electrons many-body wavefunction. Nevertheless, it is possible to recast the intractable interacting problem in a more manageable self-consistent independent-electron one, much in the same way as in a Hartree calculation [20]. The theoretical basis for this approach, known as *Density Functional Theory* (DFT), has been given by Hohenberg and Kohn in the sixties [3], and it is widely used in modern computational materials science. In the following we illustrate the general DFT framework , describing the Plane Wave Pseudopotential technique.

1.1 Density functional theory

The *Density Functional Theory* describes electronic systems using a mean−field approach based on an exact result [3], stating that the ground state properties of an interacting electron system is uniquely determined by its electronic density, which minimizes

the energy functional:

$$E[n(\mathbf{r})] = F[n(\mathbf{r})] + \int V_{ext}(\mathbf{r})n(\mathbf{r})d\mathbf{r}, \tag{1.1}$$

where V_{ext} is the external potential, $F[n]$ is a universal functional (independent of V_{ext}) and the density $n(\mathbf{r})$ must satisfy the constraint:

$$\int n(\mathbf{r})d\mathbf{r} = N, \tag{1.2}$$

with N the number of electrons in the system.

Unfortunately, the functional $F[n]$ is unknown, and all its approximations in terms of the density only give poor results [21]. In order to transform DFT into a practical tool Kohn and Sham (KS) [2] introduced an auxiliary system of non-interacting electrons, with the same density of the original one:

$$n(\mathbf{r}) = \sum_i |\psi_i(\mathbf{r})|^2 \theta(\epsilon_F - \epsilon_i), \tag{1.3}$$

described by orthonormal wavefunctions ψ_i with eigenenergies ϵ_i:

$$\int \psi_i^*(\mathbf{r})\psi_j(\mathbf{r})d\mathbf{r} = \delta_{ij} \tag{1.4}$$

In this way the functional $F[n]$ is split in different parts:

$$\begin{aligned} F[n(\mathbf{r})] &= T_0[n(\mathbf{r})] + \frac{1}{2}\int \frac{n(\mathbf{r})n(\mathbf{r}')}{|\mathbf{r}-\mathbf{r}'|}d\mathbf{r}d\mathbf{r}' + E_{xc}[n(\mathbf{r})] \\ T_0[n(\mathbf{r})] &= -\sum_i \theta(\epsilon_F - \epsilon_i)\int \psi_i^*(\mathbf{r})\frac{\nabla^2}{2}\psi_i(\mathbf{r})d\mathbf{r}, \end{aligned} \tag{1.5}$$

where T_0 is the kinetic energy of the auxiliary system of non−interacting electrons, the second term is the classical electrostatic interaction and the last term, called exchange-correlation energy, accounts for all the many-body effects. The minimization of $F[n]$ can now be done by varying the wavefunctions ψ_i, imposing the constraints (1.2) and (1.4) using Lagrange multipliers. This is equivalent to the following set of non−linear Schrödinger−like equations [21]:

$$\begin{aligned} \left[-\frac{\nabla^2}{2} + V_{SCF}(\mathbf{r})\right]\psi_i(\mathbf{r}) &= \hat{H}_{KS}\psi_i(\mathbf{r}) = \epsilon_i\psi_i(\mathbf{r}) \\ V_{SCF}(\mathbf{r}) &= V_{ext}(\mathbf{r}) + \int \frac{n(\mathbf{r}')}{|\mathbf{r}-\mathbf{r}'|}d\mathbf{r}' + v_{xc}(\mathbf{r}) \\ v_{xc}(\mathbf{r}) &= \frac{\delta E_{xc}[n]}{\delta n(\mathbf{r})}, \end{aligned} \tag{1.6}$$

which have to be solved self−consistently, since the mean−field potential is defined by the charge also.

The total energy can be expressed as :

$$E_{tot} = \sum_i \theta(\epsilon_F - \epsilon_i)\epsilon_i - \frac{1}{2}\int \frac{n(\mathbf{r})n(\mathbf{r}')}{|\mathbf{r}-\mathbf{r}'|} d\mathbf{r}d\mathbf{r}' + E_{xc}[n(\mathbf{r})] - \int v_{xc}(\mathbf{r})n(\mathbf{r})d\mathbf{r} + E_{ion}, \tag{1.7}$$

where E_{ion} is the lattice electrostatic energy. Because of the variational character of the theory, forces are then easily calculated as energy derivatives with respect to ionic coordinates—without considering the implicit dependence—using Hellmann-Feynmann theorem [22].

The success of this method relies in the good description of the kinetic and electrostatic terms (which are the most important in not strongly-correlated materials), and the appropriate description of the smaller exchange-correlation part via a suitable approximation.

1.2 Approximations for the exchange-correlation energy

The simplest approximation for the exchange-correlation energy is obtained considering $E_{xc}[n]$ to be a local functional of the density:

$$E_{xc}^{LDA}[n(\mathbf{r})] = \int \epsilon_{xc}^{LDA}(n(\mathbf{r}))n(\mathbf{r})d\mathbf{r}, \tag{1.8}$$

where $\epsilon_{xc}^{LDA}(n)$ is the exchange-correlation energy density of a uniform electron gas with density n. With this prescription, the form for the v_{xc} potential is:

$$v_{xc}^{LDA}(\mathbf{r}) = \frac{d}{dn}(\epsilon_{xc}^{LDA}(n)n)\Big|_{n=n(\mathbf{r})} \tag{1.9}$$

In practice, ϵ_{xc}^{LDA} has been calculated using Quantum Monte Carlo methods and is available in a parameterized form [4, 23], representing the basis for a full ab-initio (i.e. parameter-free) description of real materials. This approach, known as Local Density Approximation (LDA), is guaranteed to work well in the high−density and in the nearly−homogeneous density regimes [2], but it has proven to be a very useful approximation also for inhomogeneous systems, like for instance covalently bonded ones. Its practical justification is eventually given by the good comparison with the experimental data.

Typically LDA yields a very good accuracy in the calculated structural and vibrational properties and usually overestimate bonding energies [24]. Its main deficiencies are in treating weak bonds—like for instance those occurring in H−bonded systems— or in the determination of small energy differences, like those regarding adatoms adsorption on surfaces [25]. To solve this problem some extensions to the original approximation have been proposed and, among these, the family of Generalized Gradient Approximation (GGAs) are able to partly correct LDA deficiencies with a modest increase in the computational load. They introduce an exchange-correlation term which depends also on the local variation of the electronic density:

$$E_{xc}^{GGA}[n(\mathbf{r}), \nabla n(\mathbf{r})] = \int \epsilon_{xc}^{GGA}(n(\mathbf{r}), |\nabla n(\mathbf{r})|) n(\mathbf{r}) d\mathbf{r}, \tag{1.10}$$

in such a way that the expression for the exchange-correlation potential now reads:

$$v_{xc}^{GGA}(\mathbf{r}) = \Big(\frac{\partial F}{\partial n} - \sum_{\alpha=1}^{3} \frac{\partial}{\partial r_\alpha} \big[\frac{\partial F}{\partial(\partial_\alpha n)} \big] \Big) \Big|_{n=n(\mathbf{r})},$$

where:

$$F[n, |\nabla n|] = \epsilon_{xc}^{GGA}(n, |\nabla n|) n.$$

It has been found that GGAs usually give a better description of the energetics [26], and in this thesis we have used LDA as well as the GGA formulation given by Perdew, Burke and Henzerhof [6].

1.3 Spin density functional theory

The *Density Functional Theory* is, at least in principle, able to describe also magnetic systems using the density as the only variable. Nevertheless, the local approximations introduced for the exchange−correlation energy make the study of such system problematic [24]. An effective solution to this problem is given by the spin−polarized version of the theory, which is motivated by the fact that the exchange-correlation hole[1] is very different for electrons with parallel and antiparallel spins. In this scheme, separate densities of spin-up and spin-down electrons are used: $n^{\uparrow}(\mathbf{r})$, $n^{\downarrow}(\mathbf{r})$. Correspondingly, the exchange-correlation energy depends also on the spin-polarization, and the KS Hamil-

[1] Given the one and two-body electron density matrices $n_1(\mathbf{r})$, $n_2(\mathbf{r}', \mathbf{r})$, the exchange-correlation hole $h_{xc}(\mathbf{r}', \mathbf{r})$ is defined by the relation $n_2(\mathbf{r}', \mathbf{r}) = n_1(\mathbf{r}')n_1(\mathbf{r}) + h_{xc}(\mathbf{r}', \mathbf{r})n_1(\mathbf{r})$.

tonian contains different potentials for spin-up and down electrons:

$$\left[-\frac{\nabla^2}{2} + V^{\sigma}_{SCF}(\mathbf{r})\right]\psi^{\sigma}_i(\mathbf{r}) = \epsilon^{\sigma}_i\psi^{\sigma}_i(\mathbf{r}) \tag{1.11}$$

$$n^{\sigma}(\mathbf{r}) = \sum_i |\psi^{\sigma}_i(\mathbf{r})|^2\theta(\epsilon_F - \epsilon^{\sigma}_i)$$

$$V^{\sigma}_{SCF}(\mathbf{r}) = V_{ext}(\mathbf{r}) + \int \frac{n(\mathbf{r}')}{|\mathbf{r}-\mathbf{r}'|}d\mathbf{r}' + v^{\sigma}_{xc}(\mathbf{r})$$

$$v^{\sigma}_{xc}[n(\mathbf{r})] = \frac{\delta E_{xc}[n^{\uparrow}, n^{\downarrow}]}{\delta n^{\sigma}(\mathbf{r})} \quad \sigma = \uparrow, \downarrow,$$

thus accounting for a possible spin-magnetization of the system. The exchange-correlation energy is again taken from the exact results for a homogeneous gas for LDA (LSDA). GGA extensions are also available [6].

1.4 Periodic systems

When the system to be simulated has translational symmetry (a perfect crystal, for instance), the most natural choice is to work with a periodically repeated simulation box, with periodic boundary conditions. In this case the KS equations (1.6) are translationally invariant:

$$V_{SCF}(\mathbf{r}) = V_{SCF}(\mathbf{r}+\mathbf{R}), \tag{1.12}$$

where **R** is a direct lattice vector. Thus, using Bloch theorem [20], the KS wavefunctions have the form:

$$\psi_i(\mathbf{r}) = \psi_{n\mathbf{k}}(\mathbf{r}) = e^{i\mathbf{k}\cdot\mathbf{r}}u_{n\mathbf{k}}(\mathbf{r}) \tag{1.13}$$

$$u_{n\mathbf{k}}(\mathbf{r}) = u_{n\mathbf{k}}(\mathbf{r}+\mathbf{R}), \tag{1.14}$$

and are labeled by the band index n and a vector $\mathbf{k}$ in the first Brillouin zone (IBZ) of the lattice. As a consequence, the computation of the electronic density and then of the energy requires an integral over the Brillouin zone:

$$n(\mathbf{r}) = \sum_{\mathbf{k}} w_{\mathbf{k}} \sum_n \theta(\epsilon_F - \epsilon_{n\mathbf{k}})|\psi_{n\mathbf{k}}(\mathbf{r})|^2, \tag{1.15}$$

where $w_{\mathbf{k}}$ is the **k**-point weight. In principle, an infinite number of points should be included in the summation 1.15. In practice, a finite set of **k**-points is used, chosen according to the symmetry properties of the system.

In the case of metals this procedure is not effective, since it is necessary to integrate across the discontinuity at the Fermi surface, and the use of a reduced number of integration points gives a bad accuracy and, also, causes instabilities in the self-consistent cycle. In this work we have solved this problem using a technique due to Methfessel and Paxton [27], which involves a smearing of the Fermi function with a gaussian/polynomial function (somehow introducing a fictitious finite electronic temperature). For a given value of the smearing, it is possible to obtain a good integration in the IBZ without using a prohibitive number of **k**-points, and the convergence of the procedure can be checked reducing the smearing parameter.

1.5 Plane wave pseudopotential method

To solve numerically the KS equations (1.6) it is necessary to expand the wavefunctions in a basis set, and one of the most common choices in ab-initio calculations is that of Plane-Waves (PW's) [28, 5]:

$$\psi_{n\mathbf{k}} = \sum_{\mathbf{G}} e^{i(\mathbf{k}+\mathbf{G})\cdot\mathbf{r}} c_n(\mathbf{k}+\mathbf{G}), \tag{1.16}$$

so that KS equations in reciprocal space read:

$$\sum_{\mathbf{G}'} \left[\frac{1}{2}|\mathbf{k}+\mathbf{G}|^2 \delta_{\mathbf{G},\mathbf{G}'} + v_h(\mathbf{G}-\mathbf{G}') + v_{xc}(\mathbf{G}-\mathbf{G}') + V(\mathbf{k}+\mathbf{G},\mathbf{k}+\mathbf{G}') \right] c_n(\mathbf{k}+\mathbf{G}') = \epsilon_{n\mathbf{k}} c_n(\mathbf{k}+\mathbf{G}), \tag{1.17}$$

where all the potentials have been Fourier-transformed and the ionic one, in particular, is considered to be non-local for reasons to be clear in the following. The accuracy of the calculation is set by fixing the kinetic energy cutoff for the truncation of the basis:

$$\frac{1}{2}|\mathbf{k}+\mathbf{G}|^2 < E_{cut} \tag{1.18}$$

The equations (1.17) are then solved self-consistently with the potential, and represent the most time-consuming part of the calculation. In appendix A we will describe a powerful technique suited for the fast diagonalization of large matrices, which we have implemented and used. The main advantages of the PW set are its translational invariance, the existence of one simple parameter to specify the accuracy and, very importantly, the availability of Fast Fourier Transform algorithms to speed up calculations. Moreover, the PW basis is not biased by atomic positions and Poisson equation is trivially solved,

since in this basis the Laplacian operator is diagonal:

$$v_h(\mathbf{G}) \propto \frac{n(\mathbf{G})}{G^2}$$

On the other hand, this basis puts the same resolution in every region of space so that it is impossible to describe, with a manageable number of PW's, the oscillations of core electrons. One possible solution for this problem is the pseudopotentials technique, a well established tool, which has an accuracy comparable to other, computationally more demanding methods. Starting from the consideration that the bonding properties are due to valence electrons, this approximation considers the core states as chemically inert, fixing them in some properly chosen reference configurations (most often the atomic ground state) and eliminates them from the calculation. The core-valence interaction is recovered via a pseudopotential, which is built to accurately replicate the valence scattering properties of the given atom. In particular, pseudopotentials are required to reproduce—at the reference electronic configurations—both the energies and the wavefunctions of the all-electron valence states outside the core region, while having nodeless and smoother pseudowavefunctions near the nuclei. A core radius is defined beyond which the pseudowavefunctions match the all-electron ones, still keeping the right amount of charge in the inner core region (norm-conservation property[29]). This approach makes it possible to perform the calculation with a manageable energy cutoff for the PW basis set. The price to be paid to achieve this goal is the use of non-local potentials, different for each angular momentum l. The first generation of such potentials had a semi-local form of the kind [30]:

$$V^{ps}(\mathbf{r},\mathbf{r}') = V_{loc}(r)\delta(\mathbf{r}-\mathbf{r}') + \sum_{l=0}^{l_{max}} V_l(r)\delta(\mathbf{r}-\mathbf{r}')P_l(\mathbf{r},\mathbf{r}'), \tag{1.19}$$

where $\hat{P}_l$ is the projector operator onto the l^{th} angular momentum. A fully non-local formulation of these potentials was introduced by Kleimann and Bylander [31] to improve computational efficiency.

This technique works most successfully with *s*/*p* bonding type materials but, with strongly localized valence electrons, like oxygen *2p* or transition metals *d* states, the requirement of the pseudowavefunction to be properly normalized makes the pseudopotential still too hard to be described with an acceptable basis set. To cure this technical problem it is possible to use a method proposed by Vanderbilt [32], which relaxes norm-conservation in order to build 'ultrasoft' pseudopotentials that make it possible to study such systems with a smaller energy cutoff. In this case the pseudopotential is completely

non local, as in the Kleinmann and Bylander form:

$$V^{ps}(\mathbf{r},\mathbf{r}') = V_{loc}(\mathbf{r})\delta(\mathbf{r}-\mathbf{r}') + \sum_{\alpha\beta I} D^0_{\alpha\beta}\langle\mathbf{r}|\beta^I_\alpha\rangle\langle\beta^I_\beta|\mathbf{r}'\rangle, \tag{1.20}$$

where the $\beta^I_\alpha(\mathbf{r})$ state is localized on the atom I:

$$\beta^I_\alpha(\mathbf{r}) = \beta_\alpha(\mathbf{r}-\mathbf{R}_I).$$

In order account for that part of the charge which is not described by the ultrasoft pseudowavefunctions $\psi_{n\mathbf{k}}$, the electron density is augmented with appropriate functions, $Q^I_{\alpha\beta}(\mathbf{r})$, localized around the core regions:

$$n(\mathbf{r}) = \sum_{n\mathbf{k}} \theta(\epsilon_F - \epsilon_{n\mathbf{k}})\Big(|\psi_{n\mathbf{k}}(\mathbf{r})|^2 + \sum_{\alpha\beta I} Q^I_{\alpha\beta}(\mathbf{r})\langle\psi_{n\mathbf{k}}|\beta^I_\alpha\rangle\langle\beta^I_\beta|\psi_{n\mathbf{k}}\rangle\Big) \tag{1.21}$$

$$Q^I_{\alpha\beta}(\mathbf{r}) = Q_{\alpha\beta}(\mathbf{r}-\mathbf{R}_I),$$

and the orthonormality condition is generalized in the following way:

$$\langle\psi_i|S|\psi_j\rangle = \delta_{ij},$$

where the overlap operator S is defined as:

$$S = 1 + \sum_{\alpha\beta I} q_{\alpha\beta}|\beta^I_\alpha\rangle\langle\beta^I_\beta|$$

Here $q_{\alpha\beta} = \int d\mathbf{r} Q_{\alpha\beta}(\mathbf{r})$. The KS equation are then obtained by varying the total energy with respect to the wavefunctions, noting that it holds the relation:

$$\frac{\delta n(\mathbf{r})}{\delta\psi^*_{n\mathbf{k}}(\mathbf{r}')} = \psi_{n\mathbf{k}}(\mathbf{r})\delta(\mathbf{r}-\mathbf{r}') + \sum_{\alpha\beta I} Q^I_{\alpha\beta}(\mathbf{r})\langle\beta^I_\beta|\psi_{n\mathbf{k}}\rangle\beta^I_\alpha(\mathbf{r}'),$$

that leads to the following self-consistent generalized eigenvalue problem:

$$\Big[-\frac{\nabla^2}{2} + \sum_{\alpha\beta I} D^I_{\alpha\beta}|\beta_\alpha\rangle\langle\beta_\beta| + v_s\Big]|\psi_{n\mathbf{k}}\rangle = \epsilon_{n\mathbf{k}} S|\psi_{n\mathbf{k}}\rangle$$

$$v_s = V_{loc} + v_h + v_{xc},$$

where the non-local part of the pseudopotential is defined self-consistently:

$$D^I_{\alpha\beta} = D^0_{\alpha\beta} + \int d\mathbf{r} v_s(\mathbf{r}) Q^I_{\alpha\beta}(\mathbf{r}).$$

1.6 Non linear core correction

In its original formulation, the pseudopotential technique substitutes the all-electron density with that coming from valence electrons only. This introduces a systematic error in the calculation of the total energy of the system because, even if the Hartree potential is linear in the charge, the exchange-correlation part is not. Such a problem will be especially relevant if there is a significant overlap between the valence and core charge. In this spirit, the non-linear core correction (NLCC) aims at improving the pseudopotential transferability, calculating $E_{xc}[n]$ using core charge also:

$$E_{xc} = \int_V (n_v(\mathbf{r}) + n_c(\mathbf{r}))\epsilon_{xc}(n_v(\mathbf{r}) + n_c(\mathbf{r}))d\mathbf{r}, \tag{1.22}$$

where $n_v(\mathbf{r})$ and $n_c(\mathbf{r})$ are the valence and core charge densities, respectively. This modification is particularly important when treating magnetic systems, in which case the neglect of NLCC can cause a serious overestimation of the spin-polarization density ζ:

$$\zeta(\mathbf{r}) = \frac{n^{\uparrow}(\mathbf{r}) - n^{\downarrow}(\mathbf{r})}{n^{\uparrow}(\mathbf{r}) + n^{\downarrow}(\mathbf{r})}, \tag{1.23}$$

leading even to qualitatively wrong results. In the case of bulk iron, for example, LSD with LDA and without NLCC predicts an fcc paramagnetic ground states when $3p$ electrons are considered as core states, whereas LSD with NLCC and GGA predicts the correct bcc ferromagnetic structure [33].

1.6.1 Supercell method

A non periodic system as a surface can be simulated with an appropriate supercell, in which a N-layer surface slab is repeated in the direction orthogonal to the surface plane, thus restoring the broken symmetry. This procedure is often preferred to the use of an isolated cluster geometry, because the calculated physical properties converge faster with the dimension of the simulated system and the use of PW's is straightforwards. It is important, anyway, to decouple all the images that have been introduced, checking the convergence of the calculation with respect to the number of atomic layers, the vacuum thickness and the lateral extension of the cell used for the simulation. In the following we will indicate an N-layers supercell, with a vacuum thickness equivalent to M bulk interlayer spacings, as an (N+M) cell.

Chapter 2

Oxygen adsorption on Ag(100)

O adsorption on Ag(100) is less well characterized than the adsorption on other low-index silver surfaces [7, 8, 9, 10, 11], and only recently a structural study of this system has been presented [12]. However, several interesting experimental results call for a theoretical investigation. Indeed, the first hint of anomalous behavior of O on Ag(100) has been found by Engelhard and Menzel [34], who measured an anomalous shift of the surface workfunction when O_2 was dosed on Ag(100). They were able to discriminate two different phases with a negative and positive oxygen-induced shift of the workfunction, at low and room temperature, respectively. They interpreted these results in terms of two different adsorbed species. The shift at high temperature was assigned to electronegative atomic oxygen above the surface, compatible with the workfunction increase, while the low-temperature one was possibly assigned to the adsorption of atomic O subsurface. Ares and Fang [35] used a combination of LEED and HREELS experiments to study this system and found a low temperature phase with a c(2×2) LEED interference pattern and a 37 meV electron energy loss, due to a surface vibrational mode, which was assigned to adsorbed atomic oxygen. By increasing the temperature from 180 to 300 K, they observed a p(1×1) LEED structure and a a shift of the electron energy loss to 30 meV. This transition was found to be reversible and was interpreted with a model in which a high temperature p(1×1) oxygen adsorbed phase is transformed into a low-temperature c(2×2) structure, with partial subsurface oxygen adsorption. Recently, Rocca et al. [12] presented a more complete investigation of the O$/$Ag(100) system, using a combination of techniques such as LEED, HREELS, XPS and XPD. They confirmed the existence of the phase transition observed by Ares Fang, and they were able to better characterize the nature of the oxygen species. In particular, their XPD measurement have shown that the high-temperature phase consists of atomic oxygen sitting in fourfold hollow sites, while the low temperature one has been interpreted as a $2\sqrt{2}\times\sqrt{2}$ missing-row reconstruction

of the substrate. In the missing-row reconstruction, the adsorbates sit in the hollow sites close to the missing rows and form a c(2×2) structure, much in the same way as in the O/Cu(100) system [36].

In this chapter, we present an extensive DFT investigation of O adsorption on Ag(100). First we discuss the adsorption on the unreconstructed surface: we identify the stable adsorption sites, studying the chemisorption energy as a function of coverage. The study of the oxygen coverage for O adsorption on Ag(100) is needed since it is not clearly determined experimentally. The O_2 dissociative sticking coefficient on Ag (100) is, in fact, very small [12] and high coverages are very difficult to achieve without employing special techniques such as supersonic molecular beams.

We then determine the stability of the recently proposed missing-row reconstruction for the low-temperature phase, we discuss its geometry, and we compare it with the experiments. We also discuss the subsurface O adsorption and its consequences on the reconstructed surface. An analysis of the electronic structure of the different phases is also presented and focused on the way the adsorption affects the electronic surface states.

This chapter is organized as follows. In Sec. 2.1 we specify the technical details of our ab-initio calculations. In Sec. 2.2 the results for the bulk system and the clean surface are reported, whereas in Sec. 2.3 we present our results for unreconstructed surfaces. In Sec. 2.4 and 2.5 we analyze the stability of the proposed $2\sqrt{2} \times \sqrt{2}$ missing-row structure, with and without subsurface oxygen. Finally, in Sec. 2.6 we present a study of the electronic surface states present on the clean and covered surfaces and, in Sec. 2.7 we draw our conclusions.

2.1 Computational details

All the calculations reported here have been performed using both LDA and GGA exchange-correlation functionals. Ultrasoft Vanderbilt pseudopotentials [32] are used to model the interaction between oxygen and silver valence and core electrons. Since O *2p* and Ag *4d* states are difficult to reproduce with classical norm-conserving pseudopotentials, we have carefully studied the convergence of the results with the wavefunction and the augmentation charge density cutoffs. Accurate and well converged total energies are achieved with 27 and 160 Ry cutoffs, respectively. For each element we have generated pseudopotentials within the RRKJ scheme [37] as described by Kresse et al. [38], starting from scalar relativistic all electron calculations. The oxygen pseudopotentials have 2 projectors for both the *2s* and *2p* states and a *3d* locality, while the silver

pseudopotentials have *5s* locality with one projector for the *5p* states and two for the *4d* states. Brillouin zone (BZ) integrations have been done with the gaussian smearing technique [27] with a 0.3 eV broadening and a (11×11×1) Monkhorst and Pack mesh [39] in the case of (1×1) cells (thus having 21 **k**-points in the irreducible wedge of the BZ), and with a (3×5×1) mesh for the $(2\sqrt{2} \times \sqrt{2})$ structures (6 inequivalent **k**-points). Computations with a smaller broadening and a finer mesh show a convergence of $\sim$2 10^{-3} Ry per atom in total energy differences. We have used supercells with 7 atomic layers and a vacuum thickness equivalent to 5 layers. All the structures have been optimized using ab-initio forces and the quasi-newton BFGS algorithm [40].

2.2 Ag bulk and clean (100) surface

The first step of our investigation has been the description of the clean Ag(100) surface. The in-plane lattice parameter of the supercells has been set using the calculated bulk data; in particular, LDA gives an equilibrium bulk lattice parameter a_0 =4.018 Å and a bulk modulus B_0 = 1350 kbar, while GGA predicts a_0 = 4.161Å and B_0 = 1015 kbar. The experimental values for these quantities are a_0 = 4.078 Å and B_0 = 1020 kbar. So our calculated LDA lattice parameter is smaller than the experimental one (-1.47%), and the calculated GGA parameter is overestimated ($+2.03\%$). Our results are in good agreement with other DFT calculations [41, 42]. The structure and the energetics of the clean surface have been obtained using N-layer symmetric slab geometry with $N = 7, 9, 11$. Thus an accurate estimate of the surface energy σ can be extrapolated numerically from its definition:

$$E(N) = 2\sigma S + NE_{bulk}, \tag{2.1}$$

where $E(N)$ is the total energy of the slab depending on the number of the slab layers N, S is the surface area and E_{bulk} is the total energy of a simple bulk unit cell. The value of the workfunction is calculated from the difference between the Fermi level and the averaged electrostatic potential in the vacuum.

The energetics and the geometrical data for a clean (1×1) slab are reported in Tab. 2.1 and compared with LEED-IV experiments [43], and with results of previous LDA estimates by Bohnen et al., who used mixed-basis all-electron calculations [41]. The relaxation of the first layer Δ_{12} (-2.01 % for LDA and -2.05% for GGA) is stronger than the one previously reported (-1.3%) in Ref. [41]. Such relaxation is also slightly overestimated in comparison with the experimental value ($\pm$ 1.5%). The second interlayer spacing relaxation ($+0.36$ % for LDA and $+0.86\%$ for GGA) is in better agreement

	σ (eV/Å^2)	ϕ (eV)	Δ_{12} (%)	Δ_{23} (%)	Δ_{34} (%)
CLEAN (LDA)	0.078	4.60	-2.01	0.36	0.25
CLEAN (GGA)	0.050	4.18	-2.05	0.82	-0.20
CLEAN (EXP)	0.082 [44]	4.62 [45]	± 1.5 [43]	± 1.5 [43]	
CLEAN (Bohnen et al.) [41]			-1.3	1.0	0.08

Table 2.1: Structural end energetic data for the clean Ag(100) surface.

with previous calculations [41] and experiments [43]. We note that LDA and GGA optimizations give very similar structural results. The calculated surface energy (σ) is 0.078 eV/Å^2 for LDA and 0.050 eV/Å^2 for GGA, both in good agreement with the experimental value which is 0.082 eV/Å^2 [44]. The calculated workfunction (ϕ) is also in very good agreement with the experimental value $\phi \simeq$ 4.60 eV [45], reading ϕ= 4.62/4.18 eV with LDA/GGA, respectively.

In Fig. 2.1 we report the projection of the density of states (PDOS) on the *s* and *d* bands for the Ag first, second and third layer atoms of the clean surface, as calculated with LDA. Since the Ag first layer atom is less coordinated than the subsurface layer atoms the width of its corresponding d/s PDOS is reduced from $\sim$ 4.5 eV to $\sim$ 3.5 eV. The narrow and intense *d*-band peaks are located between -7 eV and -2.5 eV (referring to the Fermi energy level) and are completely filled, while the large and diffuse s/p band contribution is extended above the Fermi level. The maximum of the *d*-band peak appears at $\sim -$ 3.5 eV. The presence of a small peak at $\sim$ 3.5 eV above the Fermi level corresponds to a s/p surface state as will be shown in the following, when the electronic surface states will be discussed.

2.3 Unreconstructed oxygen covered surface

2.3.1 High coverage adsorption structures

Energetics and geometry

In typical experimental conditions [12] (between 150 and 350 K) the coverage θ is about 0.1/0.2 ML, and its calibration is difficult because the O sticking probability on clean Ag(100) turns out to be small. We have studied the adsorption modes of oxygen for different coverages. The simplest case is the high coverage p(1×1)-O (1.0 ML) structure.

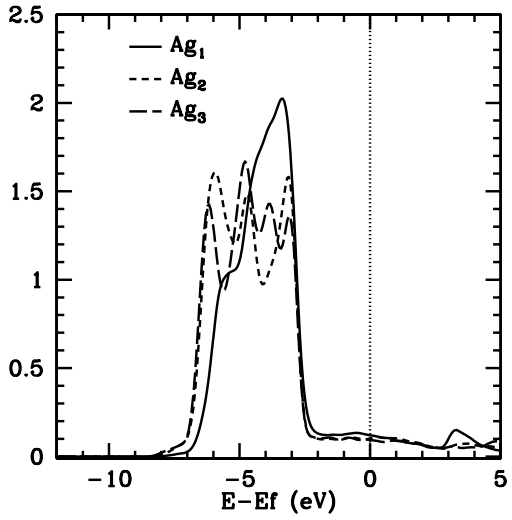

Figure 2.1: Layer-resolved local densities of states for the clean Ag(100) surface, calculated with a gaussian smearing of 0.2 eV and summing the *d* and *s* projected densities of states of the relative atoms.

Even though it has to be considered as a model case, the theoretical study of the different adsorption sites is easier for this structure, and it will bring important information for the comparison with the low coverage structures. The only experimental study (at low coverage) of the real-space structure of this system has been proposed by Rocca et al. [12], where XPD was used to characterize the adsorption geometry of the atomic oxygen on the preferred hollow site.

In this study we consider the following adsorption geometries:

- Hollow site, with O coordinated to four first layer Ag atoms.
- Subsurface hollow site, where O lies between the first and the second atomic Ag layer and where O is fivefold coordinated.
- Bridge site, with O coordinated to two first layer Ag atoms.
- Top site, in which O is only coordinated to one surface Ag atom.

Energetics and geometrical results are reported in Tab. 2.2. The chemisorption energies E_{chem} are referred to the isolated oxygen molecule and the clean surface:

$$E_{chem} = \left(E_{M-O} - E_M - N_{O_{ads}} \frac{E_{O2}}{2}\right) / N_{O_{ads}}, \tag{2.2}$$

	E_{chem} (eV/O_{atom})	ϕ (eV)	Δz_{O-Ag_1} (Å)	d_{O-Ag_1} (Å)	Δ_{12} (%)	Δ_{23} (%)
HOLLOW (LDA)	-0.25	6.42	0.49	2.07	9.89	-1.96
HOLLOW (GGA)	UNSTABLE					
SUBSURFACE HOLLOW (LDA)	-0.23	4.11	-0.44	2.06	35.9	-1.5
SUBSURFACE HOLLOW (GGA)	-0.23	3.94	-0.36	2.11	32.5	-1.9
BRIDGE (LDA)	0.56		1.38	1.98	-0.08	-0.03
BRIDGE (GGA)	0.70		1.40	2.03	-0.53	-0.75
TOP (LDA)	1.61		1.95	1.95	-0.51	-0.07
TOP (GGA)	1.62		2.02	2.02	-0.68	0.27

Table 2.2: Structural end energetic data for the 1 ML oxygen covered Ag(100) surfaces.

where E_{M-O} is the energy of the system with adsorbed atomic oxygen, $N_{O_{ads}}$ is the number of adsorbed atomic oxygens, E_M is the reference energy of the relaxed clean slab and E_{O2} is the total energy of an isolated O_2 molecule in a 12 Å-side cubic box calculated within the spin-polarized LDA or GGA approximation. The calculated chemisorption energies indicate that highly coordinated adsorption sites are favored and stable. This result agrees with the general experimental finding that atomic adsorption often occurs on multi-bonded sites. We notice that, with the exceptions of the subsurface hollow site that will be discussed in a moment, LDA and GGA gives very similar results.

At the LDA level, the most stable site is the surface fourfold hollow site with a chemisorption energy of -0.25 eV/O_{atom}. This site (lying above the surface ($\Delta z_{O-Ag_1} =$ 0.49 Å)) is not a local minimum on the GGA potential energy surface, since the complete structural optimization leads the O atom from a hollow position to a subsurface position of the oxygen atom ($\Delta z_{O-Ag_1} = -0.36$ Å). This local minimum also exists for the LDA potential energy surface ($\Delta z_{O-Ag_1} = -0.44$ Å). It corresponds to a subsurface fivefold hollow site which has almost the same chemisorption energy (-0.23 eV/O_{atom} for both LDA and GGA) as the fourfold hollow site. The subsurface site lies on top of a second layer Ag atom so it is also coordinated with the second metallic layer (d_{O-Ag2}= 2.3 Å). At the LDA level, both stable sites are separated by a transition state corresponding to a saddle point on the potential energy surface. Because of their small chemisortion energy, both the considered hollow sites are not very stable in the high coverage p(1×1) structure. In fact, at θ =1.0 ML, oxygen-oxygen repulsion strongly affects the overall stability of the system as we will discuss in the next section. Therefore the chemisorption is expected to be stronger at lower coverages.

Both LDA and GGA optimizations lead to an O-metal Ag bond length of $2.06/2.11$ Å for the hollow sites, which is in very good agreement with the experimental O-Ag distance of 2.13 Å. Moreover the oxygen chemisorption deeply affects the first interlayer spacing relaxation. For the clean surface, within LDA the Δ_{12} parameter is negative (-2.01 %)—corresponding to a contraction between the first and the second surface metallic plane—while it becomes strongly positive (9.89 %) for the hollow bonded oxygen site, which means that the presence of oxygen induces a strong expansion of the surface plane. This phenomenon has been discussed several times in the literature [42]: the charge transfer from the metal to the electronegative O atoms is responsible for the weakening of the first and second Ag layer bonds, since it removes a part of the bonding charge between these planes. For the oxygen subsurface adsorption, the first interlayer spacing Δ_{12} is even more expanded ($35.9/32.5$ %). A large part of this expansion is due to a steric repulsion between the oxygen atom and the metallic planes. The low coordinated top and bridge sites are not stable on the Ag (100) surface since their chemisorption energies are endothermic for both LDA and GGA predictions. The top site is the less stable site with chemisorption energies of $+1.61/+1.62$ eV$/\mathrm{O}_{atom}$ for LDA and GGA respectively. The chemisorption of the bridge site is stronger but still endothermic ($+0.56/+0.70$ eV$/\mathrm{O}_{at}$ for LDA and GGA respectively).

Workfunction and electronic structure

Experimentally, the presence of subsurface oxygen atoms has been advocated to explain the anomalous decrease of the workfunction with oxygen adsorption. Our calculated workfunction for the super-surface hollow site is 6.42 eV at the LDA level. It is thus 1.8 eV larger than the workfunction for the clean surface. The increase of the workfunction is due to the charge transfer from the metal to the adsorbate which increases the mean surface dipole. The calculated workfunction for the subsurface structure is $4.11/3.94$ eV for LDA and GGA respectively. This value is smaller than the one of the clean surface, because of the position of the electronegative oxygen atoms, which reduces the surface dipole. These results corroborate with the conclusions of Engelhard and Menzel [34] who considered a negative shift of the workfunction as a fingerprint of subsurface oxygen adsorption. The electronic structure analysis of the chemisorption phenomenon has been performed by analyzing the projections of the total density of states (PDOS) presented in Fig.2.2. A comparison of the DOS for the clean surface and the fourfold hollow bonded oxygen p(1×1) structure has been performed at the LDA level. On the left-hand side of the figure we have reported in panels (b) and (d) the projected densities of states (PDOS) on the Ag d_{xy} and d_{xz}, d_{yz} surface states and on

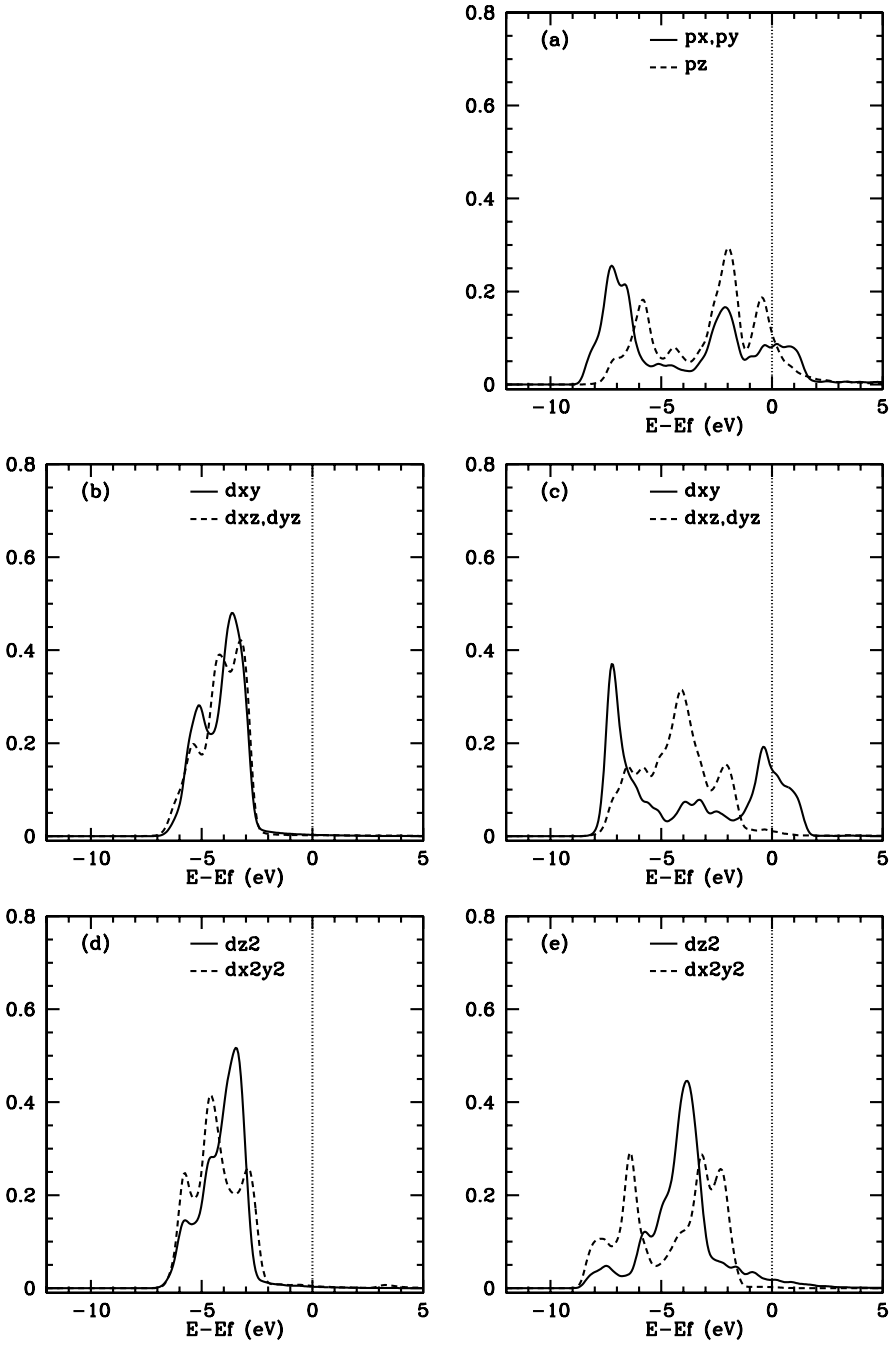

Figure 2.2: Projected densities of states (PDOS) for the oxygen p states (a) in the 1 ML hollow configuration and the first Ag atom d states in the clean (b,d) and hollow (c,e) structure , obtained with LDA and using a gaussian smearing of 0.2 eV.

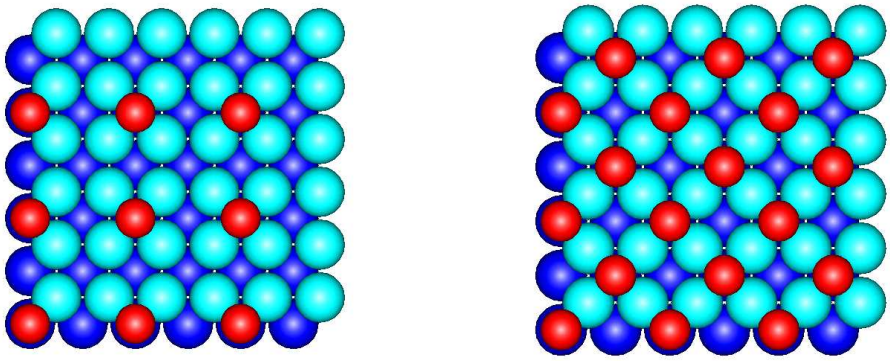

Figure 2.3: (Color) Unreconstructed O/Ag(100) p(2×2) (left) and c(2×2) (right) structures considered in the text. Oxygen atoms are smaller and depicted as red.

the Ag d_{z^2} and $d_{x^2-y^2}$ surface states for the clean surface. On the right-hand side of the figure we present the PDOS for the O p atomic orbitals (panel (a)), and on the Ag d_{xy}, d_{xz}, d_{yz} (panel (c)), d_{z^2} and $d_{x^2-y^2}$ (panel (e)) surface states, for the hollow bonded p(1×1)-O (1.0 ML) structure. The projections of the *d*-band on the different Ag 4*d* orbitals reveal a broadening of the PDOS after the oxygen adsorption (from -8 eV to $+2$ eV in panel (c) instead of -7 eV to -2 eV in the clean surface panel (b), and from -9 eV to $+2$ eV in panel (d) instead of -7 eV to -2 eV for the clean surface (panel (d)). The broadening comes from the direct interactions between the surface Ag 4*d* orbitals with the O 2*p* bands. Strong bonding peaks are visible at -7 eV for O p_x/p_y and Ag d_{xy} orbitals, which are properly oriented to bind because of the reduced oxygen height over the surface. The O p_z states, instead, have developed bonding-antibonding structures with the Ag d_{xz}/d_{yz} orbitals, while the Ag d_{z^2} are almost not affected by adsorption.

2.3.2 Medium- and low-coverage adsorption structures

The influence of the coverage on oxygen chemisorption is discussed in this section. We present results for the non-reconstructed medium- and low-coverage structures, and we compare them with those for the previous high coverage structure. Since the highly coordinated hollow site is the most stable one for the p(1×1)-O (1.0 ML) structure, all the geometry optimizations at lower coverages were performed for oxygen adsorption in this site. Both four-fold hollow and subsurface five-fold hollow sites have been considered. The low-coverage regime was simulated with a p(2×2) 0.25 ML oxygen structure, while the medium 0.5 ML coverage was modeled by a c(2×2) structure. In Fig. 2.3 we present a top-view of the super-surface structures:

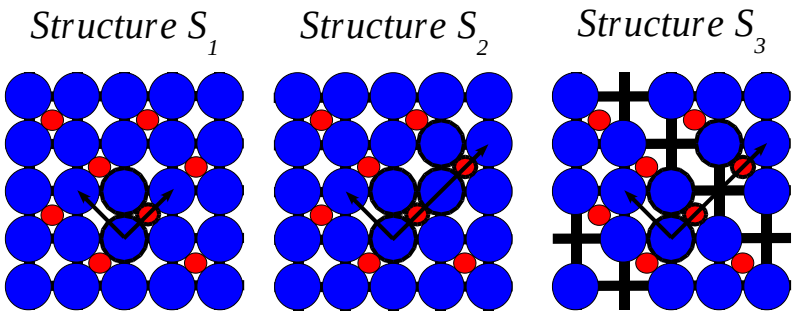

Figure 2.4: (Color) Target S_1, S_2 and S_3 structures discussed in the text

The study of the c(2×2) 0.5 ML structure is particularly interesting. In fact, a c(2×2) LEED pattern of adsorbed oxygen is observed experimentally at low temperature. However, the determination of the Ag surface structure is still debated and two different interpretations of the measurements have been suggested in the literature. The first possibility is to associate the experimental c(2×2) LEED pattern to an unreconstructed surface adsorption corresponding to a simple ($\sqrt{2} \times \sqrt{2}$)-O or S_1 structure (Fig.2.4) as proposed in [35], with one O atom and 2 surface Ag atoms in the surface unit cell. The second possibility has been proposed by Rocca et al. [12]: a missing-row reconstructed surface associated to a ($2\sqrt{2} \times \sqrt{2}$)-2O/3Ag or S_3 structure (Fig.2.4) with two O atoms and 3 surface Ag atoms in the unit cell. The results for the missing-row structure will be discussed in the next section where S_3 will be compared with S_1. In order to make the comparison more accurate, we have extended the S_1 cell along the first lattice vector giving an equivalent ($2\sqrt{2} \times \sqrt{2}$)-2O/4Ag or S_2 structure (cfr. Fig. 2.4) with two O atoms and 4 surface Ag atoms in the unit cell. For such a structure we can use the same **k**-point sampling as for the reconstructed surface, thus improving our numerical accuracy.

First of all, we have checked the stability of the subsurface hollow site. This site is not stable at low coverages according to both LDA and GGA approximations. The oxygen always sits in the fourfold hollow site at the final optimized geometry. So the change in the conformation of the potential energy surface which makes stable the subsurface site occurs only when the coverage is sufficiently high, almost at saturation (between 0.5 and 1.0 ML). These results agree with the experimental behavior [12] observed at temperatures above 300 K, when there are clear indications that atomic oxygen starts migrating into the bulk. In Fig. 2.5 we report the chemisorption energies for the calculated non-reconstructed surfaces. For the 0.5 ML coverage, the calculated LDA and

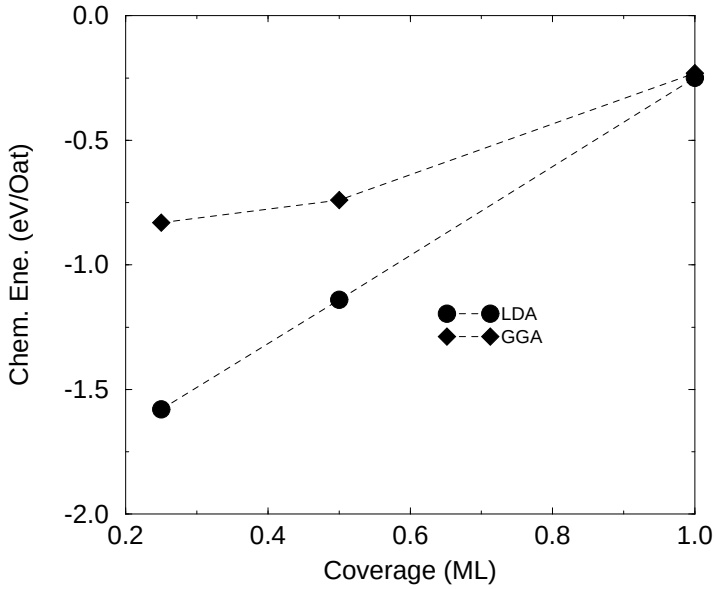

Figure 2.5: Calculated chemisorption energies for the most stable non-reconstructed structures considered, varying the coverage.

GGA chemisorption energies of the hollow site (see Fig. 2.3) are stronger for the non-reconstructed S_2 structure than for the high coverage p(1×1) structure (-1.14 eV for LDA and -0.74 eV for GGA). So the hollow site—which was not a local minimum at the GGA level at coverage 1.0 ML—becomes now stable at lower coverage. The stabilization due to the lowering of the coverage also occurs for the 0.25 ML p(2×2)-O structure (-1.58 eV for LDA and -0.83 eV for GGA), with a smaller effect between coverages 0.5 and 0.25 ML (Tab. 2.3). Hence both GGA and LDA show an important strengthening of the oxygen chemisorption when the coverage is lowered. This phenomenon has already been explained for the adsorption of atomic oxygen on Pd(100) [46], and it will be discussed in the following. The optimized structural parameters for both LDA and GGA S_2 and p(2×2) structures are reported in Tab. 2.3. The decrease of the coverage is clearly associated with the lengthening of the Ag-O bond distance d_{Ag_1-O}. In fact, the LDA Ag-O bond length equals 2.07 Å at full coverage, and it is elongated for coverages 0.5 and 0.25 ML (2.14 and 2.20 Å, respectively). The GGA results are consistent with the LDA trends (2.20 and 2.27 Å for 0.5 and 0.25 ML coverages, respectively). As the d_{Ag_1-O} increases, the oxygen height over the first Ag layer Δz_{O-Ag_1} is also elongated from 0.5 Å at full coverage to $0.75/0.82$ Å (LDA/GGA) at 0.5 ML coverage, and $0.78/0.80$ Å at 0.25 ML coverage. In this last case, moreover, we

	E_{chem} (eV/O_{atom})	ϕ (eV)	Δz_{O-Ag_1} (Å)	$\Delta_{lat}(Ag_1)$ (Å)	d_{O-Ag_1} (Å)	Δ_{12} (%)	Δ_{23} (%)
p(2 × 2) (LDA)	−1.58	5.41	0.82	0.02	2.20	−0.4	−0.18
p(2 × 2) (GGA)	−0.83	5.01	0.80	0.03	2.27	−1.5	1.5
S_2 (LDA)	−1.14	5.73	0.75	0.0	2.14	2.7	−0.4
S_2 (GGA)	−0.74	5.31	0.71	0.0	2.20	3.2	−0.9
EXP (Rocca et al.) [12]			0.6		2.13		
Ricart et al. [47]			0.97				

Table 2.3: Structural end energetic data for the 0.25 and 0.5 ML oxygen covered unreconstructed surfaces.

have found an almost negligible oxygen-induced 0.05/0.06 Å buckling of the second Ag layer, and a smaller lateral shift $\Delta_{lat}(Ag_1)$ = 0.02/0.03 Å of the silver atoms next to the adatoms. This behavior can be understood considering the effect of the repulsive electrostatic interaction between the adsorbates. At high coverage, the short O−O distance destabilizes the chemisorption, and the adatoms tend to fit into the hollows to partly shield their interaction with the metal electrons. At low coverage, instead, the electrostatic interaction is no more so effective, the adsorbates-metal bonds are stronger, and the oxygen height can accommodate to optimal values.

The only experimental data regarding the geometry of this system are those by Rocca et al. [12], who performed XPD measurements of an unreconstructed phase at low coverage, with oxygen having no clearly defined superstructure, thus finding a p(1×1) periodicity. They found a preferred fourfold hollow site adsorption, with an oxygen height of 0.6 Å. So our predictions for the 0.5 and 0.25 ML structures are in a good agreement with this experimental reference. Our LDA and GGA optimized O-Ag_1 height are moreover in better agreement with the experiments than a previous Hartree-Fock ab-initio molecular orbital cluster model study, where only the oxygen position was relaxed and the O-Ag_1 height was optimized to 0.97 Å [47].

Finally, in Fig. 2.6 we report a plot of the surface workfunction for different values of the coverage. We show the result for the most stable unreconstructed structures, always finding a monotone increase with the coverage, except in the θ=1 case for GGA, when the subsurface oxygen adsorption does decrease the mean surface dipole (the same would be for the subsurface p(1×1) geometry considered within LDA, but it happens to be less stable than the super-surface one).

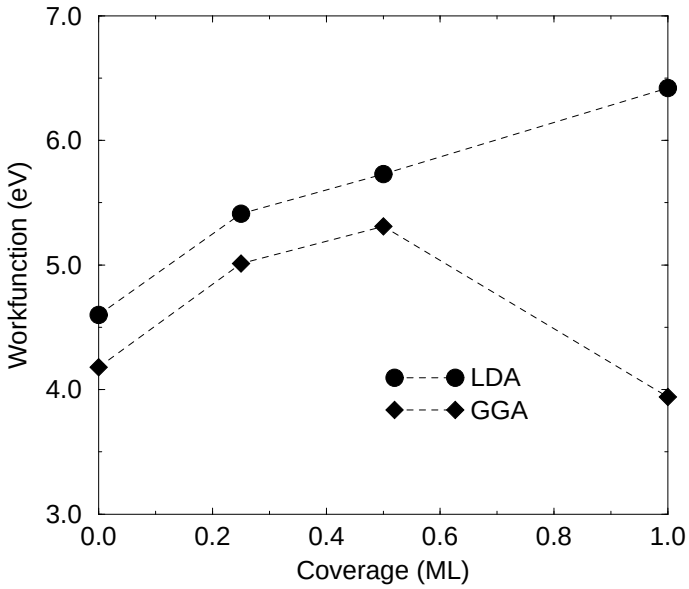

Figure 2.6: Calculated workfunctions for the most stable non-reconstructed structures considered, varying the coverage.

2.4 Missing-row reconstructed oxygen covered surface

An oxygen-induced missing row reconstruction has been suggested for the interpretation of LEED and XPD measurements at low temperature [12]. This structure assignment needs confirmation, since the LEED pattern is consistent also with a simple c(2×2) structure [35]. Therefore a comparative study between the two possible structures ($2\sqrt{2} \times \sqrt{2}$)-2O/4Ag (previously referred as S_2) and ($2\sqrt{2} \times \sqrt{2}$)-2O/3Ag (which corresponds to S_3) is crucial to understand the phase transition occurring on the Ag(100) surface. The energetics and the optimized geometries of both structures will be compared in this section.

We have used the published XPD parameters of the missing-row structure [12] as a starting point for our structural optimization. The main geometrical parameters are defined in Fig.2.7. We indicate as $d_{lat(O)}$ and $d_{lat(Ag)}$ the lateral shifts (along the (001) direction) of the O and Ag atoms, respectively. The O-Ag bonding distance d_{O-Ag} is given for the first and second neighbors. Moreover we indicate as h_1 the vertical buckling of the first layer Ag atoms, as h_2 the distance between the first and the second Ag layer, and as h_3 the height difference between the oxygen atoms and the neighboring Ag atoms. LDA and GGA approximations have given very similar results which are

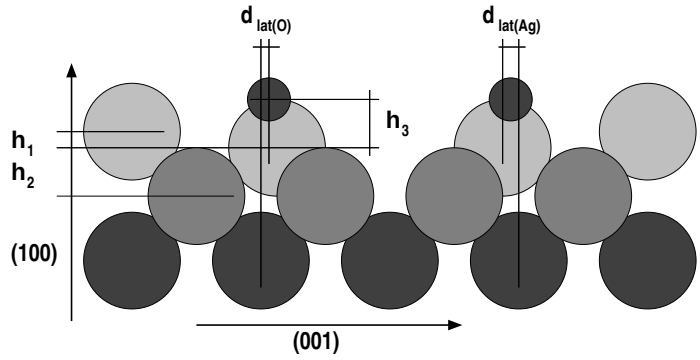

Figure 2.7: Main geometrical parameters for the S_3 missing-row reconstructed surface. Small circles are oxygen atoms.

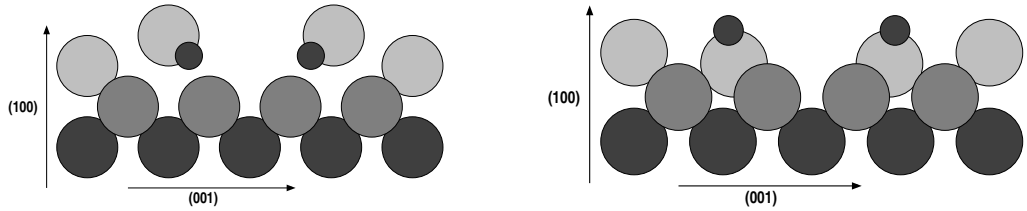

Figure 2.8: Schematic side view of the experimentally proposed (left) and calculated (right) S_3 missing-row reconstructed surface. Small circles are oxygen atoms.

reported in Tab. 2.4 and compared with experimental data. In Fig. 2.8 we sketch both the geometry proposed in Ref. [12] and our calculated structure.

The optimized structure is slightly but significantly different from that inferred from XPD data. In the XPD measurements, in facts, the oxygen atoms sits partially in a subsurface position; the adsorbate lies 0.15 Å above the unreconstructed surface plane but 0.15 Å below the silver atoms next to the missing-row, which are shifted by 0.3 Å vertically. The oxygen atoms are also moved laterally by 0.36 Å towards the missing-row, and the silver atoms are displaced with a negligible lateral shift. In the calculated structure, the oxygen atoms sit 0.30/0.25 Å (LDA/GGA) above the neighboring Ag atoms belonging to the missing-row. These Ag atoms are also laterally pushed by 0.22 Å towards the missing-row and are situated 0.14 Å below the other surface Ag atoms. O atoms are not relaxed laterally. We notice that the theoretical S_3 structure is very similar to the one proposed for the oxygen adsorption on Cu(100), which has been studied in better experimental conditions [48, 49, 50] and modeled with effective-medium theory [51]. In Tab. 2.4 we report the oxygen chemisorption energies for the missing-row

	E_{chem} (eV/cell)	ΔE_{MR} (eV/cell)	ϕ (eV)	h_3 (Å)	d_{O-Ag} (Å)	
S_3 (LDA)	-2.51	0.32	5.1	0.30	2.04/2.06	
S_3 (GGA)	-1.80	0.29	4.8	0.25	2.06/2.12	
S_4 (LDA)	-2.53	0.31	5.5	0.26	2.07/2.02	
S_4 (GGA)	-1.25	0.29	5.0	0.20	2.14/2.09	
EXP (Rocca et al.) [12]				-0.30		
	h_1 (Å)	h_2 (Å)	$d_{lat(O)}$ (Å)	$d_{lat(Ag)}$ (Å)	Δ_{12} (%)	Δ_{23} (%)
S_3 (LDA)	0.14	2.08	0.05	0.22	5.0	-0.6
S_3 (GGA)	0.14	2.17	0.03	0.22	6.3	-1.4
S_4 (LDA)	0.39	2.12	0.06	0.25	11.0	6.0
S_4 (GGA)	0.34	2.19	0.05	0.26	11.9	7.8
EXP (Rocca et al.) [12]	-0.15		0.4	0.1		

Table 2.4: Structural end energetic data for the missing-row reconstructed 0.5 ML and 0.75 ML S_3 and S_4 structures. All the energies are referred to a $2\sqrt{2} \times 2\sqrt{2}$ surface cell, the geometrical parameters are defined in Fig.2.7.

structure, which we have found to be stable.

The energetic cost ΔE_{MR} for creating the Ag(100) missing-row is calculated by estimating the corresponding variation of surface energy, between the reconstructed and the unreconstructed surface, using symmetric cells as explained in Sec. 2.2. Our calculations predict the stability of the missing-row reconstruction because it turns out that $E^{S_3}_{chem} + \Delta E_{MR} = -2.19/-1.51$ eV/cell using LDA/GGA, respectively. Thus the energy the system pays to reconstruct is over balanced by the stabilization due to the adsorbate$-$metal bond. On the other hand, if we compare these numbers with the chemisorption energy for the c(2×2) S_2 structure, we see that the reconstruction energy

$$E_{rec} = E^{S_3}_{chem} + \Delta E_{MR} - E^{S_2}_{chem}, \tag{2.3}$$

defined as the difference between the surface energies of the S_3 and S_2 structures, turns out to be very small. With LDA, in fact, E_{rec} = 0.08 eV/cell, while GGA gives E_{rec} =-0.02 eV/cell. Thus, according to our data, the energetics of the two competing ($2\sqrt{2} \times \sqrt{2}$) and c(2×2) 0.5 ML structures is nearly identical. They should be equally present on the surface.

The accuracy of the current exchange-correlation approximations and the finite numerical precision do not allow us to make a more definitive prediction regarding the

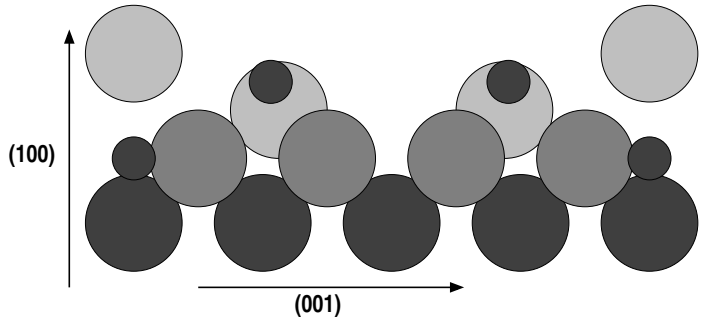

Figure 2.9: Schematic side view of the calculated S_4 missing-row reconstructed surface with subsurface oxygen. Small circles are oxygen atoms.

stability of the observed reconstructed phase, even if the system is clearly close to the onset of such a morphological transition.

2.5 Subsurface adsorption in the reconstructed phase

In this section we consider the effect of subsurface oxygen adsorption on both the geometry and the energetics of the $2\sqrt{2} \times \sqrt{2}$ reconstructed surface previously studied. Following the experimentalists' view [12], we have assumed the subsurface oxygen atoms to sit in octahedral sites, just beneath the first-layer Ag atoms not laying next to the missing-rows. We will name this new structure as S_4. Actually, there are many other available subsurface adsorption sites, and our study has to be considered only as a first effort to understand the effect of subsurface oxygen on the reconstructed Ag(110) surface. In Tab. 2.4 we present the main geometrical and energetic data for the S_4 structure, together with the experimental findings [12]. In Fig. 2.9 we present a lateral view of the calculated geometry. From a geometrical point of view, the most striking difference between the calculated S_3 and S_4 structures is that, in the latter, the Ag atoms situated over the subsurface oxygen move upwards—the h_1 parameter being now $0.39/0.34$ Å (LDA/GGA)—and are situated slightly above the O atoms in the missing-row ($0.13/0.14$ Å (LDA/GGA)). This effect is due the presence of the underlying subsurface adsorbates. Super-surface O atoms have reduced their height above the neighboring Ag atoms close to the missing-row, the h_3 parameter being $0.26/0.20$ Å (LDA/GGA). The lateral relaxations already observed for the S_3 geometry are not modified very much by oxygen in the subsurface site. Moreover, the vertical interlayer relaxations Δ_{12} and Δ_{23}—calculated using the mean positions of the surface layers—

are larger for the S_4 structure (Δ_{12} ∼11%,Δ_{23} ∼ 7% respectively) because of the pressure induced by subsurface oxygen. This new structure has a calculated workfunction (5.5/5.0 eV (LDA/GGA)), which turns out to be sligthly larger than that of the S_3 structure. Thus we can not consider this structure as the one observed by Engelhard and Menzel [34], since they observed a lowering of the workfunction for the low-temperature phase of O/Ag(100).

The energetics of the system depend on the functional used in the DFT calculations. Both LDA and GGA predict O adsorption on such a structure to be exothermic, giving a stabilization energy $E_{chem} + \Delta E_{MR}$ = −2.22/−0.96 eV/cell, respectively. Anyway, if we compare the stability of the S_4 and S_2 structures (the latter is the unreconstructed c(2×2)), the reconstruction energy turns out to be qualitatively different for the two functionals. In particular, according to LDA the S_4 structure is as favorable as the S_2 one, the reconstruction energy being only E_{rec} = 0.06 eV/cell. In the GGA case, instead, E_{rec} = 0.52 eV/cell and the S_4 structure should be ruled out if compared to the S_2 one. In this section, therefore, we have shown how the introduction of subsurface oxygen in the considered octahedral site of the ($2\sqrt{2} \times \sqrt{2}$) missing-row structure does not enhance the overall agreement with the experimental geometry. Only the LDA functional has predicted this structure to be stable when compared with the simpler c(2×2) S_2 one.

2.6 Surface states analysis

Oxygen adsorption and reconstruction induced changes of the electronic surface structure have been recently invoked in order to interpret the anomalous behavior of the Ag(100) surface plasmon dispersion upon oxygen dosing [52]. It has been observed, in fact, that the silver surface plasmon dispersion depends on the crystal face, and it is also modified by the occurrence of the already described ($2\sqrt{2} \times \sqrt{2}$) missing-row reconstruction. A tentative explanation of this fact consider the effect of electronic interband transitions between surface states to be relevant for the actual slope of surface plasmon dispersion. In this perspective, we have analyzed the electronic surface states of Ag(100) and discussed how O adsorption and the missing-row reconstruction influence the surface states.

All the calculations have been performed using the LDA and, in order to efficiently decouple the states localized at the surfaces of our supercells, we have used 11 Ag layers and 10 equivalent vacuum layers in our calculations. The use of so many metal layers is also mandatory to properly define the Fermi energy E_F, because the charge transfer from the surface to the adsorbate will not affect the overall electron counting only in the

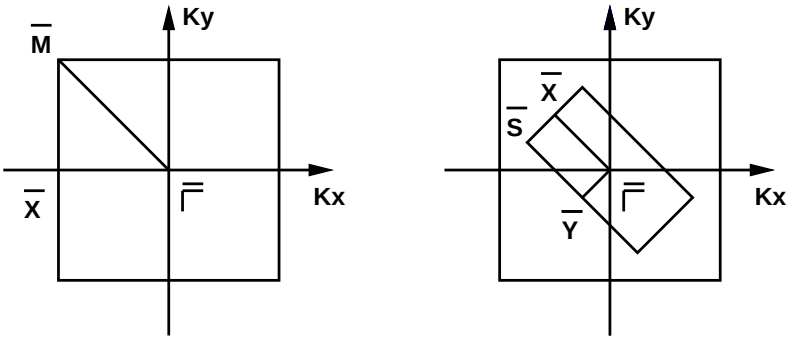

Figure 2.10: Two dimensional Brillouin zones for the p(1×1) (left) and the missing-row (right) structures.

limit of very thick slabs. In the present case, we checked that E_F is converged with an accuracy of 40 meV.

The band structure of Ag(100) near the Fermi energy is shown in Fig. 2.11, 2.12, and 2.13, for the clean and oxygen covered (1×1) and $(2\sqrt{2} \times \sqrt{2})$ structures: all the levels are referred to E_F, while the shaded area represents the bulk band structure projected on the (100) surface. The electronic states with more than 70% of charge on the first two layers have been considered as surface states and their dispersion is shown by continuous lines. Moreover, in Fig. 2.14 and 2.15 we show the planar density plots and contour plots for some of the electronic surface states at $\bar{\Gamma}$ and $\bar{X}$, respectively. We can thus follow how these states evolve as the oxygen adsorbs on the surface, with or without the induced reconstruction.

For the clean surface we notice the presence of a filled surface state (X1) at $\bar{X}$ with energy E=-0.53 eV; this state has mainly *sp* character and it is localized between the first and the third Ag layer (see Fig. 2.15). Empty states with a parabolic dispersion are predicted at E=$+0.07$ eV (X2) and E=$+3.03$ eV (X3). X2 most probably corresponds to the B state predicted by Kolb [53], which would be, in this case, located above E_F; the X3 level, instead, is the one responsible for the peak at 3 eV in the PDOS for the clean surface (see Fig. 2.1). The states X2 and X3 have also been theoretically described by Ershbaumer [54], using a FLAPW all electron method, at E=0.15 and E=2.99 eV above the Fermi energy, respectively. Two Tamm states are predicted at $\bar{M}$ (M1, M2) with energies E=-2.85, -2.42 eV. Experimentally M2 was determined to lie at E=-2.98 eV by angle resolved UPS [55, 56]. Other states are found at $\bar{\Gamma}$: $\Gamma 1$ with E=-2.97eV, and $\Gamma 2$ at E=0.99 eV.

In the presence of oxygen in the p(1×1) hollow site (unreconstructed substrate) oxygen *2p* antibonding states—indicated as X4, X5 and X6—are predicted at $\bar{X}$ at energies

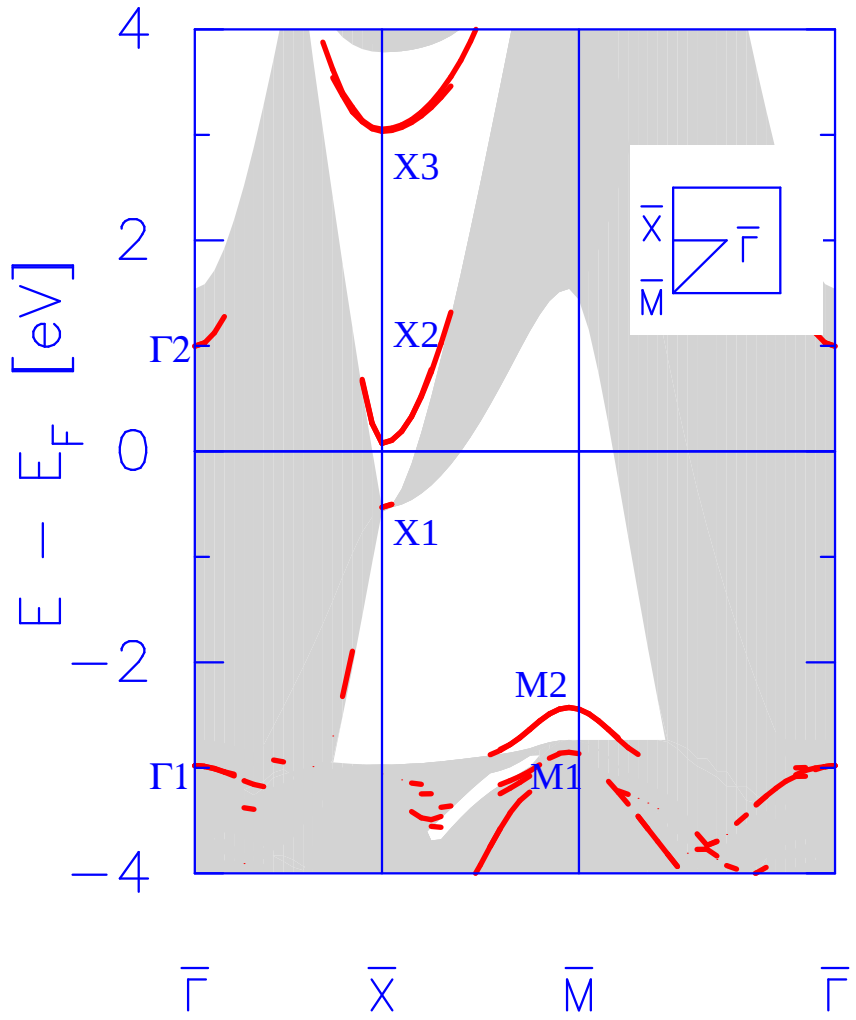

Figure 2.11: (Color) Electronic band structure of the clean Ag(100) surface.

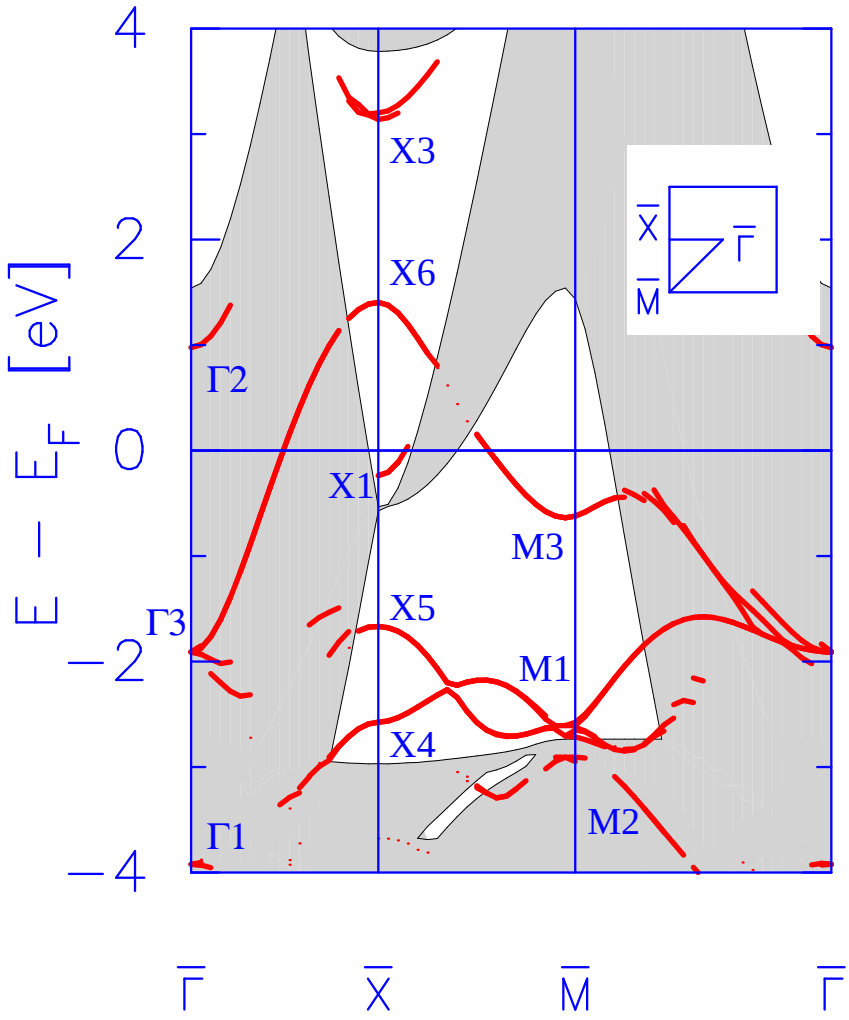

Figure 2.12: (Color) Electronic band structure of the covered p(1×1) O/Ag(100) surface.

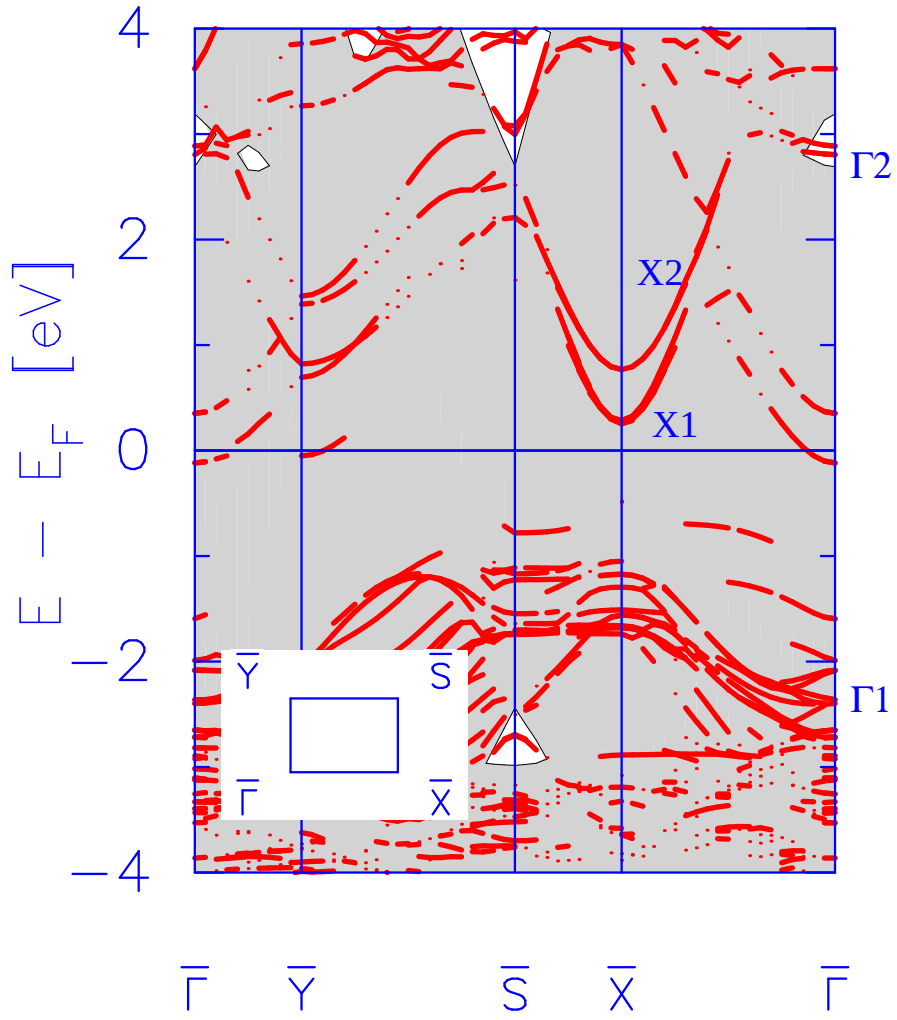

Figure 2.13: (Color) Electronic band structure of the missing-row Ag(100)-O reconstructed surface.

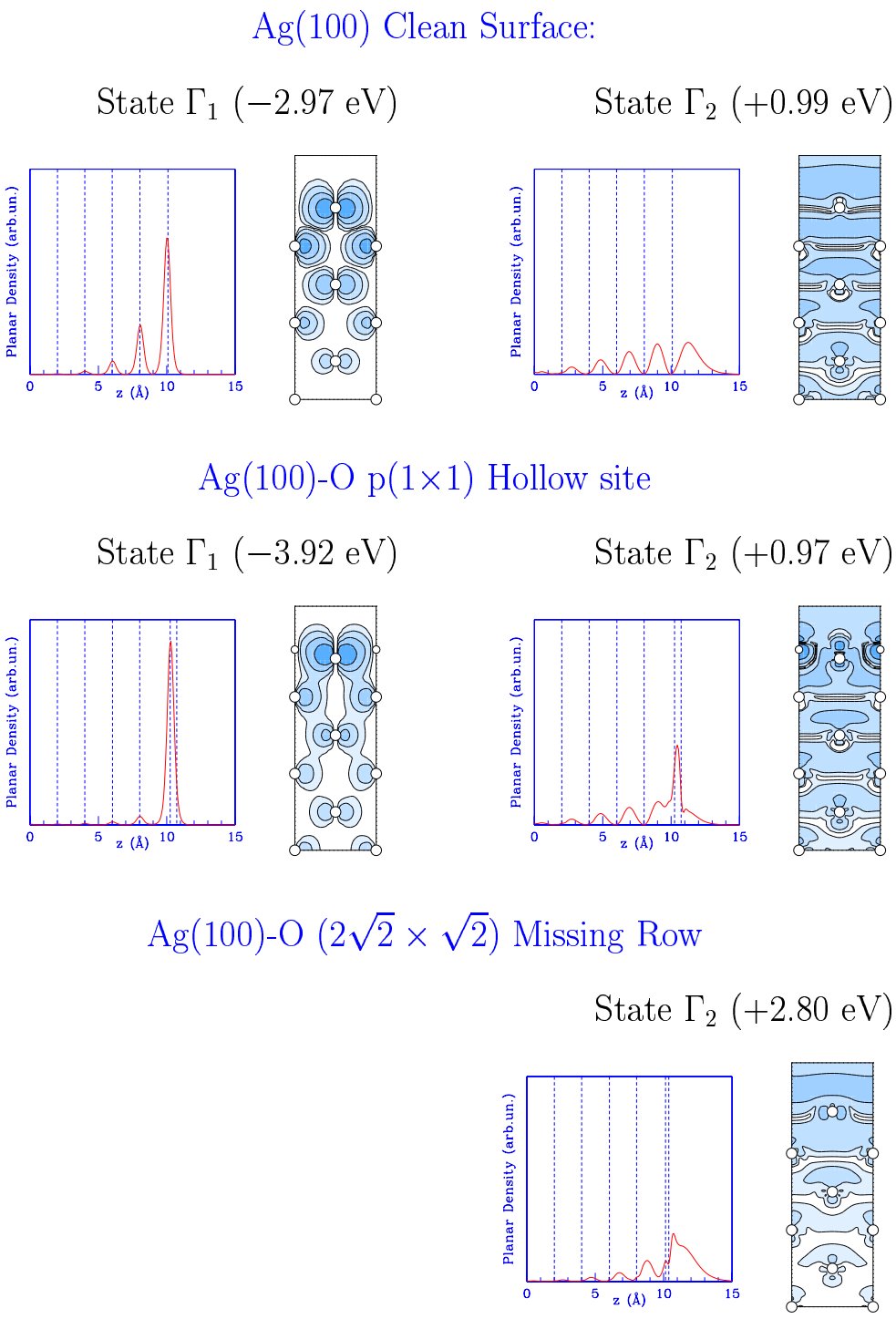

Figure 2.14: (Color) Planar density plots and contour plots of some of the electronic surface states studied at $\bar{\Gamma}$ (the scale of the contour plots is logarithmic, spanning from 10^{-2} to 10^{-5} a.u.). The dashed lines refer to the atomic planes.

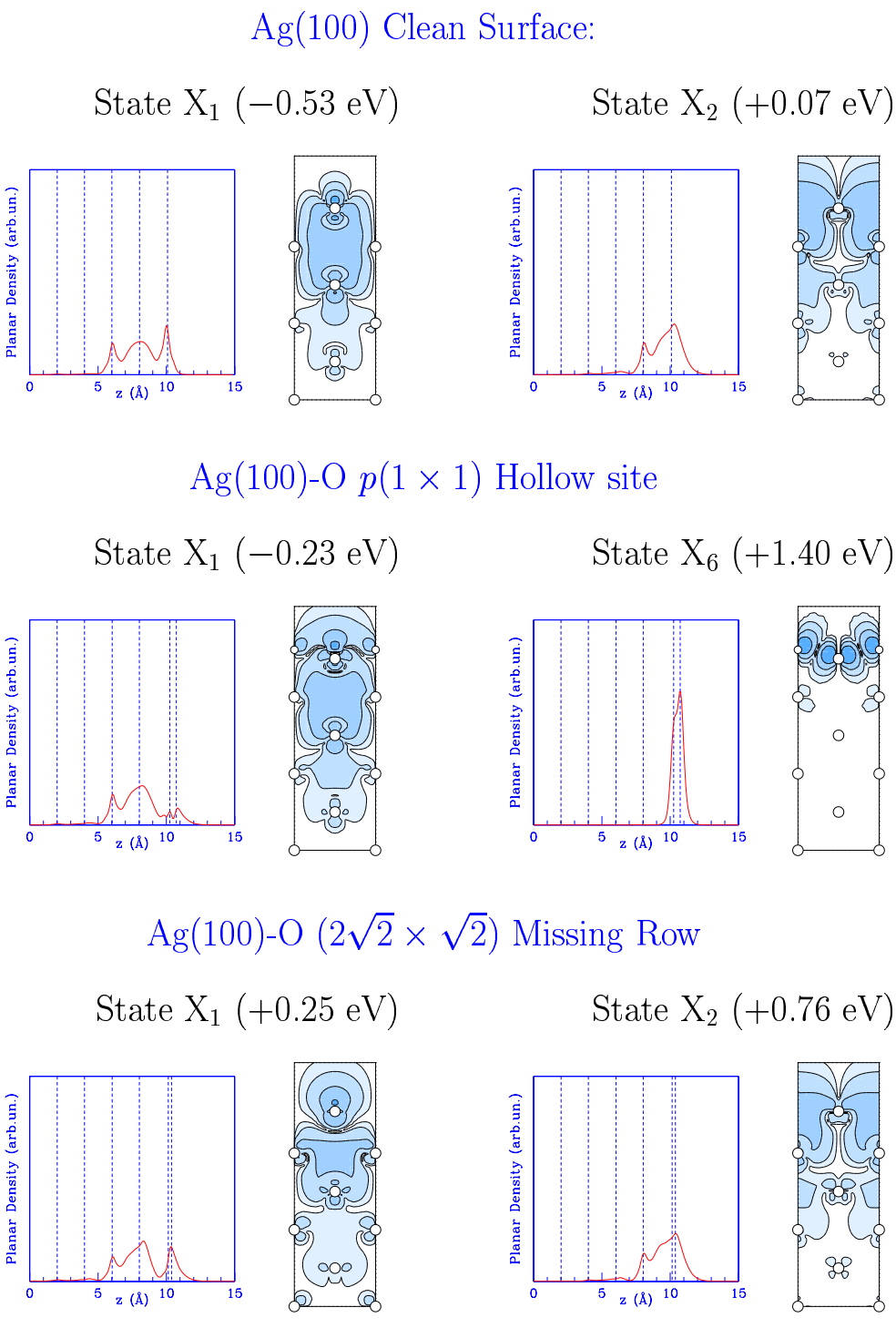

Figure 2.15: (Color) Same as in Fig. 2.14, but for states at $\bar{X}$.

-2.57 eV, -1.66 eV and 1.40 eV, respectively. Because of the dispersion, the energy of the states X4 and X5 assumes the value -2.70 eV at $\bar{M}$, while X2 reads -0.63 eV at $\bar{\Gamma}$ (indicated as $\Gamma 3$) and -1.90 eV at $\bar{M}$ (M3). The Tamm state $\Gamma 1$ at $\bar{\Gamma}$, also present on the clean surface, has now lowered its energy to -3.92 eV while $\Gamma 2$ is not shifted, being not very much perturbed by oxygen adsorption (see also the contour plots in Fig. 2.14). Moreover, the X1 state at $\bar{X}$ is now at E=-0.23 eV, thus displaying a positive shift relative to the clean surface. Note that, in this case, the state labeled X2 on the clean surface has been destroyed by oxygen adsorption, while the state X3 is still present as it is clear looking at the contour plots presented in Fig. 2.15.

For the missing row reconstructed substrate the surface Brillouin zone is folded as shown in Fig. 2.10, and the electronic band structure is consequently modified. In particular the surface states at $\bar{X}$—indicated as X1 and X2 for the clean surface—are shifted to E=+0.25 eV and E=+0.76 eV, both above the Fermi energy. This upward shift is in accord with the one observed on the Na/Cu(110) system for Na coverages lower than 0.25 ML and upon reconstruction of the surface [57, 58]. Analogously we find that oxygen adsorption removes the X1$\rightarrow$X3 surface interband transition in Ag(100) and, recently, this fact has been put into correspondence with the anomalous change in the surface plasmon dispersion when such a reconstruction occurs [52].

2.7 Conclusions

In the work described in this chapter we have been able to individuate the four-fold hollow site as the optimum one for oxygen adsorption on Ag(100) surfaces. We have then described the effect of coverage on the chemisorption structures, evidencing a subsurface adsorption at a high enough coverage. Moreover, we have given a theoretical basis to the experimentally supposed $2\sqrt{2} \times \sqrt{2}$ missing-row reconstruction, indicating that it is indeed energetically allowed, even if our calculated structure differs from the one proposed in [12]. We have then analyzed the electronic structure of the system, demonstrating the effects of both chemisorption and reconstruction on the electronic surface states.

Chapter 3

Low-index Rh surfaces magnetism

Surface magnetism is a subject that has both important basic physical and technological aspects, mainly related to thin-film physics and to the interplay between magnetism and dimensionality. In this chapter we report on a theoretical study of the possibility of a spontaneous magnetic order of the three low-index Rh(111), Rh(100) and Rh(110) surfaces, using a recently developed spin-constrained technique.

Many *3d* transition elements are magnetic. On the contrary, *4d* and *5d* transition metals do not exhibit any magnetic order in their bulk phases. It is also known, however, that such systems, when prepared in low-dimensionality structures, may present a spontaneous magnetization. For instance, Rh atomic clusters have been found to be ferromagnetic [59], and there is also evidence that a Rh monolayer grown on Ag(100) or Au(100) can sustain a finite magnetization [60]. This facts can be rationalized by noticing that the main effect of the lower dimensionality is a reduction of the local coordination and hybridization of the atoms, so that the local electronic density of states:

$$n(E,\mathbf{r}) = \sum_i \delta(E - E_i)|\langle \mathbf{r}|\Psi_i\rangle|^2$$

has a reduced width at the surface than in the bulk. Although it is not a rule, this will generally imply an increase of the density of states at the Fermi energy $n(E_F,\mathbf{r})$, so as to make energetically easier to spin$-$polarize part of the valence electrons, gaining some exchange energy with a small cost in band energy. In fact, a uniform spin magnetization of a non-magnetic metal results in a energy variation that can be written as follows:

$$\Delta E = \int d\epsilon\ \epsilon\ n(\epsilon)\ \left[\theta(E_F + \frac{\Delta}{2} - \epsilon) + \theta(E_F - \frac{\Delta}{2} - \epsilon)\right] - \frac{1}{2}KM^2,$$
$$M = N^{\uparrow} - N^{\downarrow} = \int d\epsilon\ n(\epsilon)\ \left[\theta(E_F + \frac{\Delta}{2} - \epsilon) - \theta(E_F - \frac{\Delta}{2} - \epsilon)\right],$$

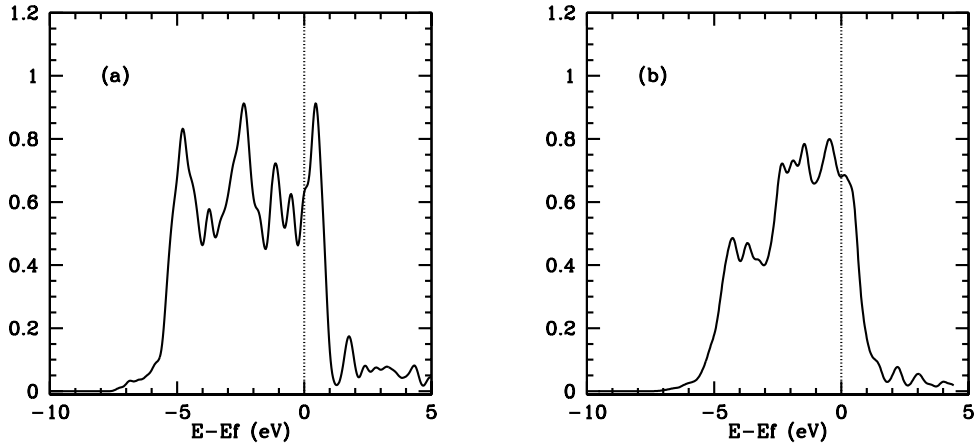

Figure 3.1: Electronic densities of states for Rh bulk (a) and projected onto the Rh(100) first layer atomic orbitals (b), calculated using a 0.15 eV energy broadening.

where Δ is a rigid spin-splitting of the spin-up/spin-down bands, $n(\epsilon)$ is the density of states in the non-magnetic phase, M is the total magnetization and K is the exchange-correlation integral, which measures the tendency of the system towards spin$-$polarization. Expanding to the lowest order in Δ, it is easy to find that the condition for the stability of the magnetic state is:

$$Kn(E_F) > 1,$$

that is the celebrated Stoner criterion for itinerant ferromagnetism. Using this model the ferromagnetism of *3d* metals can be understood in terms of their *d* bands high density of states at the Fermi energy. In the case of *4d* and *5d* metals, instead, *d* electrons are partially overlapping, their bands having a larger dispersion, and the band energy stabilizes the paramagnetic state.

According to these considerations it is reasonable to study whether an element which is only marginally magnetic in the bulk phase may present a magnetized surface, just because of the lower coordination of surface atoms. Rhodium, in particular, is a good candidate for this search because, even in its bulk phase, it is near to satisfy the Stoner criterion [13]. In Fig. 3.1 we present the electronic densities of states for Rh bulk (a), and for the Rh(100) first layer atoms orbitals (b). Note the pronounced peak near E_F for Rh bulk and the reduced width of the density of states at the surface.

Motivated by these observations and by recent experimental results [15], which show evidence of magnetic order at Rh(100) surface, in this chapter we present a systematic study of the energetics for the magnetization of Rh low-index surfaces, (100), (111) and (110). We compare their relative stability and discuss the available experimental and theoretical works, which mainly concern the Rh(100) surface.

3.1 Rh(100) surface

Rh(100) surface magnetism has been thoroughly discussed in the literature, mainly in conjuction with the problematic determination of its surface relaxations, which turn out to be not accurately decribed by theory [14]. Experimentally, in fact, the Rh(100) first interlayer distance is almost not relaxed—0.5 ± 1.0 % with respect to the bulk value [61]—while many of the theoretical predictions have given much larger values, ranging from -3.2% to -5.1% [62]. The first attempt to model Rh(100) magnetism within a DFT framework was done by Morrison [62], who tried to explain its anomalous first interlayer relaxations using a non-conventional pseudopotential technique to describe the exchange interaction of the Rh valence and *4d* electrons. He found a good agreement with the experimental values for the relaxations, and claimed a 1.8 μ_B/atom magnetization of the first two layers to be responsible for the aforementioned discrepancy. This approach was strongly criticized because of the use of the non-standard pseudopotentials, which have been later proven to be essentially wrong [63]. Other experimental and theoretical work has partly clarified the situation. Wu [64] performed spin-polarized photoemission experiments detecting only a small, almost negligible 0.2 μ_B/atom surface magnetization. Cho and Scheffler [14] have done an accurate DFT GGA study of the system, analyzing also entropic and magnetic effects. They were able to cure the discrepancy regarding the anomalous relaxations taking into account the thermal expansion of the surface, within the quasi-harmonic approximation. For what concerns the Rh(100) magnetization, they used a fixed spin calculation (described in App. B) predicting the surface to be non magnetic. Nevertheless, they found a ferromagnetic state practically degenerate with the former if the surface magnetic moment is lower than $\sim$0.5 μ_B/atom. Finally, Goldoni et al. [15] found experimental evidence of magnetic order at the Rh(100) surface, using linear magnetic dicroism in core-level photoemission experiments. They confirmed the previous experimental work, but they were not able to give a quantitative estimate of the mean surface magnetic moment, also because of the possible presence of a residual magnetic field in the sample. To summarize, the experimental data give evidence of a slightly magnetized Rh(100) surface, whereas the theoretical predictions have found its ground-state to be non-magnetic, even if a ferromagnetic structure seems to be degenerate in energy.

3.2 Computational method

3.2.1 Spin constrained calculations

Both the experiments and the theoretical calculations described before have shown, at least for Rh(100), that the surface magnetic moments we wish to investigate have to be rather small (if not null). Thus we have to look for a very tiny effect in the total energy, and both the finite numerical accuracy and the precision of the approximations used may hinder the true energetic landscape of the system. Because of this fact, we have preferred to study the energetics of the magnetization constraining the surface magnetic state, thus selecting only one solution among all those present. It will then possible, by varying the constrained quantities, to study the stability of the magnetic states. The general method to achieve this goal is the use of Lagrange multipliers, and it is described in App. B. For instance, if one wants to fix the overall cell magnetization:[1]

$$\int d\mathbf{r}\; m(\mathbf{r}) = M = const.,$$

this technique, known as Fixed Spin Method (FSM), couples the system to a homogeneous magnetic field, in such a way to constrain the ground state to have the desired magnetization. This is, actually, the method chosen by Cho and Sheffler to perform the aforementioned study of Rh(100) surface magnetization.

In our investigation we have decided not to use the FSM, noting that its application is justified only in the limit of very thick slabs calculations. Such procedure, in fact, constraints the system with a homogeneous magnetic field on the whole supercell, thus magnetizing those atoms buried inside the slab, which we know, in this case, to be non-magnetic. As a consequence, the FSM may lead to some overestimation of the energetic cost for the surface polarization. We have thus preferred a recently developed penalty-functional technique [65], which is described in App. B. Such method allows to impose a very general constraint on the magnetization profile:

$$\int d\mathbf{r}\; m(\mathbf{r})\chi(\mathbf{r}) = M = const.,$$

where χ is a generic weighting function. Due to the fact that the resulting constraining magnetic H field is modulated by χ:

$$H(\mathbf{r}) \propto \chi(\mathbf{r}),$$

[1] here $m(\mathbf{r})$ is the magnetization density.

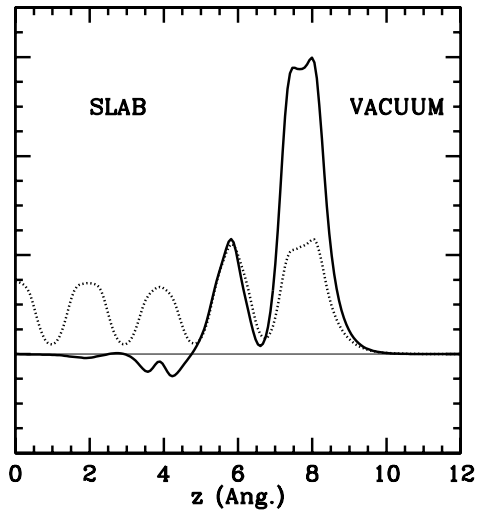

Figure 3.2: Planar density of spin polarization (arb. un.) calculated with the penalty functional method (solid line), and with the fixed-spin method (dashed line).

it is possible to select only the surface atoms to be excited, simply choosing χ to be localized in the surface region. In this manner we can avoid any fictitious magnetization of the inner part of the slab. In Fig. 3.2 we show the difference between planar averages of the Rh(100) slab surface magnetization, obtained using FSM and our penalty-functional technique: it is clear how the FSM has magnetized the bulk atoms also, while the effect of the latter method is localized on the surface.

3.2.2 Computational details

An important issue to consider when treating magnetic system within DFT is the choice of an appropriate exchange-correlation functional, able to capture the physics of the system under investigation. We have in fact verified that the LDA approximation is not able to reproduce correctly the bulk Rh magnetic susceptibility, or the energetics of the magnetic states on Rh surfaces. In Fig. 3.3 we present the result of two FSM calculation for bulk rhodium, done with LDA and with GGA plus NLCC, respectively. The calculated magnetic susceptibility turns out to be $\sim$ 598 and $\sim$109 (cgs un.)/mol with LDA and GGA, respectively. The experimental value is 111 (cgs un.)/mol [45]. Thus the neglect of NLCC and GGA has caused a strong underestimation of the magnetic stiffness of the system, while GGA with NLCC is much more accurate. Moreover, in Fig. 3.4 we show the calculated energies for the magnetized Rh(100) surface, as predicted by LDA and our penalty-functional technique. The system presents a clear magnetic ground state,

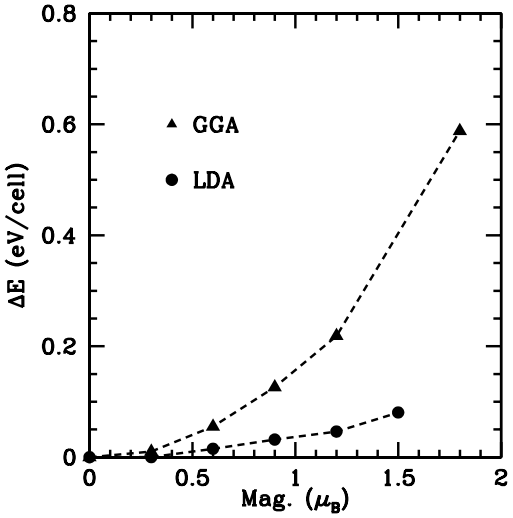

Figure 3.3: Comparison of two Fixed Spin Moment Method calculations for Rh bulk, using LDA without NLCC and GGA with NLCC, respectively

with a $\sim 2.5\ \mu_B$/atom surface polarization. In the following we will show how this is just an artifact of the approximations. We have thus preferred the use of a Vanderbilt GGA NLCC pseudopotential for Rh, generated with *s* locality, two projectors for the *4d* states and one for the *5p* states. We have used a 30 and 240 Ry cutoff for the wavefunctions and charge grid, respectively, obtaining well converged result, with a (9+5) supercell. The calculated bulk lattice parameter and bulk modulus are 3.82 Å and 2439 kbar, in good agreement with other DFT calculations [14] and the experimental values of 3.80 Å and 2690 kbar, respectively. The Brillouin zone integrations for the surfaces have been performed with a 0.3 eV broadening, using a (8×8×1) Monkhorst and Pack mesh (10 **k**-points in the irreducible wedge) for the (100) surface, and (8×6×1) and (6×6×1) (12 **k**-points) meshes for (110) and (111) surfaces, respectively. This approximation has been tested in the case of the (100) surface, where a (14×14×1) mesh (56 **k**-points) has given no qualitatively different result. We have chosen a gaussian profile (uniform in the planes parallel to the surface) for the localization function χ needed in the spin-constrained calculations, checking that our results are not affected by its specific functional form.

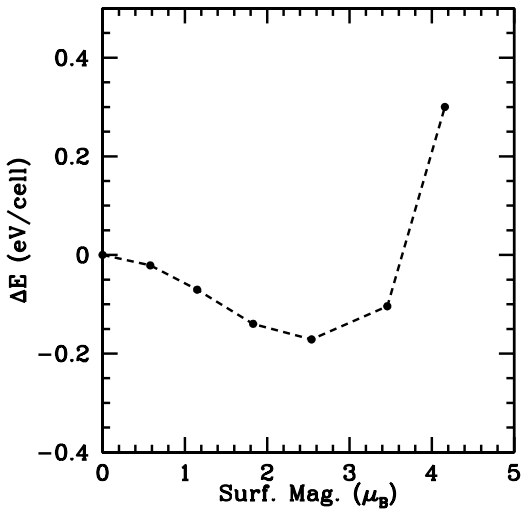

Figure 3.4: Energetics for Rh(100) surface magnetization, obtained using LDA without NLCC.

3.3 Results

Our results are reported in Fig. 3.5, where we plot the variation of surface energy (eV/surf. atom) versus atomic surface magnetization (μ_B/surf. atom) for the low-index (001), (110) and (111) surfaces. We have found that all the three orientations have a paramagnetic ground state with degenerate ferromagnetic states available up to a threshold surface polarization which is in good agreement with that previously found (some 0.5 μ_B per surface unit cell). When the surface magnetization becomes larger than this threshold the system starts paying energy. The Rh(110) surface has resulted, in particular, to be easier to magnetize then the other two surfaces, which have a similar susceptibility. This fact is in accord with the Stoner criterion, because the Rh(110) surface is the most open among those we have considered, thus presenting a higher density of electronic states at the Fermi level.

In order to further reduce the local coordination of the surface atoms, we have turned our attention to more complex surface structures, as various kinds of defects or reconstructions, which may be easier to magnetize. Interestingly, the Rh(110) surface can be prepared in a metastable (1×2) missing-row reconstructed phase, by adsorbing oxygen on the unreconstructed sample and then removing it by hydrogen titration at low temperature [66]. In such a structure the topmost Rh atoms are laterally bonded in the $(1\bar{1}0)$ direction only, and they are thus much less coordinated than those in the clean surface.

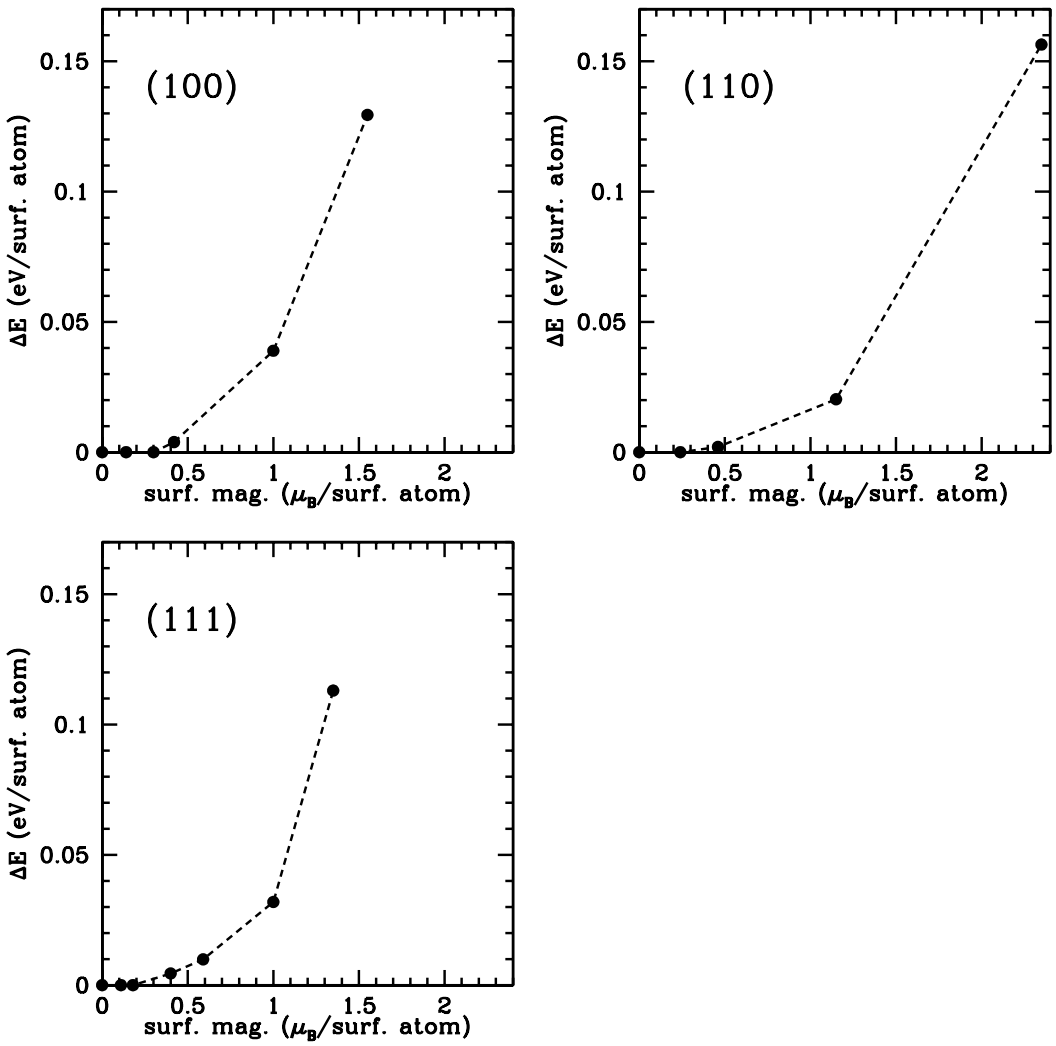

Figure 3.5: Plots of the calculated variation of surface energy (eV/surf. atom) versus the surface magnetization (μ_B/surf. atom) for the low-index surfaces we have considered.

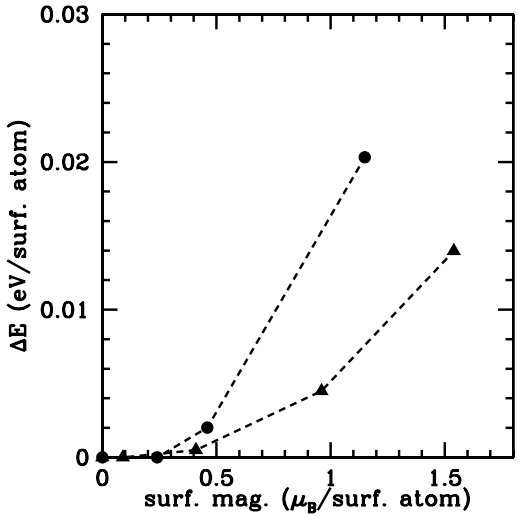

Figure 3.6: Comparison of the energetics for the magnetization of the Rh(110) clean (circles) and (1×2) (triangles) missing-row reconstructed surfaces.

Our results[2] for this system are presented in Fig. 3.6, where we compare the magnetic response of the (110) clean and missing-row reconstructed surfaces. The main feature is a large lowering of the energy needed to magnetize the reconstructed surface, even if this is not sufficient for it to develop a stable magnetic state. Nevertheless, this result suggest that rough structures like kinks or adatoms on Rh surfaces could be unstable against spin magnetization. Further work is required to clarify this point, unfortunately the simulation of extended surface defects is very problematic with fully ab-initio techniques.

3.4 Conclusions

In this chapter we have presented the first systematic study of the magnetic properties of Rh low-index surfaces. Our results indicate that such systems are close to the onset of magnetization since, together with the paramagnetic ground state, we have evidentiated the presence of ferromagnetic states energetically degenerate with the former when the surface magnetization is lower than a threshold value. At the same time, we have predicted the Rh(110) surface to be a better candidate to present a spontaneous magnetic moment than Rh(100), because of its more open structure. We have found, finally, that a structural modification like a simple missing-row reconstruction is able to greatly

[2]The **k**-point mesh for these calculations is a (6×3×1) one.

enhance the surface susceptibility.

Chapter 4

Oxygen adsorption on Rh(110)

In this chapter we present a theoretical investigation of the energetics and the equilibrium geometric structure of the Rh(110) surface in the presence of adsorbed atomic oxygen, at low temperature and low coverage. Our investigation has been mainly motivated by a collaboration with a team working at the Elettra synchrotron radiation facility in Trieste, involved in the study of the catalytic properties of Rh surfaces.

The oxygen chemisorption upon Rh(110) surfaces is known to be dissociative. Such a system presents a rich variety of different structures and induced reconstructions, varying the temperature and the coverage [66]. In the following we will indicate the sites between two atoms along the $[100]$ and $[1\bar{1}0]$ directions as long and short−bridge sites, respectively (see Fig. 4.1). At low temperature and high coverage, both experimental and theoretical results [67, 68, 69] show that oxygen adsorbs in a (2×1)p2mg structure with a saturation coverage of one mono−layer. In this case the oxygen adatoms form zig−zag rows in the troughs along the $[1\bar{1}0]$ direction (see Fig. 4.1), coordinated to two surface and one sub−surface Rh atoms, in a so called short−bridge three−fold position. When the coverage is reduced ($\theta < 0.3/0.4$ ML, experimentally) the surface does not present any long−range order and the oxygen adsorption site is changed, as it is evidentiated by the different vibrational loss detected by High Resolution Electron Energy Loss (HREELS) [70] or by the shift in the X−ray core−level photoemission (XPS) experiments [71]. On the basis of the vibrational frequencies detected by HREELS, this new chemisorption site has been suggested to be a long−bridge three−fold site, with oxygen atoms sitting slightly off the long−bridge position so as to be coordinated also to a second−layer atom. On the other hand, when the temperature is high enough to allow atoms to diffuse on the surface ($\sim$ 500−600 K), the O/Rh(110) system phase space is much more complicated and present adsorbate−induced diffusive reconstructions. The stable fully covered surface is again the (2×1)p2mg unreconstructed zig−zag structure

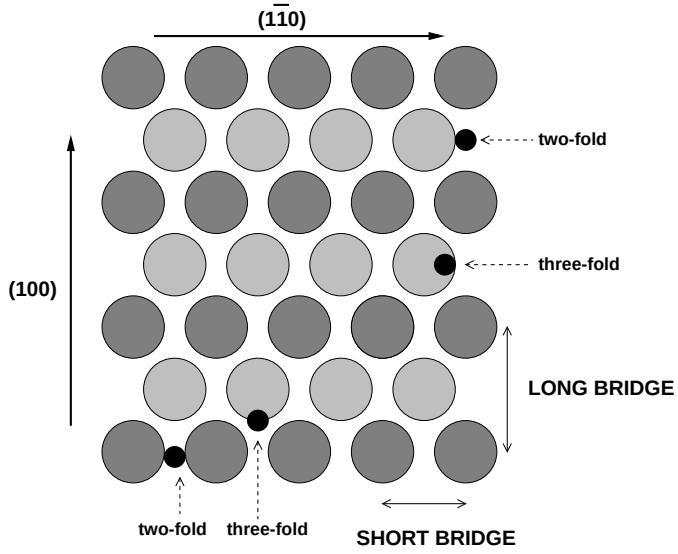

Figure 4.1: (Color) Top view of the Rh(110) surface, where we identify the long and short−bridges, and their relative adsorption sites.

already described, but the above mentioned low−temperature, low−coverage phase is metastable, and the surface undergoes different kinds of reconstructions. In particular, the experiments report many of different (1×n) missing−row reconstructions for coverages smaller than one, with overall (2×2)p2mg, (2×3)p2mg, and c(2×2n) symmetry with n = 2,3,4,5 [67, 72, 71, 73, 74, 75, 76, 77].

Some theoretical work on the same system already exists, in particular Eichler et al. [78] considered both from the structural and electronic aspects of the clean surface, while Stockbro and Baroni [69] have studied some structures at one half and full ML coverage, finding the observed equilibrium geometries and describing the bonding of the oxygen to the metal surface. The initial aim of the present investigation was to study the formation, at low temperature and low coverage, of interesting oxygen pairs adsorbed on Rh(110) and aligned along the (100) direction, as recent Scanning Tunneling Microscopy (STM) experiments have evidentiated [16]. In Fig. 4.2 we present an STM image showing the oxygen dimers formed by adatoms sitting in neighboring short−bridge sites, along the long [100] surface axis. The structural model proposed in [16] predicts the pairs to be repeated along the [1$\bar{1}$0] direction with a periodicity of two, thus having an overall (2×3) symmetry as shown in Fig. 4.2. The estimated distance between the members of each dimer is $\sim$ 2.4 Å, that is much smaller than the lattice periodicity in the [100] direction, which is 3.8 Å, and much larger than the O_2 bonding distance, which is 1.23 Å. This observation has led the experimentalist to hypotize about the presence of a short−ranged interaction between the adsorbates, mediated by the substrate, that eventually could have

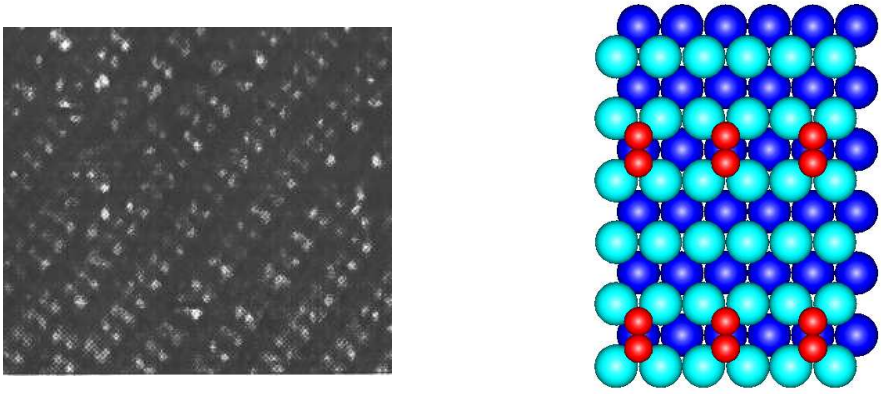

Figure 4.2: (Color) STM image of the low−temperature, low−coverage phase of Rh(110)/O. White protrusions are to be considered as oxygen adatoms. On the right we show the structural model proposed to explain such findings.

justified such a novel surface structure.

In this chapter we have studied such oxygen pairs, without being eventually able to theoretically explain their formation. Initially we addressed the atomic oxygen site preference at various coverages, describing the change of adsorption state. We have characterized the system for coverages between 0.166 and 1.0 ML, finding that on passing from $\theta = 1.0$ to $\theta = 0.5$ ML the adsorption site changes from short−bridge three−fold to short−bridge two−fold, and that this new position is preferred also at lower coverages. Our findings are thus in contrast with the assignment previously made, which was based on HREELS data only [70]. Actually, Scanning Tunneling Microscopy (STM) experiments [16] have confirmed our predictions. Finally, in the last part of the chapter, we will comment about the fact that our calculations have not predicted the oxygens pairs formation, discussing the possible reasons for this discrepancy.

4.1 Computational details

Our calculations have been performed using LDA, with Vanderbilt ultrasoft pseudopotentials. The energy cutoff for the wavefunctions and charge grid are 30 and 180 Ry, respectively. The rhodium and oxygen pseudopotentials are the same used in [79]. The one for rhodium has two projector for *4d* states, one the *5s* and *5p* locality. That for oxygen, instead, has *3d* locality and two projectors for both the *2s* and *2p* states. The calculated lattice parameter and bulk modulus for Rh are 3.81 Å and 3170 kbar, respectively, to be compared with the experimental values of 3.803 Å and 2690 kbar [80].

supercell	Δ_{12} (%)	Δ_{23} (%)	Δ_{34} (%)
(5+5)	-11	3.1	
(7+5)	-10	3.9	-2.0
(9+5)	-9.1	1.7	-2.2
Exp. [17]	$-3/-7$	$-1/-2.5$	

Table 4.1: Rh(110) clean surface relaxations.

For the O_2 molecule the calculated bonding distance and stretching frequency are 1.22 Å and 1650 cm^{-1}, while the experimental values are 1.21 Å and 1580 cm^{-1}, respectively. The integrations over the surface Brillouin zone have been done with a (8 6 2) Monkhorst & Pack mesh [39] in the case of a (1x1) cell (12 inequivalent $\mathbf{k}-$points), refolding the $\mathbf{k}-$points with bigger cells, and a 0.3 eV gaussian smearing of the Fermi function. Results will be given for (7+5) symmetric supercells.

All the structures have been relaxed to their equilibrium positions using forces, and chemisorption energies per oxygen atom are defined as in the second chapter and are referred to the clean surface and an isolated O_2 molecule.

We have checked that the accuracy of our calculations is dominated by the error related to the use of finite supercells with a limited number of layers, and we estimate the precision on chemisorption energy differences to be of the order of 40 meV. As noted in [69], this error is the consequence of the fictitious modification of the Fermi level due to the charge transfer from the metal to the oxygen, which is negligible only in the limit of very thick slabs.

4.2 Clean Surface

Usually clean metal surfaces relax, that is the distance between the first and the second layer is reduced with respect to the bulk value, while the second and third layer get more distant and so on in an oscillating fashion. In the case of Rh(110) this effect is strongly enhanced because the surface is open, and the first interlayer relaxation is $\sim$ 10%, whereas the experimental values stay between -3 % and -7 %. In Tab. 4.1 we show the values of the relaxations, calculated with different numbers of layers in the supercell, and we compare them with the available theoretical [78] and experimental values [17]. We note that the results converge rather slowly with the number of layers

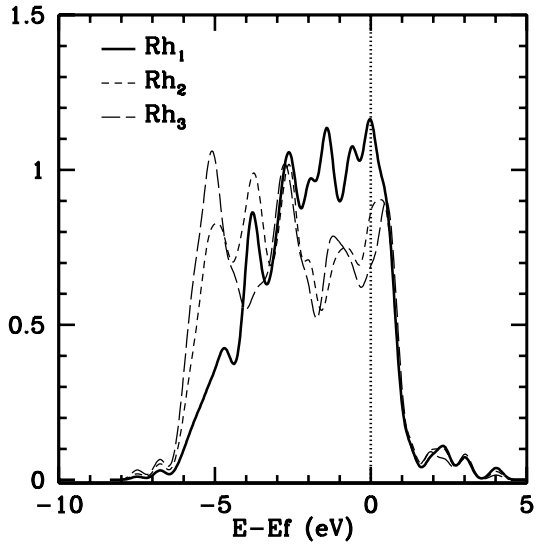

Figure 4.3: Layer−resolved local densities of states for the clean surface.

(a fact also stressed in Ref. [78]), and that the comparison with the experiment is also poor. Recently, Cho and Scheffler has pointed out that these discrepancies could be due to the neglect of thermal effects on the surface relaxations [14].

From the electronic point of view the clean surface shows resonances at the Fermi level, with prevalent *d* character. This states are important in the chemisorption process, in fact they will strongly interact with the oxygen *p* orbitals [69] stabilyzing the O−metal bonds. In Fig.4.3 we present the layer−resolved densities of states (PDOS): we note a reduced width of the PDOS of the first layer, an effect due to the lower coordination of the surface atoms with respect to those in the bulk.

4.3 Full coverage adsorption

We now characterize the oxygen adsorption structures at full coverage, studying the structural and energetical differences among the following structures, which are shown in Fig. 4.4 and include also the experimental (2×1)p2mg 'zig−zag' geometry.

- (**a**): (1×1) Long bridge two−fold
- (**b**): (1×1) Long bridge three−fold
- (**c**): (1×1) Short bridge two−fold
- (**d**): (1×1) Short bridge three−fold

STRUCT.	$\bar{z}_{O-1}$ (Å)	d_{O-O} (Å)	d_{O-1} (Å)	d_{O-2} (Å)	θ_{1-O-1} (°)	θ_{1-O-2} (°)	Δ_{12} (%)
1×1(**a**)	0.54	2.67	1.98	2.40	77	53	−7
1×1(**b**)	0.56	2.67	2.04	2.05	80	62	−2
1×1(**c**)	1.39	2.67	1.93	3.32	88	54	−0.2
1×1(**d**)	0.58	2.67	2.01	2.04	84	85	+0.8
2×1(**e**)	0.66	2.95	1.99	2.05	85	82	−3
exp.	0.60	2.93	1.98	2.05	86	84	+1

Table 4.2: 1 ML structural data, reporting: oxygen height over rhodium surface ($\bar{z}_{O-1}$), oxygen−oxygen distance (d_{O-O}), oxygen-1st/2nd nearest neighbor surface atom distance(d_{O-1},d_{O-2}), bond angle between 1st and 2nd layer atoms (θ_{1-O-1},θ_{1-O-1}) and first interlayer rhodium atoms relaxation (Δ_{12}).

STRUCT.	1×1(**a**)	1×1(**b**)	1×1(**c**)	1×1(**d**)	2×1(**e**)
E_{chem} (meV/O_{atom})	−1.58	−1.65	−1.69	−1.90	−2.12

Table 4.3: Chemisorption energies for the various 1 ML structures considered.

- (**e**): (2×1) p2mg 'zig−zag' three−fold

In Tab. 4.2 we present some data about the relaxed structures we have obtained, compared to the experimental LEED−IV parameters [17]. In Tab. 4.2 we report the calculated chemisorption energies. We note that the comparison with the experimental data is very good both for what regards the optimal equilibrium structure, which is found to be the experimental (2×1)p2mg, and for the description of the geometry of the adsorption site. This structure has a −2.12 eV chemisorption energy and maximizes oxygen−oxygen distance, thus reducing the electrostatic interaction among the charged adatoms. Note also that the oxygen−rhodium bonding angles are almost equal to $90°$. In this way the hybridization of the metal *d* orbitals and the oxygen *p* states is optimized. The O−Rh bonding distance is, moreover, very similar to that found in bulk rhodium oxide Rh_2O_3 ($\sim 2\mathring{A}$). The first interlayer relaxation of the surface has been strongly reduced by oxygen adsorption, passing from −10% of the clean surface to a much smaller −3%. The second energetically favorable structure is the (1×1) three−fold short−bridge one (**d**), with a chemisorption energy 0.22 eV higher than the optimum (2×1)p2mg one. The(1×1) two−fold short−bride geometry (**c**) has, instead, a −1.69

(**a**) (1×1) Long Bridge two-fold

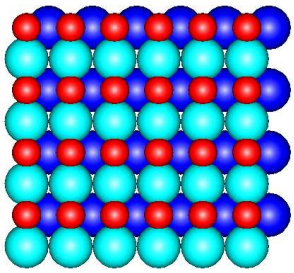

(**b**) (1×1) Long Bridge three-fold

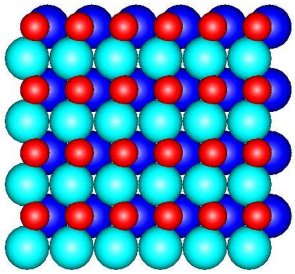

(**c**) (1×1) Short Bridge two-fold

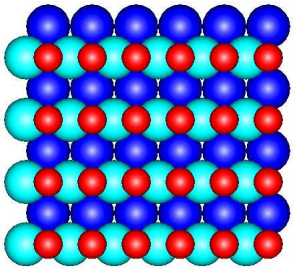

(**d**) (1×1) Short Bridge three-fold

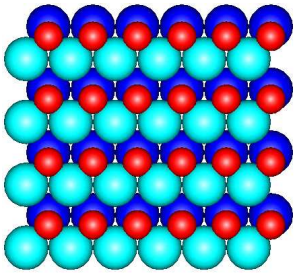

(**e**) (2×1)p2mg Zig-Zag three-fold

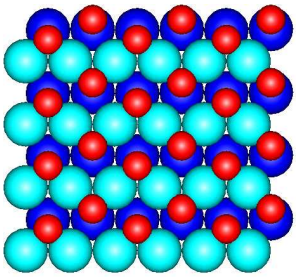

Figure 4.4: (Color) Top view of the full−coverage cells considered in the text. Oxygen atoms are small and shown in red.

eV chemisorption energy.

4.4 Lower coverage adsorption

In this section we consider lower coverage structures, describing how the adsorption site depends on the amount of adsorbates present on the surface. We will find that, passing from $\theta = 1.0$ ML to 0.5 ML, the oxygen site changes from a two−fold to a three−fold one, still remaining on the short−bridge. We will initially consider 0.5 ML structures, then extending our investigation to $1/6$ ML covered surfaces. For the former case we have relaxed both (1×2) and (2×1) cells, with the oxygen in the following sites, also illustrated in Fig. 4.7 and 4.8:

- (**a**): Long Bridge two−fold
- (**b**): Long Bridge three−fold
- (**c**): Short Bridge two−fold
- (**d**): Short Bridge three−fold

In Tab. 4.4 and 4.5 are reported, as in the previous section, structural and energetic information: this time the lowest energy adsorption site is no longer a three−fold one, the system has preferred to move towards the centered two−fold position (2×1)(**c**) on the short−bridge. In this way the chemisorbed adatom has lost the coordination with a second layer rhodium, optimizing the bonding with only two first layer atoms. The optimal chemisorption energy increases by reducing the coverage, passing from −2.12 eV for the (2×1)p2mg 1.0 ML structure to −2.29 eV for the (2×1) short−bridge two−fold 0.5 ML geometry. We report in Fig. 4.5 the oxygen chemisorption energy versus the coverage, calculated for the most stable structures considered (see the following). Passing from 1.0 to 0.166 ML we have found a 0.3 eV increase of the adsorbate stability, pointing to the presence of electronic interaction among the adsorbates, as also noted by Comelli et al. [66]. The second most stable structure is the (2×1) long−bridge two−fold, with a −2.22 eV chemisorption energy, while the short bridge three−fold site has now a −2.15 eV chemisorption energy ((2×1)(**d**)). From a structural point of view, passing from 1 ML to 0.5 ML the oxygen distance from its nearest neighbor is reduced from 2.0 to 1.9 Å, and the bonding angle θ_{1-O-1} passes from 85° to 92°, resulting in a better overlap between oxygen *2p* and rhodium *4d* orbitals [69].

These results confirm that a change in the adsorption site associated to the reduction of the coverage occurs, as observed in HREELS and XPS experiments, but they

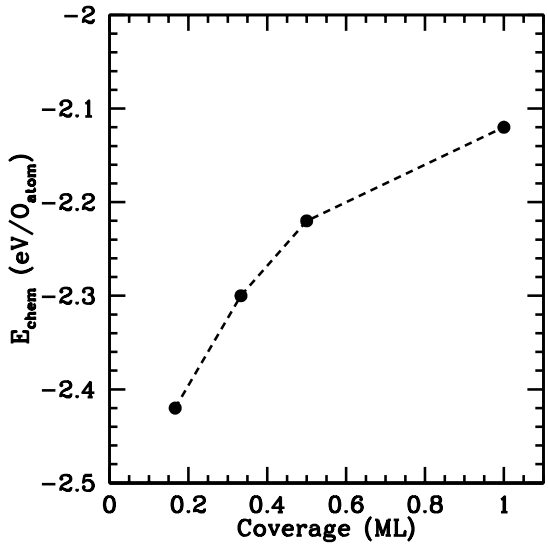

Figure 4.5: Oxygen chemisorption energies as a function of the coverage.

do not agree with the experimetal assignment given for the new adsorption site, since the HREELS data have been interpreted in favor of a long−bridge two−fold position. Recent STM investigations [16] have indeed confirmed our prediction about the low−coverage most stable structure, demonstrating that, at variance with the general trend observed on other transition metal surfaces, oxygen sticks on the low coordinated two−fold short−bridge site when dosed on Rh(110) at low coverage and low temperature.

In order to better characterize the oxygen−metal bond, we have analyzed the PDOS of the two different (2×1) short−bridge structures. In in Fig. 4.6 we plot the electronic density of states projected on the oxygen *s* and *p* orbitals, for the equilibrium (2x1)(**c**) short−bridge centered and the similar (2x1)(**d**) short−bridge three−fold one. In both cases the low energy bonding peaks have a larger weight than the anti−bonding ones, which are also partly depopulated, indicating that the adatoms are charged. The three−fold site oxygen electronic density has, moreover, a much larger contribution to the band−energy than in the two−fold case. This means that the part of band energy coming from oxygen orbitals would have favor the more coordinated three−fold site. Hence the system preference towards the low−coordinated structure is due to the response of the substrate.

To study the adsorption at still lower coverages, we have then considered the same adsorption sites as for the 0.5 ML case, using (2×3) $1/6$ ML supercells. The geometrical and energetics parameters are listed in Tab. 4.6 and 4.7, where we have main-

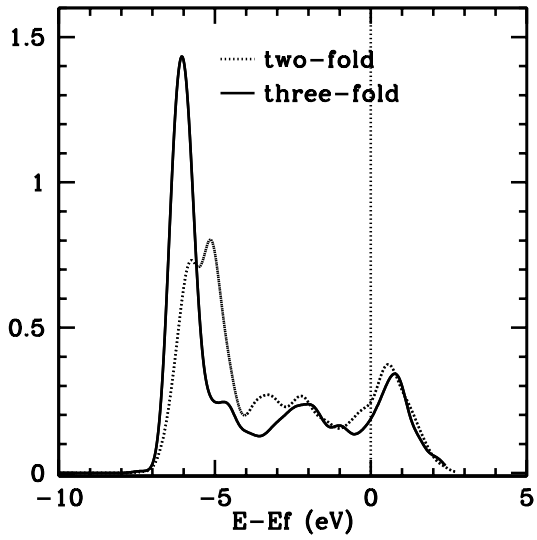

Figure 4.6: Electronic densities of states (arb. un.), projected onto the oxygen's s and p states for the $(2times1)$(**c**) and (2×1)(**d**) structures.

tained the labeling convention used before, indicating with (**a**), (**b**), (**c**) and (**d**) the long−bridge/short−bridge two−fold/three−fold sites. Also for this reduced coverage, the optimal adsorption site is the short−bridge two−fold one, with a chemisorption energy that has increased from -2.29 to -2.42 eV, with respect to the 0.5 ML case. Moreover, the energy difference between the two short−bridge sites (**c**,**d**) has not changed, the two−fold one being 0.130 meV more stable than the three−fold one. The long−bridge two−fold site, instead, has now become less favorable than both the short−bridge sites. The local geometry of the surface has not changed by varying the coverage, as it can be seen comparing the structural data for to the optimal (**c**) site for the 0.5 and 0.166 ML cells. The only parameter varied is the first interlayer relaxation of the metal surface, which is much less reduced (-7.8% instead of -3.9%) in the case of the lower coverage adsorption.

Concluding, the new adsorption site found at 0.5 ML is still optimal at a lower 0.116 ML coverage, with a better chemisorption energy and almost no change in the local geometric distortion of the surface around the oxygen. We thus espect that the described geometry is stable even at lower coverages.

(**a**) (1×2) Long Bridge two-fold

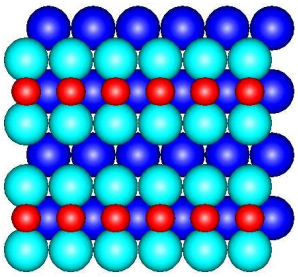

(**b**) (1×2) Long Bridge three-fold

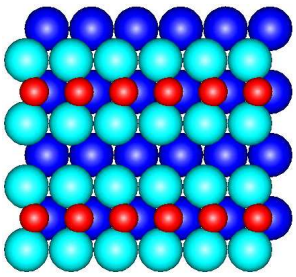

(**c**) (1×2) Short Bridge two-fold

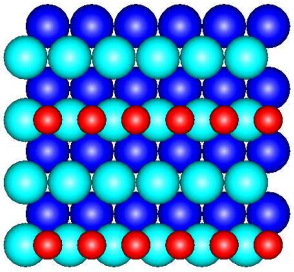

(**d**) (1×2) Short Bridge three-fold

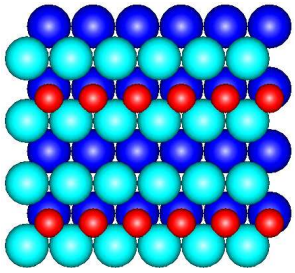

Figure 4.7: (Color) 0.5 ML (1x2) cells.

STRUCT.	$\bar{z}_{O-1}$ (Å)	d_{O-O} (Å)	d_{O-1} (Å)	d_{O-2}	θ_{1-O-1} (°)	θ_{1-O-2} (°)	Δ_{12} (%)
1×2(**a**)	0.90	2.67	1.97	2.70	126	67	−2.5
1×2(**b**)	0.64	2.67	2.84	2.35	130	79	−7.6
1×2(**c**)	1.49	2.67	1.93	3.34	88	54	−3.8
1×2(**d**)	0.63	2.67	2.01	2.01	83	86	−4.9
2×1(**a**)	0.66	3.80	1.97	2.37	145	76	−4.0
2×1(**b**)	0.64	3.80	2.16	2.01	123	79	−6.4
2×1(**c**)	1.32	3.80	1.90	3.27	92	56	−3.9
2×1(**d**)	0.71	3.80	2.01	2.06	88	81	−6.2

Table 4.4: 0.5 ML cells structural data, symbols as in Tab. 4.2.

(**a**) (2×1) Long Bridge two-fold

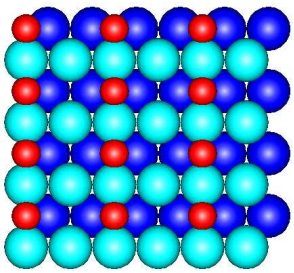

(**b**) (2×1) Long Bridge three-fold

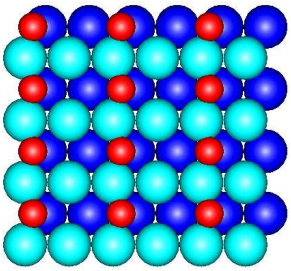

(**c**) (2×1) Short Bridge two-fold

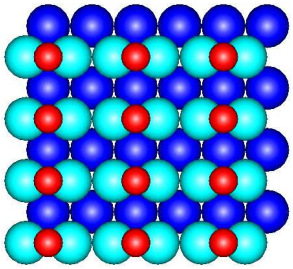

(**d**) (2×1) Short Bridge three-fold

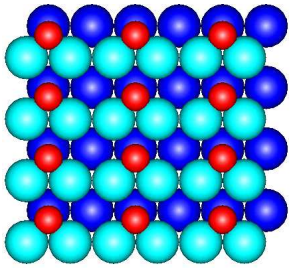

Figure 4.8: (Color) 0.5 ML (2x1) cells

STRUCT.	1×2 (**a**)	1×2 (**b**)	1×2 (**c**)	1×2 (**d**)
E_{chem} (meV/O_{atom})	−1.84	−1.83	−1.78	−2.02
STRUCT.	2×1 (**a**)	2×1 (**b**)	2×1 (**c**)	2×1 (**d**)
E_{chem} (meV/O_{atom})	−2.22	−1.81	−2.29	−2.15

Table 4.5: Chemisorption energies for the various 0.5 ML cells considered.

STRUCT.	$\bar{z}_{O-1}$ (Å)	d_{O-O} (Å)	d_{O-1} (Å)	d_{O-2} (Å)	θ_{1-O-1} (°)	θ_{1-O-2} (°)	Δ_{12} (%)
(2×3)(**a**)	0.96	3.80	1.99	2.72	122	65	−7.3
(2×3)(**b**)	0.72	3.80	2.09	2.05	125	78	−8.9
(2×3)(**c**)	1.37	2.67	1.91	3.27	92	56	−7.8
(2×3)(**d**)	0.76	2.67	2.03	2.04	85	83	−3.0

Table 4.6: $1/6$ ML cells structural data, symbols as in Tab. 4.2.

STRUCT.	2×3 (**a**)	2×3 (**b**)	2×3 (**c**)	2×3 (**d**)
E_{chem} (meV/O_{atom})	−1.97	−2.11	−2.42	−2.29

Table 4.7: Chemisorption energies for the various 0.166 ML cells considered.

4.4.1 Oxygen pairs

We have studied the formation of oxygen pairs, performing several constrained relaxations of the aforementioned (2×3) structure, fixing the O−O distance to several values ranging from 0.2 to 3.8 Å and relaxing all the others ionic coordinates. In all the cases the initial structure for the relaxation has been chosen to be with oxygen molecule in the vacuum, far from the surface. At the end the oxygen pairs were sticked on the surface. In Fig. 4.9 we present the energetics and some geometric parameters of the studied system, for different values of the constrained distance. No tendency towards formation has been observed. The system, in fact, relaxes to a structure with O atoms in their relative short−bridge sites, for all the considered values of the constrained parameter. Also in this case both the oxygen−metal bonding lengths and angles are very similar to those found for the θ = 0.5 case, while the first interlayer relaxation has a value intermediate between that of the 0.5 ML and 0.166 ML structures ($\Delta_{12} \sim -5.5$ %).

We have also considered the effect of a possible surface magnetic structure on the

STRUCT.	$\bar{z}_{O-1}$ (Å)	d_{O-O} (Å)	d_{O-1} (Å)	d_{O-2} (Å)	θ_{1-O-1} (°)	θ_{1-O-2} (°)	Δ_{12} (%)
(2×3)(dimer)	1.33	2.67	1.91	3.28	91	56	−5.5

Table 4.8: $1/3$ ML cells data, referring to the final dimer structure, symbols as in Tab. 4.2.

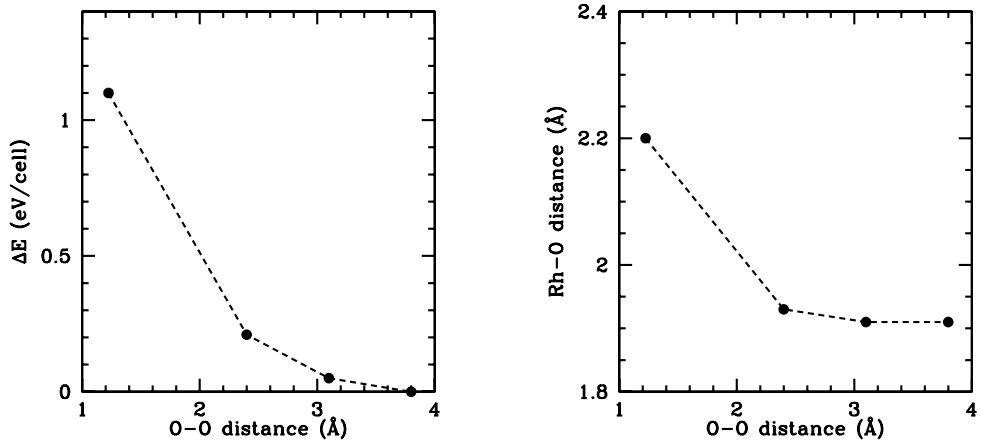

Figure 4.9: Energy and Rh−O distance for the (2×3) cells with oxygen dimers, varying the constrained distance between the oxygens forming a pair.

formation of the pairs. We have thus relaxed the system using LSDA, with the GGA NLCC pseudopotential described in Chap. 3. The starting magnetic state was chosen with the O_2 molecule in its triplet state and the Rh(110) surface with a 1.0 μ_B/atom magnetization. The results, however, indicate that both the oxygen and the surface atoms lose their initial magnetization, relaxing towards the already found paramagnetic ground state.

Finally, to check if the reduced O−O distance in the observed oxygen pairs was possibly due to a misinterpretation of the experimental STM images—which, in the Tersoff and Hamann formalism [81], are proportional to the local density of states at the Fermi energy—we have simulated the STM images for our equilibrium structure, as described in [79]. We found that the calculated STM profile of our structure, which don't present formed pairs, is indeed characterized by oxygen peaks centered at the true position of the oxygen atoms, thus indicating the correct O−O bonding distance. Thus we conclude that the measured STM images can be considered as a faithfull representation of the surface morphology, and that the reason for our discrepancy has to be sought elsewhere. In particular we have not kept into account the role thermal effects may possibly have on the surface geometry.

4.5 Conclusions

Altough we have not been able to describe theoretically the observed oxygen pairs formation, at least using LDA or GGA approximations, our investigation has resulted in a detailed structural characterization of the low−coverage oxygen phases on Rh(110),

which was previously debated experimentally. We have, in fact, described the correct equilibrium adsorption states, studying the coverage dependent site change described in the literature.

Chapter 5

Oxygen and aluminum adsorption on Pd(100)

In recent years there has been considerable interest in understanding the driving force for the (2×2)p4g symmetry reconstructions on fcc(100) transition metal surfaces, induced by the adsorption of light elements [18]. The structure of this distortions is characterized by a (2×2) periodicity with two orthogonal glide lines (see Fig. 5.1). In particular, much is known about C/Ni(100), N/Ni(100) and O/Rh(100) systems, which present such surface displacive reconstructions when half a monolayer of adsorbates is deposited. In these cases, adatoms initially sit in the hollow sites with a c(2×2) symmetry, which is then reduced to (2×2)p4g because of a rhomboid distortion of every other surface metal hollows (see Fig. 5.1). Actually, two different microscopic structures can lead to the same in−plane symmetry and LEED pattern (see Fig. 5.2). In the first one—which was named *white* reconstruction in Ref. [82] and which occurs in O/Rh(100)—two of the four metal atoms neighboring the adsorbate atom strengthen their bond with the latter, thus getting closer to each other. As a consequence, the occupied square hollows deform and become rhombi, while the empty hollows are expanded. In the other case—which was named *black* reconstruction and occurs in C/Ni(100) and N/Ni(100)—the adsorbate penetrates into the square hollows, enlarging them and deforming the empty hollows into rhombi. From both an experimental and a theoretical point of view, it is known that half a monolayer of oxygen induces a *white* type of reconstruction on Rh(100), while the O/Ni(100) surface is instead not deformed [82]. O/Pd(100) is in some sense intermediate between these two cases, because palladium is isoelettronic to nickel, but it also has a lattice parameter closer to that of rhodium. Experimentally it is found that O/Pd(100) does not present this kind of reconstruction [83, 84], and in the first part of this chapter we will discuss the physical reasons for such a behavior.

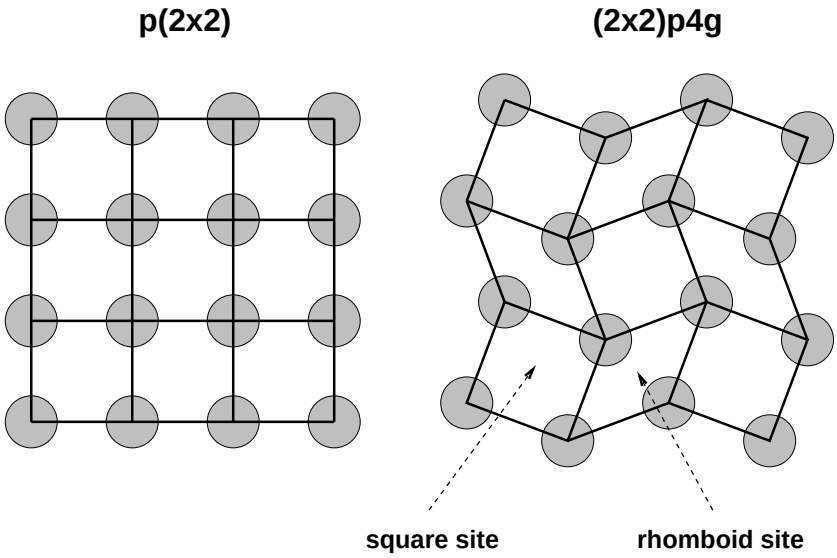

Figure 5.1: Schematic view of the (2×2)p4g reconstruction pattern of an fcc (100) surface.

We will initially consider oxygen adsorption on Pd(100), at various coverages, verifying how this system is indeed stable against the (2×2)p4g reconstructions. Then—by comparing the geometry and the electronic structure of the oxygen c(2×2) phases on Rh(100), Pd(100) and Ni(100)—we will give some arguments to understand the electronic and steric effects that make such distortions energetically not favored. In the second part of the chapter we will consider Al adsorption on Pd(100), which has been found to induce a reconstruction with the same symmetry. In this case, however, the microscopic surface structure is different from those described earlier, in that after annealing Al adsorbs in subsurface sites, forming an ordered alloy in the second metal layer. Our investigation will allow to discriminate between the different structural models that have been proposed in the literature. Finally, we will also describe the effect of oxygen adsorption on the reconstructed Al/Pd(100) surface.

5.1 Computational details

We have used Vanderbilt GGA pseudopotentials [32] for Rh, Pd, Ni and O, generated within the RRKJ3 scheme [37]. The oxygen and the rhodium pseudopotentials are the same used in Chap. 3, while that for palladium has one projector for the *5p* states, two for the *4d* channel and *5s* locality. The calculated lattice parameter for Pd is is 3.98 Å, whereas the experimental data is 3.89 Å. The theoretical and experimental bulk modulus

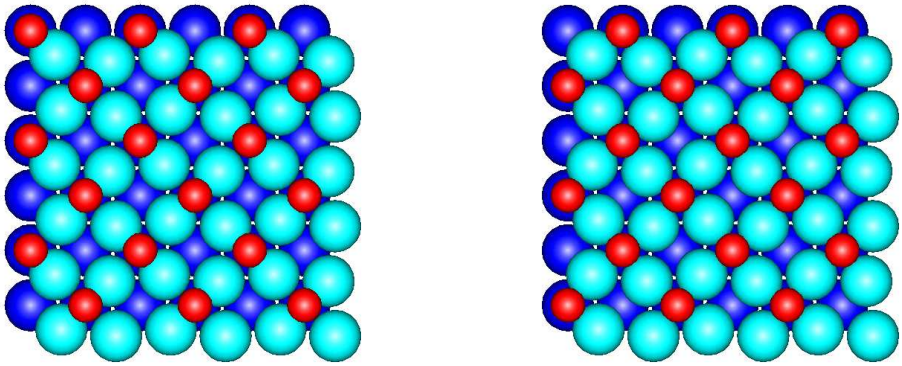

Figure 5.2: (Color) Oxygen−induced *white* (left) and *black* (right) (2×2)p4g symmetry reconstructions. Oxygen atoms are smaller and shown in red

is, instead, 160 and 195 kbar, respectively. The nickel pseudopotential has two projectors for *s*, *p* and *d* states. The calculated Ni lattice parameter and bulk modulus are 3.52 Å and 185.6 kbar, respectively. The experimental values are 3.52 Å and 180 kbar. Al, instead, has been described by a norm−conserving pseudopotential with two projectors for both the *3s* and the *3p* states. The calculated Al lattice parameter and bulk modulus are 4.05 Å and 774 kbar, while the experimental values are 4.04 Å and 760 kbar. All the calculations have been performed using (7+5) supercells, sampling the Brillouin zone with a 0.3 eV gaussian smearing [27] and a (11×11×1) Monkhorst & Pack **k**−point mesh [39] for (1×1) cells (21 **k**−points in the irreducible wedge of the IBZ). For (2×2) cells we have chosen a (4×4×1) mesh which has 3 inequivalent **k**−points. We have used 27 and 162 Ry cutoffs for the wavefunctions and charge grids, respectively, verifying that our numerical accuracy is sufficient to estimate chemisorption energies differences with an error of ~ 30 meV/O_{atom}.

5.2 Oxygen adsorption on Pd(100)

5.2.1 Clean and full coverage surface

We have initially considered the clean Pd surface, whose surface interlayer relaxations are shown in Tab. 5.1, together with the results of other calculations [85] done with LDA and a mixed−basis pseudopotential scheme. We have then studied the oxygen adsorption site preference at $\theta = 1$ML coverage, considering the four−fold hollow site, the two−fold bridge and the one−fold top sites. In Tab. 5.2 we report the energetical and structural parameters where, as usual, the chemisorption energies are referred to the

	Δ_{12} (%)	Δ_{23} (%)	Δ_{34} (%)
GGA	-2.6	-0.9	-0.8
Other calc. [85]	-1.2	0.0	0.0

Table 5.1: Calculated surface relaxations for the clean Pd(001) surface.

	E_{chem} (eV/O_{atom})	Δz_{O-Pd_1} (Å)	d_{O-Pd_1} (Å)	Δ_{12} (%)	Δ_{23} (%)
Hollow	-0.24	0.70	2.11	11.2	-1.2
Bridge	-0.21	1.37	1.96	1.9	-0.9
Top	0.72	1.85	1.85	1.6	0.4

Table 5.2: Energetic and structural data for the full coverage O/Pd(001) structures considered.

clean surface and a spin−polarized O_2 molecule. The top site turns out to be unstable, while the hollow and bridge sites have a small but exothermic chemisorption energies of -0.24 and -0.21 eV/O_{atom}, respectively. Such small adsorption energies make it difficult even to state that these structures will be stable in real samples, because of the approximations used. The O−Pd bonding distance is smaller in the two−fold bridge site (1.96 Å) than in the hollow site (2.11 Å). In this last structure, moreover, oxygen atoms sit nearer to the first surface layer (0.70 Å), whereas in the bridge site O stays 1.37 Å above the surface. Finally, in the hollow site, oxygen adsorption induces a very large relaxation of the fist interlayer Pd distance, which is $\sim$ 11 % and that will be reduced for smaller coverages.

5.2.2 Adsorption and reconstruction at lower coverage

We now consider the oxygen adsorption structures at lower coverage. In particular, we will study $\theta = 0.5$ ML and 0.25 ML oxygen covered surfaces, simulated with c(2×2) and p(2×2) structures, respectively. We will restrict our attention to hollow sites only, because we have verified that the competing bridge site is unfavored with respect to the former already for $\theta = 0.25$ ML, where it has a chemisorption energy which is 0.24 eV/O_{atom} higher. In Fig. 5.3 we present a top view of the two considered structures, whereas in in Tab. 5.3 we list all the calculated parameters.

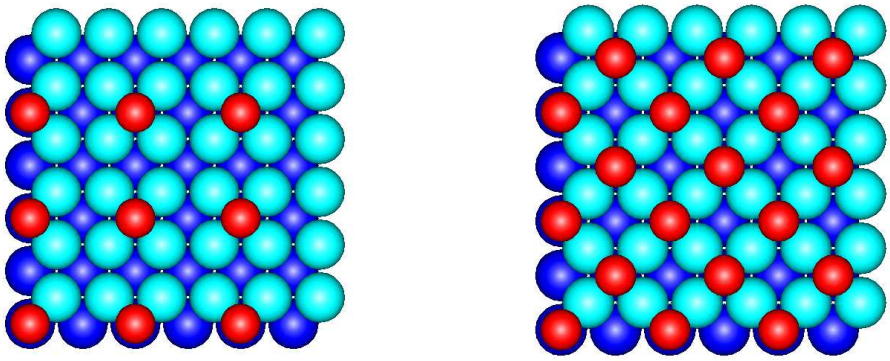

Figure 5.3: (Color) Unreconstructed O/Pd(100) p(2×2) (left) and c(2×2) (right) structures considered in the text. Oxygen atoms are smaller and shown in red.

	E_{chem} (eV/O_{atom})	Δz_{O-Pd_1} (Å)	Δ_{lat-Pd_1} (Å)	Δz_{Pd_2} (Å)	d_{O-Pd_1} (Å)	Δ_{12} (%)	Δ_{23} (%)
p(2×2) Hollow	−1.14	0.90	0.01	0.15	2.18	0.3	−0.87
p(2×2) Exp		0.83±0.02	±0.015	0.12	2.11	0.5±2.5	−3.0±2.5
c(2×2) Hollow	−0.92	0.78	0.0	0.0	2.14	4.6	0.5
c(2×2) Hollow	White Rec.	UNSTABLE					
c(2×2) Hollow	Black Rec.	UNSTABLE					

Table 5.3: Energetic and structural data for the 0.25 and 0.5 ML O/Pd(001) structures.

Oxygen chemisorption is now much more stable than in full coverage case. For the 0.5 ML c(2×2) hollow structure, in fact, $E_{chem} = -0.92$ eV/O_{atom} while in the 0.25 ML p(2×2) $E_{chem} = -1.14$ eV/O_{atom}. The oxygen height over the surface Δz_{O-Pd_1} increases lowering the coverage, passing from 0.78 to 0.90 Å in the c(2×2) and p(2×2) structures, respectively. This trend may be rationalized in terms of the electrostatic repulsion among the charged adsorbates. At high coverage the Coulomb repulsion among oxygen atoms is greater. As a consequence they prefer to enter in the metal hollows and shield their mutual interaction. At low coverage the Coulomb repulsion is less effective and the adatoms can freely optimize their distance from the metal atoms, thus getting higher above the surface plane. The surface interlayer distance relaxations Δ_{12}, moreover, are now much reduced and pass from 4.6% at $\theta = 0.5$ ML to 0.3% at $\theta = 0.25$ ML. In the p(2×2) structure Pd atoms lying in the same layer are no longer equivalent: as a consequence the first layer atoms present an in−plane lateral shift Δ_{lat-Pd_1} =0.01 Å, expanding the hollows occupied by the adatoms. In a similar fashion, the second layer

atoms get vertically buckled with $\Delta z_{Pd_2} = 0.15$ Å. For this last structure we have been able to compare our findings to LEED−IV data [86], which are reported in Tab. 5.3, with a very good overall agreement.

In order to study the stability of the system against the (2×2)p4g−symmetry reconstructions, we checked that both the *black* and the *white* reconstructions are unstable against the unrelaxed c(2×2) 0.25 ML structure. We thus predict O/Pd(100) to be stable against the displacive distortions observed in O/Rh(100) or N/Ni(100) and C/Ni(100), in agreement with the experimental evidence [83, 84]. In the following we discuss the electronic structure of the O/Pd(100) system, claryfing how the O−Pd chemical bonding does not lead to any reconstruction.

5.2.3 O/Pd(100) vs. O/Rh(100) and O/Ni(100)

Previous work [82] has allowed to understand the mechanism responsible for the *black*/*white* (2×2)p4g reconstructions in O/Rh(100), C/Ni(100) and N/Ni(100). The general trend emerging from these studies is that when the adsorbate is small enough to penetrate the hollows—staying $\sim$ 0.1 Å above the surface as in C/Ni(100) and N/Ni(100)—the interaction between the adatom p_z and the metal d_{xz}/d_{yz} orbitals gives the main contribution to the energetic balance, favoring the distorted *black* geometry. In the case of O/Rh(100), the calculations have demonstrated that the overlap between the aforementioned orbitals is no more effective, because of the greater height of the adsorbed atoms over the surface ($\sim$1Å). The electronic mechanism responsible for the *white* reconstruction is, in fact, related to the interaction of the oxygen p_x and p_y orbitals with the metal d_{xz} or d_{yz} states. In this case two of the four O−metal bonds of the occupied hollows get stronger and shorter, distorting the occupied hollows and finally achieving the *white* type of reconstruction.

To shed some light on the O−metal bonding for O/Pd(100), we have compared it with analogous c(2×2) O/Rh(100) and O/Ni(100) structures.[1] Actually, the Rh geometry we have considered is metastable, since we know it to undergo a transition to a *white* structure [83, 84] (see Fig. 5.2). It is indeed a constrained minimum, forced to have the c(2×2) symmetry. The electronic structure of the three systems reveals their main differences. In Fig. 5.4 we show the projected electronic densities of states for O/Rh(100), O/Pd(100) and O/Ni(100). We present the contributions coming from oxygen p_x and p_z orbitals (p_y states are degenerate with the p_x), and the first layer metal d_{xz} and d_{yz}

[1] Ni magnetism has not been kept into account, since previous studies have demonstrated it not to be important for the description of the O−Ni surface bond [82].

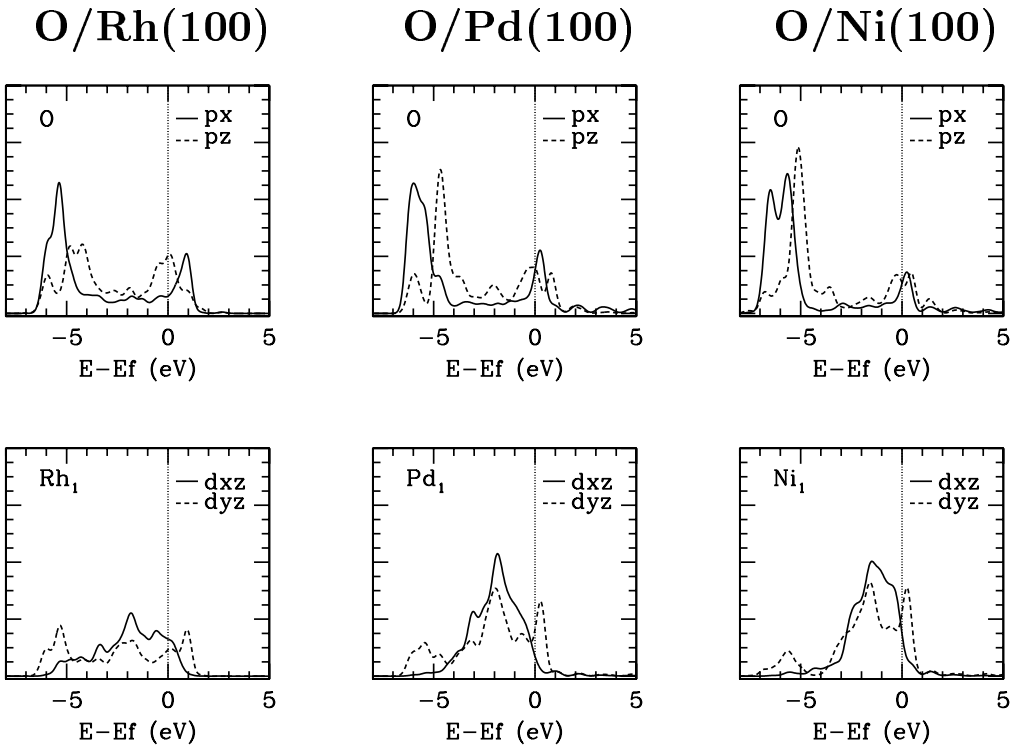

Figure 5.4: Projected densities of states for the oxygen p_x/p_y and first−layer metal atoms d_{xz}/d_{yz} states of the O/Rh(100), O/Pd(100) and O/Ni(100) systems discussed in the text.

components. We note that O/Rh(100) is mainly stabilized by the interaction of the oxygen p_x/p_y states with the metal d bands, and that the bond is stronger in this system than in the other two because the majority of the anti−bonding p levels is situated above the Fermi energy. The main difference is , however, in the relative weight of the bonding p_x/p_y and p_z contributions. In O/Rh(100), in fact, the p_z bonding peak at ~ -4.5 eV is much less important than the p_x/p_y one at ~ -5.5 eV (see Fig. 5.4). On the contrary, in O/Pd(100) and O/Ni(100) both the p_z and p_x/p_y contributions are important. Thus in O/Pd(100) and O/Ni(100) both the mechanisms leading to the different *black* and *white* reconstructions—namely, the oxygen p_z and p_x/p_y interactions with the metal—are active, and the energetic balance does not favor any of them, in such a way that the surface does not reconstruct.

5.3 Al adsorption on Pd(100)

In this section we study the effect of aluminum adsorption on Pd(100) [19, 87]. Recent experimental data [19] indicate that the clean Pd(100) surface undergoes a morphological transition to a phase with (2×2)p4g symmetry when Al is dosed on it [88]. Even if the surface symmetry of this new structure is the same of the previously discussed examples, its geometry will be found to be different, resembling that of a surface substitutional alloy. The first experimental evidence of such a transition has been given by Onishi et al. [88], who performed a LEED study of the Al/Pd(100) system at various temperatures. They found a strong (2×2)p4g interference pattern after annealing the surface, but they were not able to characterize the structure any further. Later Shen et al. [19] performed LEED and low energy ion scattering (LEIS) experiments giving a much better characterization of the system. They found that Al adsorption at room temperature removes the clean surface (1×1) LEED signal—a fact consistent with a random distribution of Al atoms above the surface—and LEIS data predict that Al is adsorbed on the surface. By annealing the sample at 900 K°, the system acquires the (2×2)p4g symmetry and LEIS indicates that Al has been incorporated into the bulk. The stoichiometry of the system has been accurately described, finding that in the (2×2)p4g phase the first Pd layer is practically clean, whereas the second layer has a mixed composition, with almost equal abundances of Al and Pd atoms. Remarkably, the described stoichiometry is found to be very stable also increasing the Al coverage up to 4.7 ML. The authors of Ref. [19] have also proposed a structural model, based on the comparison between the experimental data and classical dynamical simulations of the ions impinging on the surface. The proposed structure is shown in Fig. 5.5. Following the convention adopted before, we name it as *black* reconstruction. According to this model the first surface layer is composed by Pd atoms, while the underlayer is made by Al and Pd atoms situated in the fcc sites, with equal abundances and a checkerboard c(2×2) disposition. Because of a 0.25 Å vertical buckling of the second layer Al atoms getting closer to the surface, the first layer hollows over each Al atom enlarge, thus deforming the other hollows into rhombi. The in−plane lateral shift of the first layer Pd atoms Δ_{lat-Pd_1} has been estimated to be 0.5 Å. Further LEED−IV investigations [87] have instead proposed a different model, which is also shown in Fig. 5.5. We name it as *white* reconstruction. Such a structure is indeed very similar to the one just described, it is obtained by exchanging the Al and Pd atoms of the second layer in the *black* model. A skematic side view is given in Fig 5.6. This time the second layer Pd atoms are buckled 0.25 Å towards the surface, while the first layer hollows over the Al atoms are distorted into rhombi, with a 0.57 Å Δ_{lat-Pd_1}

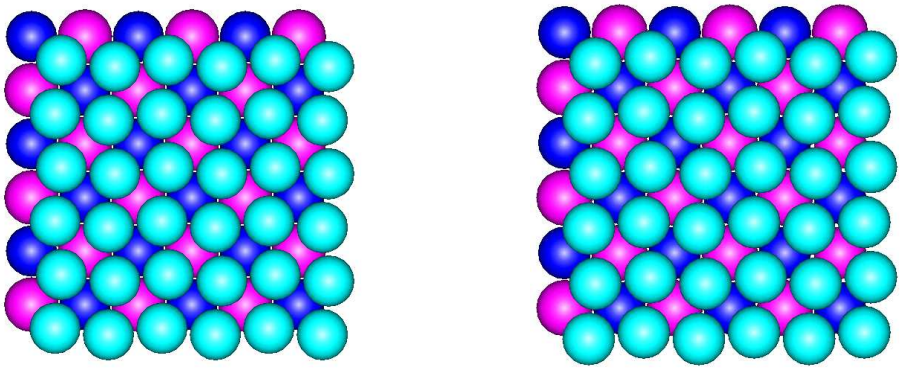

Figure 5.5: (Color) Aluminum−induced *white* (left) and *black* (right) (2×2)p4g symmetry reconstructions. Al atoms are bigger and shown in pink.

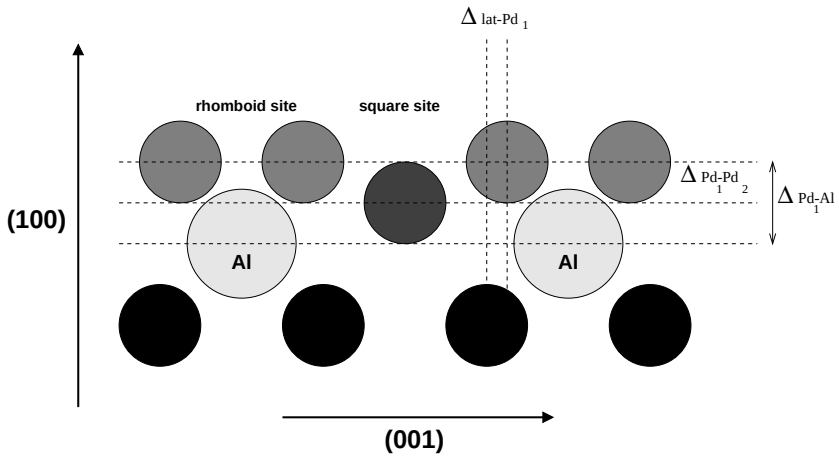

Figure 5.6: Side view of the *white* model for Al/Pd(100).

lateral shift.

Some previous theoretical work has been performed by Watari et al. [89], who compared the stability of the experimentally proposed *white* model with an unreconstructed structure, in which the first layer Pd atoms are not relaxed laterally, nor the Al−Pd underlayer is vertically buckled. They have used DFT and cluster geometries—performing two single-point calculations without relaxing ionic positions—to predict the stability of the *white*−reconstructed with respect to the unreconstructed structure, the stabilization energy being $\Delta E \sim 0.2$ eV/cell. However, they did not consider the proposed *black* reconstruction.

	ΔE (eV/cell)	Δ_{lat-Pd_1} (Å)	Δz_{Pd_1-Al} (Å)	$\Delta z_{Pd_1-Pd_2}$ (Å)	Δ_{12} (%)	Δ_{23} (%)
Black rec.	0.29	0.0	1.81	1.92	-7.6	-4.0
White rec.	0.0	0.41	2.06	1.83	-2.1	-1.1
Exp. (LEIS)		0.5	1.7±0.1	1.95		
Exp. (LEED-IV)		0.57±0.1	2.1±0.06	1.85±0.06		

Table 5.4: Experimental and theoretical data for the reconstructed Al/Pd(100) surface.

5.3.1 (2×2)p4g reconstruction

In this section we consider the energetics of the *black* and *white* structural models for Al/Pd(100). We have chosen the experimentally proposed structures as starting configurations for our optimizations. The *black* reconstruction has turned out to be unstable, in the sense that its calculated equilibrium structure does not present any lateral shift of the first layer Pd atoms, having a higher c(2×2) symmetry. The total energy of this geometry is 0.290 eV/cell higher than that for the optimized *white* one, which is indeed distorted. The first layer of the the calculated *white* model, in fact, still presents the desired (2×2)p4g symmetry as the LEED−IV data has evidentiated. The comparison with the LEED−IV structural parametres is indeed very good. The lateral displacement Δ_{lat-Pd_1} is 0.41 Å—the experimental value being 0.57 Å— and the vertical buckling of the mixed underlayer $\Delta z_{Pd_1-Pd_2}$ is 0.23 Å, while LEED−IV gives 0.25 Å [87]. Thus, even though the real structure of the Al/Pd(100) surface alloy may be somehow different from what we supposed, our results yield the first ab-initio confirmation of the *white* kind of reconstruction, as predicted by the quantitative LEED−IV analysis.

5.3.2 Oxygen adsorption on Al/Pd(100)

In this last section we present some preliminary results on the effect of oxygen adsorption on the (2×2)p4g−reconstructed Al/Pd(100) surface. LEIS data have demonstrated how oxygen adsorption on Al/Pd(100) is able to remove the (2×2)p4g reconstruction, segregating Al atoms from the second to the first surface layer. Nevertheless, both the initial O adsorption site and the final unreconstructed surface geometry are unknown. In particular, experiments have not been able to state whether Al atoms will be situated in first layer fcc sites, or will stay above the surface as O atoms do [19]. Here we try to determine the most stable O adsorption site and we propose a model for the O−covered unreconstructed surface.

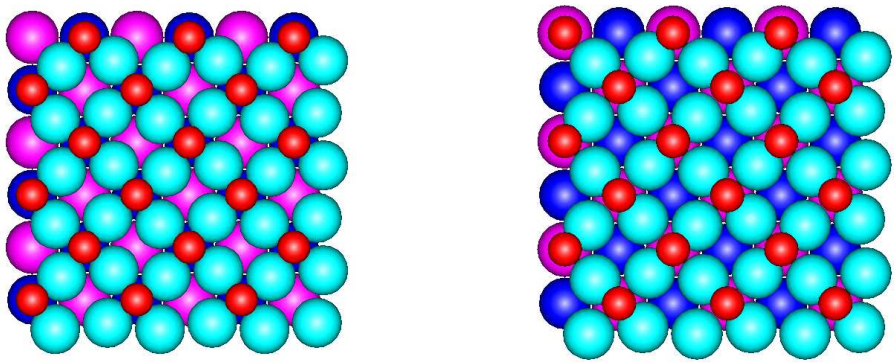

Figure 5.7: (Color) Oxygen adsorption on the squares (left) and rhomboid (right) sites of the reconstructed Al/Pd(100) surface.

Since there is experimental evidence that the O and Al coverages are equal [19], we have restricted our investigation to 0.5 ML structures with the same number of Al and O atoms. We have considered two possible O adsorption sites on the reconstructed Al/Pd(100), which are shown in Fig. 5.7. In particular, we have calculated the energetics and the geometry of O staying above the square and rhomboid hollows of the surface. Our results are shown in Tab. 5.5, where the chemisorption energies are referred to the reconstructed Al/Pd(100) surface. We note that both sites are stable, and that the equilibrium one is the square hollow ($E_{chem} = -0.83$ eV/O_{atom}). Its structure reveals that O adsorption reduces the in−plane distortion Δ_{lat-Pd_1}—which is now 0.43 Å—thus being consistent with the observation that O tends to remove the distortion.

Finally, to study whether Al will segregate over the surface or it will be included in the first layer, we have simulated two different unreconstructed c(2×2) structures that realize one or the other choice (see Fig. 5.8). In the first geometry, which we name S_1, both the oxygen and the aluminum atoms sit in super−surface hollow sites, with a c(2×2) disposition, on the clean Pd surface. In the latter, named S_2, Al is incorporated in the first surface layer while oxygen is still situated in the hollow sites. The results are shown in Tab. 5.6, where we also presents the surface energy differences ΔE^{surf} with respect to the already discussed structure with O in the square hollows of the reconstructed Al/Pd(100) surface. We note that the S_1 structure turns out to be less favorable than the reconstructed one— $\Delta E^{surf} = 3.65$ eV/cell—while the S_2 geometry has indeed stabilized the system, ΔE^{surf} being -0.96 eV/cell.

We thus predict that O will adsorb on the square hollow of Al/Pd(100), and that in the final reconstructed surface Al atoms will be segregated in first layer fcc sites, since the adsorption of both Al and O atoms above the surface is energetically forbidden. This

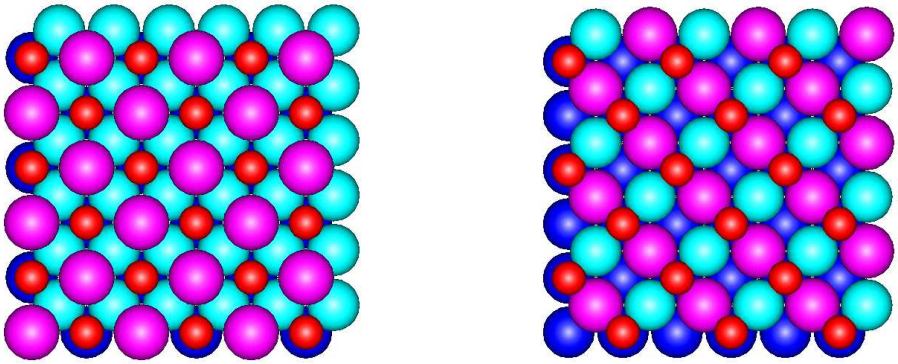

Figure 5.8: (Color) Oxygen adsorption on the considered S_1 (left) and S_2 (right) unreconstructed Al/Pd(100).

behavior is consistent with some previous guess based on LEIS data [19], and can be understood in terms of the stronger bond between Al−O than Pd−O [19].

	E_{chem} (eV/O_{atom})	Δ_{lat-Pd_1} (Å)	Δz_{O-Pd_1} (Å)	d_{O-Pd_1} (Å)	Δz_{Al-Pd_1} (Å)	d_{Al-Pd_1} (Å)
Hollow site	−0.81	0.43	0.81	1.75	2.08	1.93
Rhomboid site	−0.38	0.50	1.33	1.95	2.13	1.89

Table 5.5: Theoretical data for oxygen adsorption on the reconstructed Al/Pd(100) surface.

	ΔE^{surf} (eV/cell)	Δz_{O-Pd_1} (Å)	Δz_{Al-Pd_1} (Å)	d_{O-Pd_1} (Å)	d_{Al-Pd_1} (Å)	d_{O-Al} (Å)
S_1 struct.	+3.65	1.55	1.51	2.52	2.49	2.81
S_2 struct.	−0.96	0.57	−0.37	2.07	2.00	2.20

Table 5.6: Theoretical comparison between the two unreconstructed Al/Pd(100) surfaces, with chemisorbed oxygen.

5.4 Conclusions

In this chapter we have analyzed the electronic effects governing a very common reconstruction of fcc(100) surfaces. In particular, we have elucidated the different chemical bonds that lead O/Rh(100) to reconstruct and, on the other side, O/Ni(100) and

O/Pd(100) to be stable with c(2×2) symmetry. Furthermore, we have presented the first ab-initio description of the surface reconstruction occurring for Al adsorption on Pd(100), and identified the correct structural model among those proposed in the literature. In addiction, we have studied oxygen coadsorption on the Al/Pd(100) surface, showing that O makes Al moving from the second to the first surface layer.

Conclusions

In this thesis we have discussed several aspects of surface adsorption and surface electronic structure. The field of theoretical modelling of surface phenomena has nowadays reached such a degree of maturity that accurate, parameter-free ab-initio calculations can proceed, hand in hand, with the experimental investigations of surface science, yielding important information that is not directly accessible to the experiment.

Our study of O/Ag(100) is a typical example of such a collaborative effort. The O/Ag(100) system is not very well characterized from the experimental point of view, and the only real-space investigation of this system is due to the group of M. Rocca in Genova. We have analyzed both the unreconstructed and the $(2\sqrt{2} \times \sqrt{2})$ phases of O/Ag(100), yielding structural information in good agreement with existing experimental data. We have also addressed the energetics of the $(1\times1)\rightarrow(2\sqrt{2} \times \sqrt{2})$ phase transition, considering the effect of subsurface oxygen. Our results indicate that the real morphology of the missing-row surface is probably different from that which had emerged in the XPD study, and it is indeed similar to the one observed in O/Cu(100). For the same system we have also analyzed how O adsorption and the missing-row reconstruction affect the surface electronic states present on the clean surface.

The investigation of Rh surfaces, instead, is due to a collaboration with the group of R. Rosei and A. Paolucci at the Elettra synchrotron radiation facility in Trieste. The possibility that Rh(100) surface may present a spontaneuous surface magnetization has long been debated. Since both the experimental and the theoretical works have not been able to provide a definive answer to such a problem, we have performed a systematic study of surface magnetization at Rh (111), (110) and (100) surfaces, using a recently developed constrained DFT scheme. Our results have clarified the influence of the surface coordination on the magnetic properties, showing that Rh surfaces have a much larger magnetic susceptibility than their bulk phase, and that the more open Rh(110) surface has indeed a larger susceptibility than the other more compact structures. Even though the approximations adopted have not allowed us to provide any definitive prediction about the observed small surface magnetization, we have pointed out how a further

reduction of the surface atomic coordination—like that occurring in the (1×2) missing-row structures observed in Rh(110)—can greatly enhance the system's tendency to magnetize. We have then characterized the low-coverage phase for O/Rh(100), describing the change of adsorption site. Our results, at variance with previous HREELS experiments [70], have predicted a different equilibrium geometry, later confirmed by STM investigations [16]. Unfortunately we have not been able to describe the formation of oxygen pairs on the Rh(110) surface.

In the last chapter we have considered the electronic effects at the basis of the (2×2)p4g reconstruction of fcc (100) transition metal surfaces. We have been able to understand how the O/Pd(100) system is indeed observed to be stable against the kind of reconstruction occurring in O/Rh(100), presenting a different kind of O-metal chemical bond. We have then turned our attention to the Al-induced (2×2)p4g reconstruction of Pd(100). For this system many experimental investigations exist, and there is a large consensus that Al is adsorbed in second layer fcc sites, with a site exchange with Pd atoms. We have presented the first extensive ab-initio investigation of this system. Our study has been able to discriminate between the two structural models proposed in the literature. Moreover, we have also predicted that O adsoprtion on the reconstructed Al/Pd(100) surface removes the reconstruction, and induces Al to move from the bulk to the surface fcc sites. These last findings are in good agreement with some experimental guesses, but remain to be confirmed.

Appendix A

DIIS diagonalization method

In this appendix we illustrate a rather recent diagonalization technique that we have successfully implemented. The main motivation for this effort stems from the fact that, for large enough systems, the diagonalization step of the self-consistent calculation is the most time-consuming.

All the modern algorithms used to solve the KS equations belong to the class of iterative solvers. In particular, they are aimed at finding the lower portion of the spectrum, and they don't keep in memory the entire Hamiltonian matrix $\hat{H}$, needing only a fast procedure to calculate, given an arbitrary vector $|\Psi\rangle$, the corresponding matrix$-$vector product $\hat{H}|\Psi\rangle$. This is indeed the case using PW's, where the application of the different part of the Hamiltonian operator can be done efficiently using Fourier-transform techniques.

Among all the different iterative procedures, the great majority uses the variational properties of the Rayleigh quotient of a given trial vector $|\Psi_T\rangle$, defined as:

$$r(\Psi_T) = \frac{\langle\Psi_T|\hat{H}|\Psi_T\rangle}{\langle\Psi_T|\hat{S}|\Psi_T\rangle} \tag{A.1}$$

which has an unconstrained minimum at the system ground state $|\Psi_0\rangle$, when $r(\Psi_0) = \epsilon_0$ is the ground state energy. Here $\hat{S}$ is an overlap operator, needed when using Vanderbilt pseudopotentials [32]. Moreover, if one minimizes the Rayleigh quotient in the subspace orthogonal to a set of already calculated wavefunctions $\Omega = \{|\Psi_i\rangle, \hat{H}|\Psi_i\rangle = \epsilon_i|\Psi_i\rangle\}$, it is easy to show that $|\Psi_T\rangle$ will converge to the lowest eigenstate not contained in Ω. The diagonalization problem is thus recast into a constrained minimization in which the search directions for the correction of the trial wavefunctions are given by the residual vectors:

$$|R(\psi_T)\rangle = \frac{\delta}{\delta\langle\Psi_T|} r(\Psi_T) = \frac{1}{\langle\Psi_T|\hat{S}|\Psi_T\rangle}\left(\hat{H} - r(\Psi_T)\hat{S}\right)|\Psi_T\rangle. \tag{A.2}$$

The most important algorithms of this class are the Davidson's [90] and the Conjugate Gradient [91, 92] ones.

The main drawback of the approach just described is the need to enforce the orthonormalization of the trial wavefunctions, which requires a global operation whose computational workload scales as $O(N_{at}^3)$, where N_{at} is the number of atoms in the primitive cell. Such a bad scaling is important only when N_{at} is large enough, and it represents the bottleneck of the calculation. A possible solution to this problem has been originally proposed by Pulay and Wood [93, 94], who observed that the Rayleigh quotient is stationary at each eigenvalue, even if it does not posses a minimum. Thus the norm of the residual vector has a local, unconstrained minimum at the system eigenstates. This idea can be translated into a very efficient diagonalization method called *Direct Inversion in the Iterative Subspace* (DIIS) which, starting from an initial set of trial wavefunction, optimizes the norm of their residuals without any additional constraint: at convergence the orthonormalization condition will be automatically satisfied.

We now come to a short description of our implementation, that follows the one given in [95]. Each band is optimized independently. Starting from an initial guess for the wavefunction $|\Psi^0\rangle$ a new trial is constructed:

$$|\Psi^1\rangle \leftarrow |\Psi^0\rangle + \lambda \hat{K} |R(\Psi^0)\rangle \tag{A.3}$$

where $\hat{K}$ is a suitable preconditioning operator (used to fasten the convergence) and the λ parameter is chosen so as to minimize the Rayleigh quotient, $r(\Psi^1)$. Note that this step will generally lead the actual band in the wrong direction, because of the neglect of the orthonormalization requirement. This error will be corrected in the subsequent part of the calculation that switches to the optimization of the residual vector, using Pulay's method. We look for the best linear combination of the n preceding trials:

$$|\bar{\Psi}^n\rangle = \sum_{i=1,n} \alpha_i |\Psi^i\rangle \tag{A.4}$$

which minimizes the squared norm of the residual vector, $\langle R(\bar{\Psi}^n)|R(\bar{\Psi}^n)\rangle$. This is a non-linear problem but, if the starting guess for $|\Psi\rangle$ is accurate enough, a linear interpolation will do the job: [1]

$$|R(\bar{\Psi}^n)\rangle \simeq \sum_{i=1,n} \alpha_i |R(\Psi^i)\rangle. \tag{A.5}$$

[1] This is especially true when the eigenenergies will be already converged so to give an almost perfect linear relation.

in order to obtain the $\{\alpha_i\}$ coefficients, one minimizes the following expression:

$$\langle R(\bar{\Psi}^n)|R(\bar{\Psi}^n)\rangle \simeq \frac{\sum_{i,j}\alpha_i^*\alpha_j\langle R(\Psi^i)|R(\Psi^j)\rangle}{\sum_{i,j}\alpha_i^*\alpha_j\langle R(\Psi^i)|\hat{S}|R(\Psi^j)\rangle}, \tag{A.6}$$

which is equivalent to finding the smallest eigenvalue and the corresponding eigenvector of the positive-definite problem:

$$\sum_j\langle R(\Psi^i)|R(\Psi^j)\rangle\alpha_j = \xi\sum_j\langle R(\Psi^i)|\hat{S}|R(\Psi^j)\rangle\alpha_j. \tag{A.7}$$

Once this is done the next approximation for the current band is:

$$|\Psi^{n+1}\rangle = |\bar{\Psi}^n\rangle + \lambda\hat{K}|R(\bar{\Psi}^n)\rangle, \tag{A.8}$$

and the procedure is repeated until some convergence criterion is satisfied (usually on the norm of the residual vector) and a new band is considered. This scheme is in principle exact but its efficiency depends very much on the starting wavefunctions. In particular, if the initial update of a given band (A.3) contains important contributions from states which are near in energy, the entire procedure is dramatically slowed down and it can even miss the correct solution. In order to avoid these problems, the initial guess for the wavefunctions has to be well educated (we use linear combinations of atomic orbitals), and it is always convenient to rotate the initial set of states into a representation in which the Hamiltonian is diagonal. This last procedure is important (even if it is an $O(N_{at}^3)$ operation) because it makes the residual vectors orthogonal to the current set of wavefunctions, so that the initial step (A.3) is much less problematic. The main advantages of this method are the reduced use of complete orthonormalizations (only two: at the beginning of the diagonalization and at the end, to build the charge density), and the clear data locality of the algorithm. This means that it is possible to process more than one wavefunction at the same time—by distributing the bands over the processors or by using a wavefunctions buffer with scalar computers—with a large increase of performance. We have not extensively tested the program but, to give a rough idea, the DIIS code runs approximately twice as fast as the Davidson one for systems containing some 10-20 transition metal atoms in the unit cell. For larger systems (40-50 atoms) the relative efficiency reaches better values between 3 and 4.

Appendix B

Spin constrained calculations

It is sometimes interesting to study the energetics of a system as a function of some internal parameter, especially when one is trying to asses the stability of the system. In particular, in the spin−dependent case, it is important to study how the energy depends, for instance, on the total magnetic moment M of the cell:

$$M = \int_V m(\mathbf{r}) d\mathbf{r} \tag{B.1}$$
$$m(\mathbf{r}) = n^{\uparrow}(\mathbf{r}) - n^{\downarrow}(\mathbf{r}),$$

where $m(\mathbf{r})$ is the spin magnetization density and V is the cell's volume. This can be done on a very general setting using Lagrange multipliers much in the same way used to constrain the KS wavefunction to be orthonormal and the number of electrons to be conserved (see Eq. 1.2 and 1.4). In fact, changing the KS functional $E[n]$ as follows:

$$E[n] \leftarrow E^{LM}[n] = E[n] + H\Big(\int_V m(\mathbf{r}) d\mathbf{r} - M\Big), \tag{B.2}$$

the last term guarantees the total magnetic moment to be equal to M, since the stationarity of $E^{LM}[n]$ with respect to H enforces such a constraint. The KS equations are modified accordingly, with the introduction of a homogeneous magnetic field H coupled to the spins:

$$\frac{\delta E^{LM}[n]}{\delta \psi^*_{i\sigma}(\mathbf{r})} = \big(\hat{H}_{KS} - \epsilon_{i\sigma}\big)\psi_{i\sigma} + s_\sigma H \psi_{i\sigma} = 0 \tag{B.3}$$

where s_σ = ± 1 if the spin index σ is $\uparrow$ or $\downarrow$, respectively. Applying the field H is equivalent to the use of different Fermi levels ϵ_F^σ for the two spins, in such a way as to satisfy:

$$\epsilon_F^{\uparrow} - \epsilon_F^{\downarrow} = 2H. \tag{B.4}$$

Thus, at each iteration of the self-consistent cycle, it is sufficient to find the Fermi levels ϵ_F^σ imposing the fulfillment of the magnetic constraint, to perform automatically the minimization with respect to H, without having to solve the KS equation for each considered value of H. The technique we have just described is known as Fixed Spin Moment Method (FSM) and it has been applied to study magnetization fluctuations in solids, magnetic phase transition and a host of different problems, also with constraints different from the magnetic ones [96, 97].

When the constraint to be imposed is local – for instance requiring the spin magnetization in a given domain Ω to have a value M_Ω – the FSM can be formulated by adding the following term to the KS energy functional:

$$-H\Big(\int_V m(\mathbf{r})\chi_\Omega(\mathbf{r})d\mathbf{r} - M_\Omega\Big), \tag{B.5}$$

where $\chi_\Omega(\mathbf{r})$ is a weighting function localized in Ω. In this case, however, the application of the FSM method is no longer straightforward because the KS equations now read:

$$\frac{\delta E^{LM}[n]}{\delta\psi^*_{i\sigma}(\mathbf{r})} = \big(\hat{H}_{KS} - \epsilon_{i\sigma}\big)\psi_{i\sigma} + s_\sigma H\chi_\Omega(\mathbf{r})\psi_{i\sigma} = 0, \tag{B.6}$$

and contain a spatially varying magnetic field $H\chi_\Omega(\mathbf{r})$, which makes impossible to satisfy the constraint by only varying ϵ_F^σ. Moreover, the imposed constraint is not well suited to be implemented using PW's, since the presence of the inhomogeneous magnetic field introduces spurious Fourier components that can not be eliminated without spoiling the orthonormality of the wavefunctions [98].

In this work we have by-passed this problem using a different technique to fix the average spin magnetization in localized regions of space [98]. We have, in particular, minimized a different unconstrained electronic functional whose stationarity point coincides with that of the original, constrained system. In fact, introducing the following energy functional which contains a positive-definite penalty term:

$$E^{PF}[n] = E[n] + \lambda\Big(\int_V m(\mathbf{r})\chi_\Omega(\mathbf{r})d\mathbf{r} - M_\Omega\Big)^2, \quad \lambda = const > 0, \tag{B.7}$$

with a large enough λ constant, the minimization procedure will favor the second term of Eq. (B.7), thus satisfying the constraint. It is possible to show that in the $\lambda \to \infty$ limit the penalty term goes to zero and $E^{PF}[n]$ gets to the constrained $E[n]$, so that the described procedure is equivalent to the use a Lagrange multiplier [65]. Using this approach the KS equations for $E^{PF}[n]$ are the following:

$$\frac{\delta E^{PF}[n]}{\delta\psi^*_{i\sigma}(\mathbf{r})} = \big(\hat{H}_{KS} - \epsilon_{i\sigma}\big)\psi_{i\sigma} + 2s_\sigma\lambda\chi_\Omega(\mathbf{r})\Big(\int_V m(\mathbf{r})\chi_\Omega(\mathbf{r})d\mathbf{r} - M_\Omega\Big)\psi_{i\sigma} = 0, \tag{B.8}$$

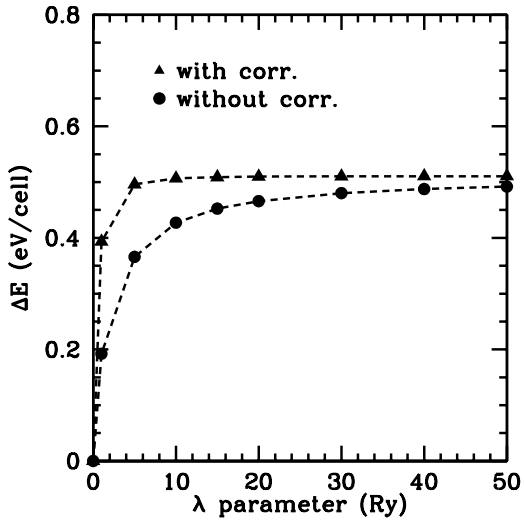

Figure B.1: Effect of the perturbative correction (B.10) on the total energy for Rh bulk, calculated with the penalty functional technique.

and present an inhomogeneous magnetic field, defined self-consistently by the actual polarization, which is trivial to implement in the existing codes. One practical difficulty to take into account is that the use of a very large λ causes instabilities in the diagonalization step of the calculation. One possible remedy is the choice of a reasonably small λ, then extrapolating the results for $\lambda \to \infty$ perturbatively. In fact, expanding $E^{PF}[n]$ to first order in $1/\lambda$:

$$E^{PF}[n, 1/\lambda] = E^{PF}[n, 1/\lambda = 0] + \frac{d}{d(1/\lambda)} E^{PF}[n, 1/\lambda]\Big|_{1/\lambda=0} 1/\lambda + O^2(1/\lambda), \quad \text{(B.9)}$$

one easily finds the correction term for the energy:

$$E^{PF}[n, \lambda \to \infty] = E^{PF}[n, \lambda] + \lambda \Big(\int_V m(\mathbf{r}) \chi_\Omega(\mathbf{r}) d\mathbf{r} - M_\Omega \Big)^2 + O(1/\lambda)^2. \quad \text{(B.10)}$$

In Fig. B.1 we show the effect of this correction for a spin constrained calculation for a rhodium fcc crystal: it is evident how this modification can make possible to effectively reduce the λ parameter to work with.

E siamo ai ringraziamenti. Credetemi, e' un bel momento. Desidero innanzi tutto ringraziare Stefano Baroni, Stefano de Gironcoli e Andrea Dal Corso per tutta la cortesia e la pazienza che hanno dimostrato nei tre anni della mia permanenza a Trieste. In questo senso sono anche grato a David Loffreda, che mi ha aiutato non poco nello svolgimento di questa tesi. Quello che sono riuscito a scrivere lo devo a loro. Inoltre volevo salutare molti amici, la lista e' necessariamente incompleta. Luca, sempre molto allegro e loquace (a volte in maniera incomprensibile), che si e' rivelato un amico prezioso per superare alcuni momenti un po' difficili. Paul, che forse dopo tre anni di dottorato a Trieste riuscira' finalmente ad imparare l'italiano. Michele, con il quale ho condiviso molte piacevoli seratine passate a debuggare. E poi Massimo, Leonardo, Gianni, Stefano, Andrea&Giannette, Lorenzo, Andrea, Francesca e tutti gli altri che si sono trovati sulla stessa barca. Alle fine, pero', volevo ringraziare Benedetta, che mi ha insegnato ad apprezzare molte cose al di fuori della fisica.

Bibliography

[1] A. Zangwill, *Physics at Surfaces*, Cambridge University Press, 1988.

[2] W. Kohn and L. Sham, Phys Rev. **140**, A1133 (1965).

[3] P. Hohenberg and W. Kohn, Phys. Rev. **136**, B864 (1964).

[4] D. Ceperley and B. Alder, Phys. Rev Lett. **45**, 566 (1980).

[5] W.E. Pickett, Comp. Phys. Rep. **9**, 115 (1989).

[6] J.P. Perdew, K. Burke, and M. Ernzerhof, Phys. Rev. Lett. **77**, 3865 (1996).

[7] C. Backx et al., Surf. Sci. **128**, 80 (1983).

[8] A. Raukema et al., J. Phys.:Cond. Matt. **8**, 2247 (1996).

[9] C. Rheven et al., Zeitshrift fur Phy. Chemie **174**, 12 (1991).

[10] X. Bao et al., Phys. Rev. B **54**, 2249 (1996).

[11] V.I. Bukhtiyarov et al., Surf. Sci. **232**, L205 (1990).

[12] M. Rocca et al. Phys. Rev. B **61**, 213 (2000).

[13] J.F. Janack, Phys. Rev. B **16**, 255 (1977).

[14] J.H. Cho and M. Scheffler, Phys. Rev. Lett. **78**, 1299 (1997).

[15] A. Goldoni et al., Phys. Rev. Lett. **82**, 3156 (1999).

[16] R. Rosei, private comunication.

[17] W. Nichtl et al., Surf. Sci. **188**, L729 (1987).

[18] C. Clink et al., Phys. Rev. Lett. **71**, 4350 (1993) and references therein.

[19] Y.G. Shen et al., Phys. Rev. B **56**, 9894 (1997).

[20] N.W. Ashcroft and N.D. Mermin, *Solid State Physics*, Saunders Coll. Pub. (1976).

[21] R.G. Parr and W. Yang, *Density Functional Theory of Atoms and Molecules*, Oxford University Press (1989).

[22] H. Hellmann, Einführung in die Quantenchemie (Deuticke, Leipzig, 1937).
R.P. Feynmann, Phys. Rev. **56**, 340 (1939).

[23] J.P. Perdew and A. Zunger, Phys. Rev. B **23**, 5040 (1981).

[24] R.O. Jones and O. Gunnarson, Rev. Mod. Phys. **61**, 689 (1989).

[25] B. Hammer, K.W. Jacobsen and J.K. Norskov, Phys. Rev. Lett. **70**, 3971 (1993).

[26] J.P. Perdew et al., Phys. Rev B **45**, 6671 (1991).

[27] M. Methfessel and A. Paxton, Phys. Rev. B **40**, (1989) 3136.

[28] J. Ihm, A. Zunger, and M.L. Cohen, J. Phys. **C12**, 4409 (1979).

[29] G.B. Bachelet, D.R. Hamann and M. Schlüter, Phys. Rev. B **26**, 4199 (1982).

[30] D.R. Hamann, M. Schlüter, and C. Chiang, Phys. Rev. Lett. **43**, 1494 (1979).

[31] L. Kleinmann adn D.M. Bylander, Phys. Rev. Lett. **48**, 1425 (1982).

[32] D. Vanderbilt, Phys. Rev. B **41**, 7892 (1990).

[33] J. Zhu, X.W. Wang, and S.G. Louie, Phys. Rev. B **45**, 8877 (1992).

[34] H.A. Engelhardt and D. Menzel, Surf. Sci. **57**, 591 (1976).

[35] C.S. Ares Fang, Surf. Sci. Lett. **235**, L291 (1990).

[36] M. Wuttig at al., Surf. Sci. **213**, 103 (1989).

[37] A.M. Rappe et al., Phys. Rev. B **41**, 1227 (1990).

[38] G. Kresse and J. Hafner, J. Phys.: Cond. Mat. **6**, 8245 (1994).

[39] H.J. Monkhort and J.D. Pack, Phys. Rev. B **13**, 5188 (1976).

[40] Press W.H., Teukolsky S.A., Vetterling W.T. and Flannery B.P., *Numerical Recipes in FORTRAN* , Cambridge University Press (1992).

[41] Bohnen et al., in *The Structure of Surfaces III*, Spinger Series in Surface Sciences **24**, 16 (1990).

[42] M. Methfessel et al., Phys. Rev. B **46**, 4816 (1992).

[43] H. Li et al., Phys. Rev. B **43**, 7305 (1991).

[44] W.R. Tyson, and W.A. Miller, Surf. Sci. **62**, 267 (1972).

[45] *Handbook of Chemistry and Physics* 74th ed., CRC Press (1988).

[46] D.M. Newns, Phys. Rev. **178**, 1123 (1969).

[47] J.M.Ricart et al., Surf. Sci. **307**, 107 (1994).

[48] R. Mayer et al., Phys. Rev. B **33**, 8899 (1986).

[49] M. Wutting, Surf. Sci. **213**, 103 (1989).

[50] F.M. Leiblse, Surf. Sci. **337**, 51 (1995).

[51] F. Besenbacher and J.K. Norskov, Prog. in Surf. Sci. **44**, 5 (1980).

[52] L. Savio, L.Vattuone, and M. Rocca, accepted for publication on Phys. Rev. B.

[53] D.M. Kolb et al., Phys. Rev. Lett. **47**, 1921 (1981).

[54] H. Ershbaumer et al., Surf. Sci. **243**, 317 (1991).

[55] M. Canepa et al., Journal of Electron Spectroscopy and Related Phenomena **76**, 471 (1995).

[56] A. Goldmann, and E. Bartels, Surf. Sci. **122**, L629 (1982).

[57] P. Sandl and E. Bertel, Surf. Sci. Lett. **302**, L325 (1994).

[58] N. Memmel, Surf. Sci. Rep. **32**, 91 (1998).

[59] A.J. Cox, J.G. Loudernack, and L. Bloomfield, Phys. Rev. Lett. **71**. 923 (1993).

[60] H. Li et al., Phys. Rev. B **44**, 1438 (1991).

[61] W. Oed et al., Surf. Sci. **207**, 55 (1988).

[62] I. Morrison, D. M. Bylander, and L. Kleinmann, Phys. Rev. Lett. **71**, 1083 (1993).

[63] M. Weinert, S. Blugel, and P.D. Johnson, Phys. Rev. Lett. /bf 71, 4097 (1993).

[64] S.C. Wu et al., Phys. Rev. b **49**, 14081 (1994).

[65] R. Gebauer, and S. Baroni, Phys. Rev. B **61**, R6459 (2000).

[66] G. Comelli et al., Surf. Sci. Rep. **32**, 165 (1998).

[67] M. Gierer et al., Surf. Sci. **297**, L73 (1993).

[68] J.D. Batteas et al., Surf. Sci. **339**, 142 (1995).

[69] K. Stokbro and S. Baroni, Surf. Sci. **370**, 166 (1997).

[70] D. Alfè et al., Chem. Phys. Lett. **211**, 220 (1993).

[71] G. Comelli et al., Chem. Phys. Lett. **261**, 253 (1996).

[72] C.W. Tucker, J. Appl. Phys. **37**, 4147 (1966).
C.W. Tucker, J. Appl. Phys. **38**, 2696 (1967).

[73] E. Shwarz et al., Vacuum **41**, 167 (1990).

[74] V.R. Dhanak et al., Chem. Phys. Lett. **188**, 237 (1992).

[75] P.W. Murray et al., Phys. Rev. B **47**, 12976 (1993).

[76] V.R. Dhanak et al., Phys. Rev. B **49**, 5585 (1994).

[77] C. Comincioli et al., Chem. Phys. Lett. **214**, 438 (1993).

[78] A. Eicheler et al., Surf. Sci. **346**, 300 (1996).

[79] D. Alfè, Ph.D. thesis, http://www.sissa.it/cm/PHD.html.

[80] http://www.shef.ac.uk/chem/web-elements.

[81] J. Tersoff, and D.R. Hamann, Phys. Rev. B **31**, 805 (1985).

[82] D. Alfè, S. de Gironcoli, and S. Baroni, Surf. Sci. **410**, 151 (1998).
D. Alfè, S. de Gironcoli, and S. Baroni, Surf. Sci. **437**, 18 (1999).

[83] T.W. Orent and S.D. Bader, Surf. Sci. **115**, 323 (1982).

[84] G. Simons et al., J. Phys. Chem. **95**, 4522 (1991).

[85] A. Watcher, K.P. Bohen, and K.M. Ho, Surf. Sci. **346**, 127 (1996).

[86] P. Kolthoff et al., Surf. Sci. **365**, 374 (1996).

[87] H. Onishi et al., Surf. Sci. **392**, L51 (1997) and Surf. Sci. **444**, 7 (2000).

[88] H. Onishi et al., Surf. Sci. **283**, 231 (1993).

[89] N. Watari et al., Jpn. J. App. Phys. **39**, 1457 (2000).

[90] E.R. Davidson, in: *Methods in Computational Molecular Physics*, NATO Advanced Study Institute, Ser. **C**, Vol **113**, 95 (1983).

[91] I. Stich and al., Phys. Rev. B **39**, 4997 (1989).

[92] M.P. Teter, M.P. Payne, and D.C. Allan, Phys. Rev. B **40**, 12255 (1989).

[93] P. Pulay, Chem. Phys. Lett. **73**, 393 (1980).

[94] D.M. Wood and A. Zunger, Journ. of Phys. A:Math. Gen. **18** (1985).

[95] G. Kresse and J. Furthmuller, Comp. Mat. Sci. **6**, 15 (1996).

[96] P.H. Dederihcs et al., Phys. Rev. Lett. **53**, 2512 (1984).

[97] V.L. Moruzzi et al., Phys. Rev. B **34**, 1784 (1986).

[98] R. Gebauer, Ph.D. thesis, http//www.cecam.fr/local-resources/ralph.gebauer.ps